

Utah State University

DigitalCommons@USU

All Graduate Theses and Dissertations

Graduate Studies

5-2022

A Study of Wings with Constant and Variable Sweep for Aerodynamic Efficiency in Inviscid Flow

Bruno Moorthamers
Utah State University

Follow this and additional works at: <https://digitalcommons.usu.edu/etd>



Part of the [Aerospace Engineering Commons](#)

Recommended Citation

Moorthamers, Bruno, "A Study of Wings with Constant and Variable Sweep for Aerodynamic Efficiency in Inviscid Flow" (2022). *All Graduate Theses and Dissertations*. 8369.
<https://digitalcommons.usu.edu/etd/8369>

This Dissertation is brought to you for free and open access by the Graduate Studies at DigitalCommons@USU. It has been accepted for inclusion in All Graduate Theses and Dissertations by an authorized administrator of DigitalCommons@USU. For more information, please contact digitalcommons@usu.edu.



A STUDY OF WINGS WITH CONSTANT AND VARIABLE SWEEP FOR
AERODYNAMIC EFFICIENCY IN INVISCID FLOW

by

Bruno Moorthamers

A dissertation submitted in partial fulfillment
of the requirements for the degree

of

DOCTOR OF PHILOSOPHY

in

Aerospace Engineering

Approved:

Douglas F. Hunsaker, Ph.D.
Major Professor

Randy Christensen, Ph.D.
Committee Member

Matt Harris, Ph.D.
Committee Member

Geordie Richards, Ph.D.
Committee Member

Stephen A. Whitemore, Ph.D.
Committee Member

D. Richard Cutler, Ph.D.
Interim Vice Provost of Graduate Studies

UTAH STATE UNIVERSITY
Logan, Utah

2021

Copyright © Bruno Moorthamers 2021

All Rights Reserved

ABSTRACT

A Study of Wings with Constant and Variable Sweep for Aerodynamic Efficiency in
Inviscid Flow

by

Bruno Moorthamers, Doctor of Philosophy

Utah State University, 2021

Major Professor: Douglas F. Hunsaker, Ph.D.

Department: Mechanical and Aerospace Engineering

Wing sweep has been studied by industry and academia since the pioneering days of aviation for both high-speed and low-speed applications. In transonic and supersonic flight regimes it serves to delay the onset of compressibility effects and decrease wave drag. In subsonic conditions, flying wing designs sweep back the main lifting surface in such a way that it can be used for longitudinal stability and control, to allow for the elimination of a traditional empennage. This is desirable because it can decrease the aerodynamic drag. Sweep can also be seen in nature in the wings of birds and fins of fish. While sweep in man-made airplanes is mostly limited to a constant sweep angle from wing root to wing tip, nature shows a curved sweep profile in the wings of birds and fins of fish. There might be an aerodynamic benefit to non-constant or variable sweep profiles. This research attempts to discover the potential aerodynamic benefits of non-constant sweep. In the present work, the theoretical background of our current understanding of swept wing aerodynamics is revisited. Inviscid numerical methods are used to investigate the lift, induced drag, and aerodynamic center position of conventional wings with constant sweep, and crescent wings with a linear sweep profile, where the local sweep increases from zero at the wing root to some finite value at the tip. A comparison between the two types is made to see whether

the curved wing planforms offer a potential aerodynamic benefit over conventionally swept wings. The wings are compared at equivalent aerodynamic center position so that they will offer similar longitudinal stability. An induced drag factor that is nearly independent of lift coefficient and acts as a measure for aerodynamic efficiency, is the performance metric used in the aerodynamic comparison. A cross-over point that indicates at what aerodynamic center position or equivalent sweep angle the crescent sweep profile produces less induced drag than the constant sweep profile is found and shown as a function of aspect and taper ratio. The wing of an albatross is used to demonstrate that some more complex sweep profiles can produce less induced drag than both constant or purely linear sweep profiles in inviscid flow. A separate chapter studies the effects of viscosity on the results found in this work, by modeling the boundary layer thickness, flow transition, and laminar and turbulent skin friction using FlightStream. It shows that when including viscous effects, the wings with constant and linear sweep show similar trends with sweep as those resulting from inviscid results. The cross-over point between wings with constant sweep and linear sweep when considering total drag coefficient is shown to not differ significantly from that of the inviscid results for induced drag, especially not at the small angles of attack considered in this research. Therefore, the findings from the inviscid study are insightful in understanding the effects of sweep type and angle on induced drag. Finally, an optimization exercise is performed to find sweep profiles that offer lower induced drag than both the constant and linear sweep profiles in a purely inviscid scenario. It is shown that there are more efficient sweep profiles, but proving that any solution is the global minimum is difficult. It is also addressed that these results would likely not perform as well in a real world setting.

ACKNOWLEDGMENTS

I would like to acknowledge a few people without whom the last four years of research and the writing of this dissertation would have been a lot harder. First of all I'd like to thank Dr. Douglas Hunsaker for inviting me to do research in his lab, the opportunities he created for me, and the continued guidance and motivation he has given me throughout the past 4 years. I stumbled upon his work through shared interests, and I realize the gamble he took by taking me on after exchanging a few emails from halfway across the world. I also want to thank the rest of my committee for any help and advice they provided.

I would like to thank Research In Flight, and especially Dr. Vivek Ahuja, for his training in the use of FlightStream and his constant and immediate support. Learning about FlightStream was a pivotal moment in my research that undid a lot of frustration with earlier tools, and without Vivek's help it would not have gone as smoothly. Thank you to Dr. Willem A.J. Anemaat from DARcorporation for introducing me.

Thank you to my parents and brothers for supporting my endeavors, and accepting that I am always far away from home. The past four years have been accompanied by hardships, both academic and personal, and they became significantly easier to bear thanks to my friends and family, near and far. Kristoff, Troy, Adam, Matt, the AeroLab, the extended crew of the USU ceramics department, and others (you know who you are); Thank you!

This work was partially funded by the U.S. Office of Naval Research Sea-Based Aviation program (Grant No. N00014-18-1-2502) with Brian Holm-Hansen as the program officer.

Bruno Moorthamers

CONTENTS

	Page
ABSTRACT	iii
ACKNOWLEDGMENTS	v
LIST OF TABLES	viii
LIST OF FIGURES	ix
NOTATION	xiv
1 INTRODUCTION	1
2 THEORETICAL BACKGROUND TO FINITE WING AERODYNAMICS	6
2.1 SOLUTIONS FROM LIFTING-LINE THEORY FOR WINGS WITHOUT SWEEP	6
2.2 KÜCHEMANN'S ANALYTICAL DERIVATINS OF SWEPT WING AERODYNAMICS	8
2.3 AERODYNAMIC CENTER FOR A SPANWISE SECTION OF A FINITE WING IN INVISCID FLOW	12
3 COMPUTATIONAL METHODOLOGY	17
3.1 DEFINITION OF GEOMETRY	17
3.2 NUMERICAL AERODYNAMIC TOOLS	20
3.2.1 MACHUPX	22
3.2.2 PANAIR	23
3.2.3 FLIGHTSTREAM	24
3.3 CALCULATION OF THE LOCUS OF SECTION AERODYNAMIC CENTERS	29
3.4 CALCULATION OF THE GLOBAL AERODYNAMIC CENTER POSITION	31
3.5 GENERAL AERODYNAMIC RELATIONS FOR COMPARISON OF WINGS WITH AND WITHOUT SWEEP	31
4 AERODYNAMIC PROPERTIES OF WINGS WITHOUT SWEEP IN INVISCID FLOW	34
4.1 RESULTS FOR LIFT	34
4.2 RESULTS FOR INDUCED DRAG	36
5 EVALUATION OF KÜCHEMANN'S ANALYTIC SOLUTIONS FOR WINGS WITH CONSTANT SWEEP	38
5.1 RESULTS FOR CONSTANT REARWARD SWEEP	38
5.2 RESULTS FOR THICKNESS VARIATION	43
5.3 RESULTS FOR CONSTANT FORWARD SWEEP	46

6	AERODYNAMIC PROPERTIES OF WINGS WITH CONSTANT SWEEP IN INVISCID FLOW	52
6.1	RESULTS FOR LIFT	53
6.2	RESULTS FOR INDUCED DRAG	53
6.3	RESULTS FOR AERODYNAMIC CENTER	56
7	AERODYNAMIC PROPERTIES OF WINGS WITH LINEAR SWEEP IN INVISCID FLOW	58
7.1	RESULTS FOR LIFT	58
7.2	RESULTS FOR INDUCED DRAG	60
7.3	RESULTS FOR AERODYNAMIC CENTER	61
8	COMPARISON OF INVISCID AERODYNAMICS OF WINGS WITH CONSTANT AND LINEAR SWEEP	63
8.1	COMPARISON CRITERIA	63
8.2	RESULTS FOR WINGS WITH ASPECT RATIO $R_A = 8$ AND TAPER RATIO $R_T = 0.25$	65
8.3	RESULTS FOR WINGS OF VARYING ASPECT AND TAPER RATIO	73
8.4	COMPARISON TO ALBATROSS WING	79
8.5	DISCUSSION AND CONSIDERATIONS	81
9	EFFECTS OF VISCOSITY ON WINGS WITH SWEEP	84
10	OPTIMIZATION OF WING SWEEP PROFILE FOR MINIMUM κ_D	91
10.1	OPTIMIZATION SETUP	91
10.2	INFLUENCE OF INITIAL GUESS	93
10.3	INFLUENCE OF NUMBER OF SPANWISE SECTIONS	97
10.4	RESULTS FOR OPTIMIZATIONS AT DIFFERENT κ_{ac}	99
10.5	DISCUSSION AND CONSIDERATIONS	101
11	CONCLUSIONS	103
	REFERENCES	109
	CURRICULUM VITAE	114

LIST OF TABLES

Table	Page
4.1 Planform variables for unswept wing analysis.	34
5.1 Planform variables for evaluation of Küchemann's analytic solution to the locus of aerodynamic centers.	38
5.2 Airfoil Data.	43
5.3 Planform variables for evaluation of Küchemann's analytic solution to the locus of aerodynamic centers of forward swept wings.	49
6.1 Planform variables for wings with constant tip sweep.	52
7.1 Planform variables for wings with linear sweep.	58
10.1 Setup of optimization cases to verify influence of initial guess.	93
10.2 Results of optimization cases to verify influence of initial guess.	94
10.3 Setup of optimization cases to verify influence of number of spanwise sections.	98
10.4 Results of optimization cases to verify influence of number of spanwise sections.	99
10.5 Setup of optimization cases at different κ_{ac}	99
10.6 Results of optimization cases at different κ_{ac}	100

LIST OF FIGURES

Figure		Page
1.1	Frigatebird in gliding flight showing forward sweep on the inboard portion of the wing ¹	2
1.2	Comparison of wing sweep of the swift in gliding flight (left) and high speed flight (middle) to a McDonnell Douglas MD-11 airliner (right).	2
1.3	Comparison of a crescent wing with a linear sweep profile (left) to a wing with constant sweep (right).	4
2.1	Comparison of Küchemann's analytical solution [1] for the locus of section aerodynamic centers and experimental data by Kolbe [2], Hall [3], Graham [4] and Weber [5]. Data extracted from Phillips [6].	11
2.2	Spanwise lift coefficient distribution for an elliptic wing using a NACA 0012 airfoil.	13
2.3	Lift coefficient versus angle of attack at root of an elliptic wing using a NACA 0012 airfoil.	14
3.1	Definition of wing coordinate system.	18
3.2	Crescent wing with a linear sweep profile with $R_A = 8$, $R_T = 0.25$ and $\Lambda_{tip} = 20^\circ$	19
3.3	Local sweep angle of the local quarter-chord line for a linearly swept wing with $R_A = 8$, $R_T = 0.25$ and $\Lambda_{tip} = 20^\circ$	20
3.4	Convergence plots for lift coefficient C_L and pitching moment coefficient C_m as calculated by MachUpX.	23
3.5	Convergence plots for lift coefficient C_L and pitching moment coefficient C_m as calculated by PANAIR.	24
3.6	Convergence plots for lift coefficient C_L and induced drag coefficient C_{D_i} as calculated by FlightStream for wings with $R_T = 0.25$, $R_A = 4$ and $R_A = 20$, and varying tip sweep angle Λ_{tip}	25
3.7	Convergence plots for lift coefficient C_L and induced drag coefficient C_{D_i} as calculated by FlightStream for wings with $R_T = 0.25$, $R_A = 4$ and $R_A = 20$, and varying tip sweep angle Λ_{tip} , expressed as a percentage change from the most refined result.	26

3.8	Comparison of a crescent wing defined using two (left) and four (right) spanwise sections.	27
3.9	Lift coefficient (left) and induced drag coefficient (right) for a linearly swept wing as a function of number of spanwise sections.	28
3.10	Locus of section aerodynamic centers of two elliptic wings with varying quarter-chord sweep.	30
3.11	Deviation of the locus of aerodynamic centers Δx_{ac} as computed using PANAIR for two elliptic wings with varying quarter-chord sweep.	30
4.1	Lift slope correction factor due to taper κ_L as a function of taper ratio R_T for wings with zero sweep.	35
4.2	Induced drag correction factor due to taper κ_D as a function of taper ratio R_T for wings with zero sweep.	36
4.3	Front view and isometric view of FlightStream results of wake and surface pressure field of a wing with aspect ratio $R_A = 4$, taper ratio $R_T = 0.01$, and induced drag factor $\kappa_D = -0.066$	37
5.1	$E_{x_{ac}/c}$ as a function of spanwise position for wings of $R_A = 8$ and different quarter-chord sweep angles.	40
5.2	$E_{x_{ac}/c}$ as a function of spanwise position for wings with $\Lambda_{c/4} = 20^\circ$ and different aspect ratios.	40
5.3	$\Delta x_{ac}/c$ at center section for elliptic wings as a function of aspect ratio and sweep angles.	41
5.4	Root mean square error of $E_{x_{ac}/c}$ as a function of aspect ratio and quarter-chord sweep angle for all wings defined in Table 5.1.	42
5.5	Magnified view of the locus of section aerodynamic centers near the center and tip regions of a wing of $R_A = 8$ and $\Lambda_{c/4} = 20^\circ$ and varying profile thickness. Quarter-chord is indicated by the dashed line.	44
5.6	$E_{x_{ac}/c}$ for an elliptic wing $R_A = 8$ and $\Lambda_{c/4} = 20^\circ$ and varying profile thickness as a function of spanwise position.	44
5.7	Root mean square error of $E_{x_{ac}/c}$ for all wings defined in Table 5.1 for different profile thicknesses defined in Table 5.2.	45
5.8	Root mean square error of $E_{x_{ac}/c}$ for wings with a sweep angle of $\Lambda_{c/4} = 20^\circ$ as a function of aspect ratio for different profile thickness.	46

5.9	Locus of section aerodynamic centers for a wing of $R_A = 8$ and $\Lambda_{c/4} = -20^\circ$. Quarter-chord is indicated by the dashed line.	47
5.10	Magnified view of the locus of section aerodynamic centers near the center and tip regions of a wing of $R_A = 8$ and $\Lambda_{c/4} = -20^\circ$ and varying profile thickness. Quarter-chord is indicated by the dashed line.	48
5.11	$E_{x_{ac}/c}$ for a wing with $R_A = 8$ and $\Lambda_{c/4} = -20^\circ$ as a function of spanwise position for varying profile thickness.	49
5.12	Root mean square error of $E_{x_{ac}/c}$ for all wings defined in Table 5.3 as a function of aspect ratio and sweep angle.	50
5.13	$\Delta x_{ac}/c$ at center section for elliptic wings as a function of aspect ratio and sweep angle.	51
6.1	Lift slope factor δ_L of wings with constant sweep as a function of tip sweep angle Λ_{tip} , aspect ratio, and taper ratio.	54
6.2	Induced drag factor κ_D of wings with constant sweep as a function of tip sweep angle Λ_{tip} , aspect ratio, and taper ratio.	55
6.3	Aerodynamic center shift factor κ_{ac} of wings with constant sweep as a function of tip sweep angle Λ_{tip} , aspect ratio, and taper ratio.	57
7.1	Lift slope factor δ_L of wings with linear sweep as a function of tip sweep angle Λ_{tip} , aspect ratio, and taper ratio.	59
7.2	Induced drag factor κ_D of wings with linear sweep as a function of tip sweep angle Λ_{tip} , aspect ratio, and taper ratio.	61
7.3	Aerodynamic center shift factor κ_{ac} of wings with linear sweep as a function of tip sweep angle Λ_{tip} , aspect ratio, and taper ratio.	62
8.1	Wings with $R_A = 8$, $R_T = 0.25$ and $\Lambda_{tip} = 20^\circ$ featuring constant and linear sweep profiles.	64
8.2	Aerodynamic center shift κ_{ac} as a function of Λ_{tip} for wings with $R_A = 8$ and $R_T = 0.25$ featuring constant and linear sweep profiles.	64
8.3	Induced drag factor κ_D as a function of aerodynamic center shift κ_{ac} for wings with $R_A = 8$ and $R_T = 0.25$ featuring constant and linear sweep profiles.	66
8.4	Change in induced drag factor $\Delta\kappa_D$ between constant and linear sweep profiles as a function of aerodynamic center shift κ_{ac} for wings with $R_A = 8$ and $R_T = 0.25$	67

8.5	Wings with $R_A = 8$, $R_T = 0.25$ featuring constant and linear sweep profiles with equal κ_{ac} and equal κ_D	68
8.6	Drag polars for wings with $R_A = 8$, $R_T = 0.25$ using constant and crescent sweep at the intersection in Fig. 8.3.	69
8.7	Induced drag factor κ_D as a function of lift coefficient C_L for wings with constant and crescent sweep at the intersection in Fig. 8.3	70
8.8	Spanwise lift distribution for wings with constant and crescent sweep at the intersection in Fig. 8.3, evaluated at $C_L = 0.3$	70
8.9	Wings with $R_A = 8$, $R_T = 0.25$ featuring constant and linear sweep profiles with $\kappa_{ac} = 0.50$	71
8.10	Drag polars for wings with $R_A = 8$, $R_T = 0.25$ using constant and crescent sweep with $\kappa_{ac} = 0.50$	71
8.11	Wings with $R_A = 8$, $R_T = 0.25$ featuring constant and linear sweep profiles with $\kappa_D = 0.040$	72
8.12	Drag polars for wings with $R_A = 8$, $R_T = 0.25$ using constant and crescent sweep with $\kappa_D = 0.040$	73
8.13	Induced drag factor κ_D as a function of aerodynamic shift factor κ_{ac} and taper ratio R_T , for wings with aspect ratio $R_A = 8$ featuring constant linear sweep profiles.	74
8.14	Induced drag factor κ_D as a function of aerodynamic shift factor κ_{ac} and aspect ratio R_A , for wings with taper ratio $R_T = 0.25$ featuring constant linear sweep profiles.	75
8.15	Change in induced drag factor $\Delta\kappa_D$ between constant and linear sweep profiles as a function of aerodynamic center shift factor κ_{ac} , aspect ratio R_A , and taper ratio R_T	76
8.16	Cross-over point between constant and linear sweep profiles in terms of aerodynamic center shift factor κ_{ac} as a function of aspect ratio R_A and taper ratio R_T	77
8.17	Cross-over point between constant and linear sweep profiles in terms of equivalent constant tip sweep angle $\Lambda_{tip,cst}$ as a function of aspect ratio R_A and taper ratio R_T	78
8.18	Albatross wing geometry and model representation [7]. ²	79
8.19	Front view and isometric view of FlightStream results of wake and surface pressure field of the albatross wing with induced drag factor $\kappa_D = 0.070$. . .	80

8.20	Comparison between albatross wing and equivalent wings with constant and linear sweep profiles.	81
9.1	Induced drag coefficient C_{D_i} , parasitic drag coefficient C_{D_p} and total drag coefficient C_{D_T} as a function of lift coefficient C_L for a wing with $R_A = 8$ and $R_T = 0.25$ and tip sweep angle $\Lambda_{tip} = 20^\circ$ featuring a constant sweep profile.	85
9.2	Induced drag coefficient C_{D_i} , parasitic drag coefficient C_{D_p} and total drag coefficient C_{D_T} as a function of free stream velocity V for a wing with $R_A = 8$ and $R_T = 0.25$ without sweep, at angle of attack $\alpha = 5^\circ$	86
9.3	Total drag coefficient C_{D_T} as a function of aerodynamic center shift κ_{ac} for wings with $R_A = 8$ and $R_T = 0.25$ featuring constant and linear sweep profiles at $C_L = 0.5$	87
9.4	Induced drag coefficient C_{D_i} as a function of aerodynamic center shift κ_{ac} for wings with $R_A = 8$ and $R_T = 0.25$ featuring constant and linear sweep profiles at $C_L = 0.5$	88
9.5	Total drag coefficient C_{D_T} as a function of aerodynamic center shift κ_{ac} for wings with $R_A = 8$ and $R_T = 0.25$ featuring constant and linear sweep profiles at $C_L = 0.8$	89
9.6	Induced drag coefficient C_{D_i} as a function of aerodynamic center shift κ_{ac} for wings with $R_A = 8$ and $R_T = 0.25$ featuring constant and linear sweep profiles at $C_L = 0.8$	89
10.1	Geometry of results of optimization cases from Table 10.2.	94
10.2	Spanwise lift distributions of optimization cases from Table 10.2, evaluated at $C_L = 0.3$	95
10.3	Surface pressure fields of optimization cases from Table 10.2, evaluated at $C_L = 0.3$	96
10.4	Front views of wakes of optimization cases from Table 10.2, evaluated at $C_L = 0.3$	96
10.5	Geometry of results of optimization cases from Table 10.3.	98
10.6	Geometry of results of optimization cases from Table 10.6.	100

NOTATION

a_n	Fourier coefficient
b	span
c	chord
C_{D_i}	induced drag coefficient
C_L	lift coefficient
\tilde{C}_L	section lift coefficient
$C_{L,\alpha}$	lift slope
$\tilde{C}_{L,\alpha}$	section lift slope
$E_{x_{ac}/c}$	difference between analytical and numerical results for chordwise aerodynamic center position
n_s	number between 0 and 1 related to the chordwise distribution of vorticity
N_{span}	number of spanwise sections used to model a wing
R_A	aspect ratio
R_T	taper ratio
S	wing area
V_∞	freestream velocity
x_{ac}	axial coordinate of aerodynamic center
x_{qc}	axial coordinate of quarter chord
z	spanwise coordinate
α	angle of attack
α_{L0}	zero-lift angle of attack
δ_L	change in lift slope due to sweep
Δx_{ac}	deviation in chordwise aerodynamic center position
η_{root}	spanwise distance from root as a fraction of the local chord
η_{tip}	spanwise distance from tip as a fraction of the local chord

Γ	spanwise section circulation
κ_{ac}	change in aerodynamic center due to sweep
κ_D	induced drag correction factor due to taper, aspect ratio, and sweep
κ_L	lift slope correction factor due to taper and aspect ratio
λ_s	weighting function
$\Lambda_{c/2}$	half-chord sweep
$\Lambda_{c/4}$	quarter-chord sweep
Λ_e	effective sweep
Λ_{tip}	effective sweep
μ_L	Lift parameter used in Eq. (2.31)
μ_m	Moment parameter used in Eq. (2.31)
σ	static margin
θ	change of variables for the spanwise coordinate, $\cos^{-1}(-2z/b)$
ω	Frequency factor used in Eq. (2.31)

CHAPTER 1

INTRODUCTION

Wing sweep has been studied and used by industry and academia in high- and low-speed applications for many decades. It was first studied during the development of high speed aircraft before the Second World War [8], and has traditionally been used to delay the onset of compressibility effects and decrease wave drag at transonic and supersonic speeds. We therefore not only see it being used on supersonic fighter aircraft but also on commercial airliners flying at transonic speeds [9], where the acceleration of air over the airfoil would cause shock waves on an unswept wing. Later developments started utilizing wing sweep in the design of flying wing aircraft [10], where the lever arm resulting from sweeping back the main lifting surface allows for longitudinal stability and control without the use of a conventional empennage. The present research evolved from the interest in tailless flying wing aircraft, and the scope is therefore limited to subsonic conditions.

In early literature, the wing sweep angle was often defined by following the geometrical angle of the leading or trailing edge of the wing, or sometimes even using the imaginary line lying exactly in the middle of these two [1]. These days, literature on aerodynamic research and industry mostly make use of the angle of the quarter-chord line. This is the imaginary line running from wing root to wing tip that connects all the points lying at 25% of the distance from leading edge to trailing edge. The quarter-chord points are a good first estimate in where the aerodynamic center, an important parameter in aerodynamics and stability analysis, lies. This research adheres to this convention of defining wing sweep using the quarter-chord line.

Sweep can be seen in nature in animals, mainly in the wings and tails of birds, and the fins of fish. These sweep profiles are often variable and more complex than those of aircraft, with the local angle of sweep varying significantly from wing root to wing tip, sometimes even showing regions of forward sweep, particularly near the shoulder joint as shown on the

frigatebird in Fig. 1.1.



Fig. 1.1: Frigatebird in gliding flight showing forward sweep on the inboard portion of the wing¹

Man-made airplanes use wings where the quarter-chord sweep angle is constant from root to tip or at most consisting of two or three adjoined sections with each their constant sweep angle. Birds such as the swift [11], however, can morph their wings and sweep angle from a straight wing in slow gliding flight, to a highly swept and curved wing in high-speed flight. Figure 1.2 shows a swift with a nearly straight wing in gliding flight on the left, a swift in high-speed with a curved, crescent-moon shaped wing in the middle, and a McDonnell Douglas MD-11 with constant sweep on the right.



Fig. 1.2: Comparison of wing sweep of the swift in gliding flight (left) and high speed flight (middle) to a McDonnell Douglas MD-11 airliner (right).

¹Figure available via license: Creative Commons Attribution 2.0 Generic. Photo by Peter Swaine.

These curved sweep profiles suggest a linear change in sweep angle, increasing from zero or even a negative angle, indicating a sweep forwards, at the root to some finite positive value at the tip in a linear fashion. In a high-speed maneuver, birds can collapse their tail to a point, suggesting that they also use their main wing for longitudinal stability and control in a similar way as tailless flying-wing aircraft. It has to be noted that while birds can morph their wings mid-flight by spreading their feathers or sweeping their wings aft, this research does not consider morphing of any kind, but instead looks at static wing designs.

Since we see these curved sweep profiles in nature and we like to believe nature offers efficient solutions, it could be believed that wings with curved or other variable sweep profiles pose benefits over wings with constant sweep. In the past, airplane designers have used wings with constant sweep because of the ease of manufacturing, but modern and future manufacturing techniques such as fibre-reinforced composites [12] or 3D-printing [13] could relax these requirements. This research aims to understand a potential increase in aerodynamic efficiency of a wing with a non-constant sweep profile with respect to that of a conventional wing with constant sweep when considering inviscid flow. An inviscid study allows to draw direct one-to-one comparisons between the performance of wing designs that would not be possible when including the effects of viscosity because of its dependence on atmospheric conditions such as air density and viscosity, and flight conditions such as airspeed and lift coefficient. An inviscid approach also allows to greatly expand the number of cases that can be run with limited resources, allow to draw trends that quickly show the relationship between changes in geometry and their effects on aerodynamic performance. A separate chapter on the effects of viscosity is included to show the validity of inviscid results. Previous research by Van Dam [14, 15] and Smith and Kroo [16, 17] suggest an induced-drag reduction by making use of wings with curved sweep profiles. For the purpose of this research we introduce the term *crescent wing* as any wing with a non-constant sweep profile, in reference to its curved, crescent moon-like shape. As a first step the aerodynamic performance of crescent wings with a linear sweep profile is investigated and compared to conventionally swept wings. Figure 1.3 shows a comparison of a crescent wing versus a

conventional wing with constant sweep.

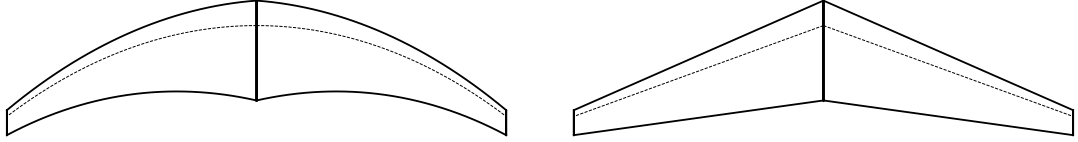


Fig. 1.3: Comparison of a crescent wing with a linear sweep profile (left) to a wing with constant sweep (right).

After comparing the aerodynamic performance of wings with a constant sweep profile to crescent wings featuring a linear sweep profile, the research uses an optimization algorithm to vary the sweep angle at various positions along the wing span to optimize for aerodynamic efficiency.

Due to the limitations of analytic methods, the aerodynamics of swept wings has largely been studied using numerical and experimental methods. Numerical methods for low-speed swept-wing aerodynamics include low-fidelity approaches such as Weissinger's lifting-line method [18] or the numerical lifting-line method by Phillips and Snyder [19] with sweep corrections by Reid and Hunsaker [20], three-dimensional vortex-lattice methods [21, 22], three-dimensional panel methods such as PANAIR [23], and high-fidelity computational fluid dynamics (CFD) simulations. Each of these methods have advantages and disadvantages over the other methods in terms of accuracy, computation time, or complexity of use.

This research considers the aerodynamic predictions for unswept wings using the analytic lifting-line method by Prandtl and compares it with computational methods. The computational methods include the numerical lifting-line method [19] with sweep corrections [20], the three-dimensional high-order panel method PANAIR [23], and Flight-Stream [24], a commercially available panel code. These numerical methods are also used to analyze the aerodynamics of swept wings and compare their results. Due to the low-fidelity nature of each of these methods, the computational expense is low and we are able to construct images that demonstrate aerodynamic behavior over a range of planform design

parameters and sweep angles. By analyzing hundreds of wing designs with varying design parameters we can gain insight in the sensitivity of performance characteristics to design parameters, similar to the insight provided by analytic solutions. The results of these analyses are used to evaluate correction factors for the lift slope and induced drag coefficient of tapered planforms with respect to elliptical planforms. Correction factors to evaluate the effects of wing sweep on lift, induced drag, and aerodynamic center location of wings are also presented.

After performing the same inviscid aerodynamic analyses using the same tools for both wings with constant sweep and crescent wings with a linear sweep profile, a comparison between the two is made to see if one type of wing design has a higher aerodynamic efficiency than the other when excluding effects of viscosity. They are compared at equal aerodynamic center position x_{ac} , thus providing similar longitudinal stability. An optimization study is run to find the optimal spanwise sweep profile for lowest induced drag, to see if a design exists that offers less induced drag than both the wings with constant and linear sweep.

CHAPTER 2

THEORETICAL BACKGROUND TO FINITE WING AERODYNAMICS

This chapter discusses analytical solutions we can gain from lifting-line theory. Section 2.1 shows corrections that can be used to find the lift slope and induced drag coefficient of a tapered finite wing relative to an elliptical planform. Section 2.2 discusses an analytic expression by Dietrich Küchemann for the locus of section aerodynamic centers, an important concept in aerodynamic analysis of wings. It has been updated from its original paper with modern notation.

2.1 SOLUTIONS FROM LIFTING-LINE THEORY FOR WINGS WITHOUT SWEEP

From Prandtl's classical lifting-line theory [25], the circulation distribution at N locations along the span of a wing is defined in terms of a Fourier series terms as

$$\Gamma(\theta) = 2bV_\infty \sum_{n=1}^N A_n \sin(n\theta) \quad (2.1)$$

where b is the wing span, V_∞ is the freestream velocity, and θ is defined from the change of variables related to the spanwise location z as

$$\theta = \cos^{-1}(-2z/b) \quad (2.2)$$

The Fourier coefficients are related to the planform, angle of attack, geometric twist, and aerodynamic twist distribution according to

$$\sum_{n=1}^N A_n \left[\frac{4b}{\tilde{C}_{L,\alpha} c(\theta)} + \frac{n}{\sin(\theta)} \right] \sin(n\theta) = \alpha(\theta) - \alpha_{L0}(\theta) \quad (2.3)$$

where $\alpha(\theta)$ is the geometric twist distribution, which includes the global angle of attack, and

$\alpha_{L0}(\theta)$ is the aerodynamic twist distribution, which includes the effects of camber. Once the Fourier coefficients have been obtained, the resulting lift coefficient and induced drag coefficient can be computed from

$$C_L = \pi R_A A_1, \quad R_A \equiv \frac{b^2}{S} \quad (2.4)$$

$$C_{D_i} = \pi R_A \sum_{n=1}^N n A_n^2 \quad (2.5)$$

Phillips [26] suggests an alternate version of this development in which effects of planform, angle of attack, and twist distribution can be independently evaluated. As an initial study on the effects of sweep, we consider here only wings without geometric or aerodynamic twist, i.e. $\alpha(\theta) - \alpha_{L0}(\theta) = \alpha - \alpha_{L0}$. Following his formulation for a wing without twist, Eq. (2.1) can be rearranged in the form

$$\Gamma(\theta) = 2bV_\infty(\alpha - \alpha_{L0}) \sum_{n=1}^N a_n \sin(n\theta) \quad (2.6)$$

The Fourier coefficients a_n are obtained from

$$\sum_{n=1}^N a_n \left[\frac{4b}{\tilde{C}_{L,\alpha} c(\theta)} + \frac{n}{\sin(\theta)} \right] \sin(n\theta) = 1 \quad (2.7)$$

and are only a function of wing planform and airfoil-section lift slope. Since the airfoil-section lift slope does not vary significantly between designs of most aircraft, the Fourier coefficients a_n can be thought of as a function of mainly the planform. Using this formulation, the lift slope of the finite wing can be found from

$$C_{L,\alpha} = \frac{\tilde{C}_{L,\alpha}}{\left[1 + \tilde{C}_{L,\alpha}/(\pi R_A) \right] (1 + \kappa_L)} \quad (2.8)$$

where the lift-slope factor κ_L is evaluated from

$$\kappa_L = \frac{1 - (1 + \pi R_A/\tilde{C}_{L,\alpha})a_1}{(1 + \pi R_A/\tilde{C}_{L,\alpha})a_1} \quad (2.9)$$

The induced drag can be found from

$$C_{D_i} = \frac{C_L^2}{\pi R_A} (1 + \kappa_D) \quad (2.10)$$

where the induced-drag factor κ_D is evaluated from

$$\kappa_D = \sum_{n=2}^N n \left(\frac{a_n}{a_1} \right)^2 \quad (2.11)$$

Plots for κ_L and κ_D as functions of taper ratio and aspect ratio were published by Phillips [27]. The induced-drag factor κ_D can be thought of as an induced-drag penalty relative to the induced drag produced by the elliptic lift distribution. From lifting-line theory follows that the elliptic lift distribution produces the lowest induced drag for a given span, and so $\kappa_D = 0$ for an elliptic lift distribution. It represents a percentage increase in induced drag for a particular wing planform relative to a planform with the same aspect ratio that would result in the elliptic lift distribution. Glauert [28] was the first to publish a plot for κ_D as a function of taper ratio, but only considered the solution at a single aspect ratio. Results from his plot formed the rule of thumb that a taper ratio near 0.4 will minimize induced drag. However, as pointed out by Phillips [26], this is only true for a wing without geometric or aerodynamic twist. Once twist is added to the wing, the taper ratio that minimizes induced drag can vary significantly from 0.4.

2.2 KÜCHEMANN'S ANALYTICAL DERIVATINS OF SWEPT WING AERO-DYNAMICS

Dietrich Küchemann [1] provides an approximation for the location of the aerodynamic center as a function of spanwise location for a swept wing with a symmetric airfoil of arbitrary thickness. Here we present his method of calculating the location of the locus of aerodynamic centers, but do so in a more modern notation. For a swept wing of infinite

span, Küchemann [1] shows that the aerodynamic center at the wing root is

$$\left(\frac{\Delta x_{ac}}{c}\right)_{\text{root}} = \frac{\Lambda_{c/4}}{\tilde{C}_{L,\alpha}} \quad (2.12)$$

On a swept wing of infinite span the line of vorticity is modeled along the same angle as the geometric sweep. In a finite wing, the interaction between vortex effects of the wing tip and wing root means the line of vorticity will never attain the angle of geometric sweep. Küchemann therefore defines the effective sweep angle to take this effect into account, and iteratively arrives at

$$\Lambda_e = \frac{\Lambda_{c/2}}{\left[1 + \left(\frac{\tilde{C}_{L,\alpha} \cos \Lambda_{c/2}}{R_A \pi}\right)^2\right]^{1/4}} \quad (2.13)$$

where $\Lambda_{c/2}$ is the sweep angle of the half-chord line, $\tilde{C}_{L,\alpha}$ is the section lift-curve slope and R_A is the wing aspect ratio. In Eq. (2.13), the local section lift curve slope $\tilde{C}_{L,\alpha}$ depends on the camber and thickness of the local airfoil. Note that in Eq. (2.13), Küchemann uses half-chord sweep instead of the now more conventional quarter-chord sweep. For the present work, it is assumed the quarter-chord sweep can be used directly instead of the half-chord in Eq. (2.13). Küchemann defines a weighting function to account for the influence of wing root and tip regions dependent on the spanwise position between root and tip. The weighting function is given by

$$\lambda_s = \lambda(\eta_{\text{root}}) - \lambda(\eta_{\text{tip}}) \quad (2.14)$$

where

$$\lambda(\eta) = \sqrt{1 + \left(2\pi \frac{\tan \Lambda_e}{\Lambda_e} \eta\right)^2} - 2\pi \frac{\tan \Lambda_e}{\Lambda_e} \eta \quad (2.15)$$

and

$$\eta_{\text{root}} \equiv \frac{y}{c} \quad (2.16)$$

$$\eta_{\text{tip}} \equiv \frac{b/2 - y}{c} \quad (2.17)$$

Here, b is the wing span, y is the local spanwise coordinate and c is the local chord length. In the case of wings without sweep, indeterminate terms with zero in the numerator and denominator appear in Eq. (2.15). Therefore, L'Hôpital's rule is used to evaluate Eq. (2.15) with $\Lambda_e = 0$ as

$$\lambda(\eta)|_{\Lambda_e=0} = \sqrt{1 + (2\pi\eta)^2} - 2\pi\eta \quad (2.18)$$

With the weighting function given in Eq. (2.14) determining the amount of influence of vortex effects from the wing root and tip regions, the location of the aerodynamic center at any spanwise location can be found from

$$\frac{x_{ac}}{c} = \frac{1 - n_s}{2} \quad (2.19)$$

where

$$n_s = 1 - \frac{1 + \lambda_s \frac{\Lambda_e}{\pi/2}}{2 \left[1 + \left(\frac{\tilde{C}_{L,\alpha} \cos \Lambda_e}{\pi R_A} \right)^2 \right]^{\frac{1}{4(1+2|\Lambda_e|/\pi)}}} \quad (2.20)$$

It should be noted that there is likely a mistake in Eq. (91) in Küchemann's paper [1]. The term within parentheses of the exponent in the denominator of Eq. (2.20) was typeset as $(1 + 2|\Lambda_e|\pi)$ in Küchemann's paper. However, from his derivation and previous equations it can only be concluded that it has to be in fact $(1 + 2|\Lambda_e|/\pi)$, which is what is used in this study.

It is convenient to express the section aerodynamic center location as a shift from its position in two-dimensional flow. The deviation of aerodynamic center location relative to the two-dimensional aerodynamic center position at any spanwise location can be calculated using Küchemann's analytical approach as

$$\left(\frac{\Delta x_{ac}}{c} \right)_{\text{Küchemann}} = \frac{1 - n_s}{2} - \left(\frac{x_{ac}}{c} \right)_{2D} \quad (2.21)$$

Figure 2.1 shows a comparison between the locus as found using Küchemann's approach and experimental data points from others [2–5] for different wing designs. The dashed line shows the locus of section aerodynamic centers as predicted by Küchemann and the circular

symbols indicate the experimental data points. The locus is seen to move forward towards the wing tip and aft towards the wing root.

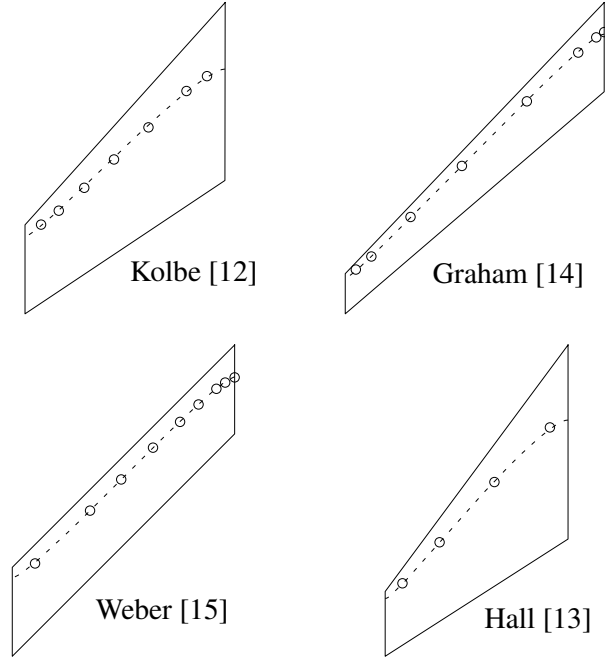


Fig. 2.1: Comparison of K  chemann's analytical solution [1] for the locus of section aerodynamic centers and experimental data by Kolbe [2], Hall [3], Graham [4] and Weber [5]. Data extracted from Phillips [6].

While Fig. 2.1 shows promise for the accuracy of K  chemann's analytical approach, the amount of available experimental data for evaluation is limited. Therefore this present research uses a numerical approach using potential flow in Chapter 5 to calculate the locus of section aerodynamic centers of finite wings and generate data to evaluate the accuracy of K  chemann's work. If proven to be accurate, K  chemann's analytical approach can be suggested as an input to an ongoing research attempt to improve the existing numerical lifting-line method by Phillips and Snyder [19] for swept wings.

2.3 AERODYNAMIC CENTER FOR A SPANWISE SECTION OF A FINITE WING IN INVISCID FLOW

In order to evaluate the location of the aerodynamic center at any location along the wing, sectional aerodynamic properties including axial and normal forces as well as the section pitching moment must be known. The location of the aerodynamic center is commonly assumed to lie on the airfoil chord line and lie at the point $x_{ac}/c = -\tilde{C}_{m,\alpha}/\tilde{C}_{L,\alpha}$. However, this widely used expression was developed from thin airfoil theory and neglects aerodynamic and trigonometric nonlinearities. A more accurate approach is suggested by Phillips [29]. It is used in combination with the development by Hunsaker, Pope, and Hodson [30].

The aerodynamic center including any trigonometric and aerodynamic nonlinearities can be computed from [29]

$$\frac{x_{ac}}{c} = \frac{\tilde{C}_{A,\alpha}\tilde{C}_{m,\alpha\alpha} - \tilde{C}_{m,\alpha}\tilde{C}_{A,\alpha\alpha}}{\tilde{C}_{N,\alpha}\tilde{C}_{A,\alpha\alpha} - \tilde{C}_{A,\alpha}\tilde{C}_{N,\alpha\alpha}} \quad (2.22)$$

$$\frac{y_{ac}}{c} = \frac{\tilde{C}_{N,\alpha}\tilde{C}_{m,\alpha\alpha} - \tilde{C}_{m,\alpha}\tilde{C}_{N,\alpha\alpha}}{\tilde{C}_{N,\alpha}\tilde{C}_{A,\alpha\alpha} - \tilde{C}_{A,\alpha}\tilde{C}_{N,\alpha\alpha}} \quad (2.23)$$

$$\tilde{C}_{m_{ac}} = \tilde{C}_m + \frac{x_{ac}}{c}\tilde{C}_N - \frac{y_{ac}}{c}\tilde{C}_A \quad (2.24)$$

The section axial and normal forces are related to the section lift and drag according to

$$\tilde{C}_A = \tilde{C}_D \cos \alpha - \tilde{C}_L \sin \alpha \quad (2.25)$$

$$\tilde{C}_N = \tilde{C}_L \cos \alpha + \tilde{C}_D \sin \alpha \quad (2.26)$$

Hunsaker [30] shows that the lift and pitching moment of a symmetric airfoil of arbitrary thickness distribution in inviscid flow can be expressed as

$$\tilde{C}_L = \tilde{C}_{L,\alpha} \sin \alpha \quad (2.27)$$

$$\tilde{C}_m = \tilde{C}_{m,\alpha} \sin \alpha \cos \alpha \quad (2.28)$$

The relations shown in Eqs. (2.27) and (2.28) were developed under the assumption of two-dimensional inviscid flow over a symmetric airfoil. For a finite wing in inviscid flow, the downwash shed by the finite wing produces an induced angle of attack that varies spanwise along the wing. For a wing without sweep, this downwash is greatest at the wing tips and decreases as the wing centerline is approached. The downwash has the effect of decreasing the local section angle of attack. For example, the lift distribution shown in Fig. 2.2 was obtained from inviscid computations using the high-order panel code PANAIR on an elliptic wing with a NACA 0012 airfoil, no sweep, no twist, and an aspect ratio of 8. The wing was set an angle of attack of 5 degrees. At 5 degrees angle of attack, a two-dimensional NACA 0012 airfoil generates a lift coefficient of 0.6029. This magnitude is also included in the figure for reference. From Fig. 2.2, it can be seen that no spanwise wing section achieves a lift coefficient of that magnitude due to the induced downwash.

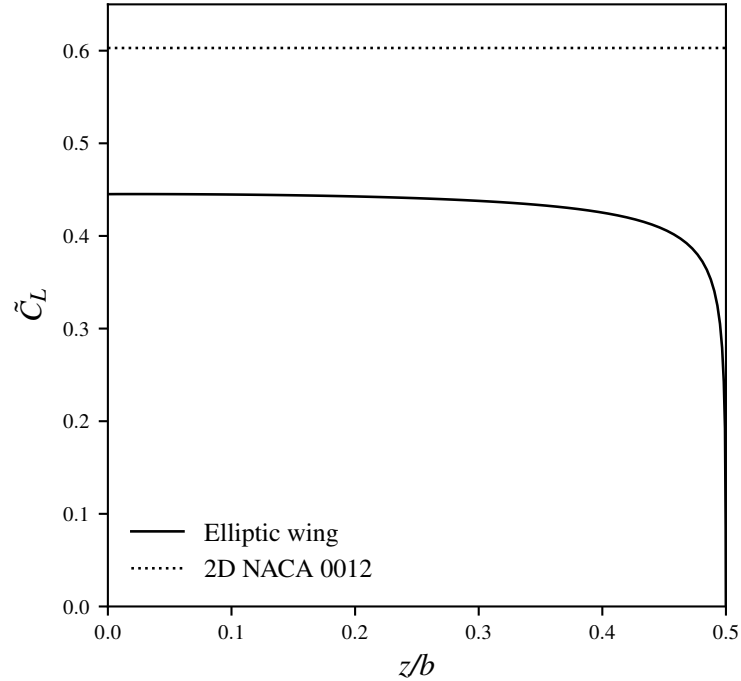


Fig. 2.2: Spanwise lift coefficient distribution for an elliptic wing using a NACA 0012 airfoil.

Figure 2.3 shows the local section lift coefficient at the wing centerline of the aforementioned unswept finite wing as a function of angle of attack. Also included is the lift coefficient as a function of angle of attack of a two-dimensional NACA 0012 airfoil in inviscid flow. The two-dimensional results can be fit to Eq. (2.27) to give $\tilde{C}_{L,\alpha} = 6.9172$ for a NACA 0012 airfoil. Results from Eq. (2.27) are included in Fig. 2.3 for comparison.

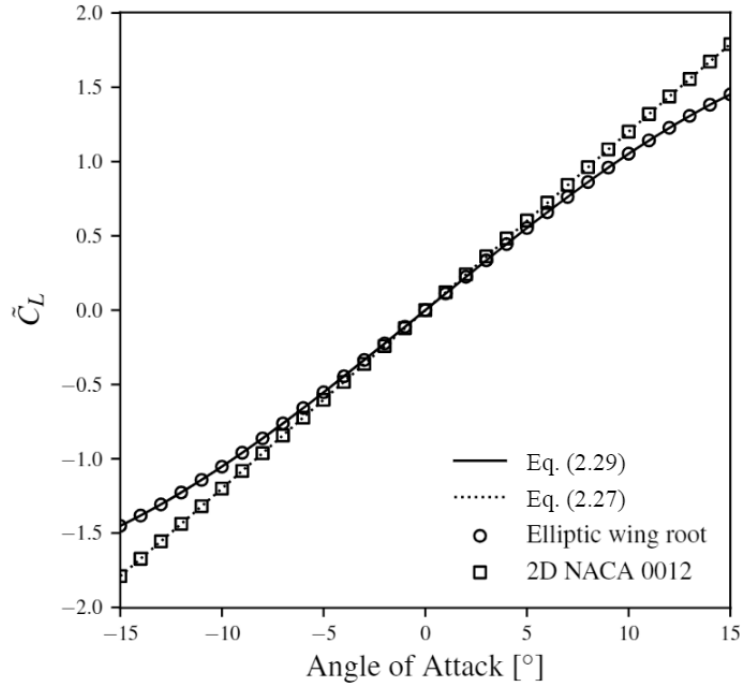


Fig. 2.3: Lift coefficient versus angle of attack at root of an elliptic wing using a NACA 0012 airfoil.

As can be seen from Fig. 2.3, the downwash has the effect of scaling the lift and changing the frequency of the sine wave associated with the lift curve. It can be shown that the section lift as a function of angle of attack at any spanwise location on a wing with a symmetric airfoil is in fact not a perfectly linear relationship but can be expressed as

$$\tilde{C}_L = \mu_L \sin(\omega\alpha) \quad (2.29)$$

where μ_L is the lift slope of the section at zero angle of attack, and ω is the frequency

defining the sine wave visible in Fig. 2.3. In the example shown in Fig. 2.3, the section data at the wing root can be fit to Eq. (2.29) by specifying $\mu_L = 1.8079$ and $\omega = 3.5621$. Results from Eq. (2.29) are included in Fig. 2.3 for comparison. Note that μ_L and ω are a function of spanwise location and depend on aspect ratio and sweep angle.

The following relation for the section pitching moment as a function of angle of attack at any spanwise location is used:

$$\tilde{C}_m = \mu_m \sin(2\alpha) \quad (2.30)$$

Using Eqs. (2.25) and (2.26) along with Eq. (2.30), differentiating twice, and applying the results to Eqs. (2.22)–(2.24) gives the aerodynamic center and associated pitching moment for any symmetric airfoil section with induced drag. This process requires a fair amount of algebraic manipulation, but can be accomplished quite quickly using a symbolic solver. The resulting relations are too lengthy to include here [31], but demonstrate that the aerodynamic center at any spanwise section is a function of angle of attack. Figure 4.8.2 on page 467 of *Mechanics of Flight* by Phillips [27] shows the dependence of aerodynamic center location on angle of attack. In the present study, only the aerodynamic center at zero degrees angle of attack is considered. For this scenario, the resulting relations for the aerodynamic center reduce to

$$\frac{x_{ac}}{c} = -\frac{2\mu_m}{\omega\mu_L} \quad (2.31)$$

$$\frac{y_{ac}}{c} = \tilde{C}_{m_{ac}} = 0 \quad (2.32)$$

The aerodynamic coefficients needed for Eqs. (2.29) and (2.30) can be obtained from a set of computational results including the section lift and pitching moment at several angles of attack. In order to obtain appropriate values for μ_L and ω at any spanwise location, a nonlinear solver is required. In order to obtain appropriate values for μ_m , a vertical least-squares method can be used to obtain an analytical solution as outlined by Hunsaker [30]. This yields

$$\mu_m = \frac{\sum_{i=1}^n \tilde{C}_{m_i} \sin(2\alpha_i)}{\sum_{i=1}^n \sin^2(2\alpha_i)} \quad (2.33)$$

Once values for μ_L , ω , and μ_m have been obtained at each spanwise section, they can be used in Eq. (2.31) to obtain the axial location of the aerodynamic center at any spanwise section. Note that μ_L and μ_m were called κ_L and κ_m by Moorthamers [32] in an earlier publication, but have been renamed to prevent conflicting with other variable names in the current research.

CHAPTER 3

COMPUTATIONAL METHODOLOGY

In the following sections, the calculation of the locus of section aerodynamic centers, global aerodynamic center, and general relations to assess the aerodynamic performance of finite, swept wings is discussed. First, Section 3.1 discusses the definitions of geometry used in this research and Section 3.2 details the numerical aerodynamic tools used, and presents grid convergence studies for each.

3.1 DEFINITION OF GEOMETRY

This section describes how wing geometry is modeled in the different methods used throughout the research. Figure 3.1 shows the coordinate system used throughout the research. The longitudinal direction is denoted by the x -axis, defined positive in the freestream direction, hence positive towards aft. The lateral y -axis is defined positive towards the right wing, and the vertical position along the z -axis follows the right-hand rule, and is therefore defined positive coming out of the page as seen from Fig. 3.1. Note that the origin is positioned at the quarter-chord location of the wing root for the majority of the research. Results drawing the locus of aerodynamic centers in Section 3.3 and Chapter 5 are drawn with the origin at $x/c = 0.25$.

The wing geometry is built up by defining the local quarter-chord positions of locations along the span of the wing, and adding the airfoil node coordinates adjusted to the local chord to that position. The root chord length is always set to unity, so the spanwise chord distribution is fully defined by the rest of the planform parameters. For tapered wing planforms, the local chord at any location along the span can be calculated using

$$c(y) = \frac{2b}{R_A(1 + R_T)} [1 - (1 - R_T)|2y/b|] \quad (3.1)$$

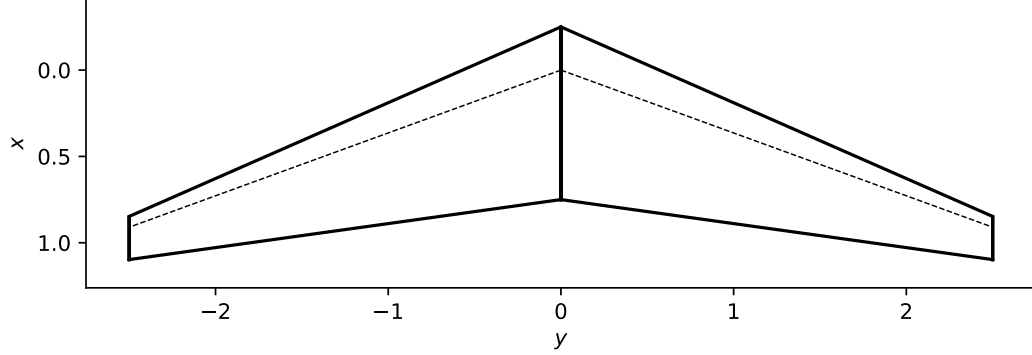


Fig. 3.1: Definition of wing coordinate system.

where R_A and R_T are the aspect and taper ratio respectively. In the case of an elliptic wing, the chord distribution is defined as

$$c(y) = \frac{4b}{\pi R_A} \sqrt{1 - (2y/b)^2} \quad (3.2)$$

The location of the quarter-chord points x_{qc} along the span of the wing depend on the wing sweep. These locations can either be freely put in, to create any arbitrary wing sweep profile, or can be defined by predetermined types of sweep. Two types of wing sweep are discussed in this research. The first is the conventional, well-known type of wing sweep where the angle of sweep is constant along the entire semispan of the wing. With the quarter-chord location of the wing root section set as the origin, and the positive x direction set in the direction of the freestream velocity, hence aft, the location of the quarter-chord points x_{qc} for a conventionally swept wing is

$$x_{qc}(y) = \tan \Lambda_{tip} \frac{2y}{b} \quad (3.3)$$

where Λ_{tip} is the angle of the imaginary line connecting the quarter-chord points of the wing root and wing tip sections. This is equal to what is generally known as $\Lambda_{c/4}$, the sweep angle of the quarter-chord line, but has been renamed. Wings where the local sweep angle of the quarter-chord line is constant along the span, will from here on be referred to as “conventionally swept wings”, or “wings with constant sweep”.

The second type of wing sweep is crescent sweep. There is no set description of the geometry of a crescent wing, beyond it generally being understood to be “half-moon shaped”. We are particularly interested in wings with a linear sweep profile, meaning one where the local sweep angle Λ of the quarter-chord sweep line is zero at the wing root, and increases linearly to some non-zero value at the tip. The local position of the quarter-chord point along different spanwise sections is given by

$$x_{qc}(y) = \tan \Lambda(y) \frac{2y}{b} \quad (3.4)$$

where $\Lambda(y)$, the angle of the imaginary line between the quarter-chord point of the wing root and the local quarter-chord point, varies along the span as

$$\Lambda(y) = \Lambda_{tip} \frac{2y}{b} \quad (3.5)$$

so that it increases linearly from zero at the root to some finite value Λ_{tip} at the tip. Figure 3.2 shows an example wing of aspect ratio $R_A = 8$, taper ratio $R_T = 0.25$ and tip sweep angle $\Lambda_{tip} = 20^\circ$. Note that the quarter-chord line, shown as a dotted line, is zero degrees at the wing root. The red line depicts the imaginary line connecting the quarter-chord points of the wing root and wing tip section. It is this line that defines the tip sweep angle $\Lambda_{tip} = 20^\circ$.

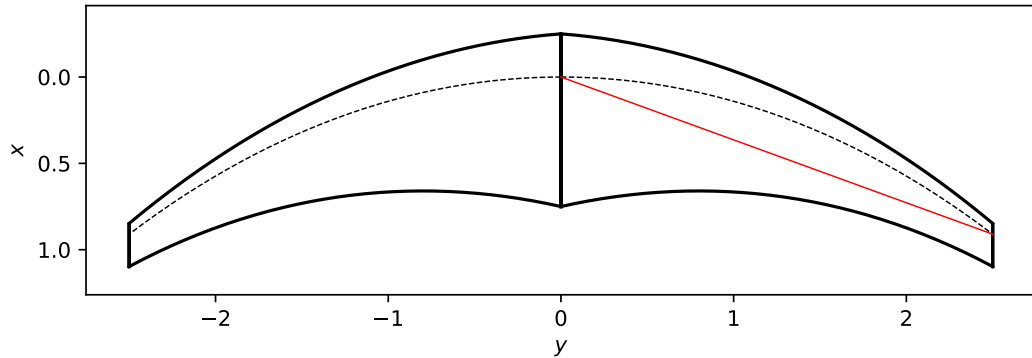


Fig. 3.2: Crescent wing with a linear sweep profile with $R_A = 8$, $R_T = 0.25$ and $\Lambda_{tip} = 20^\circ$.

Figure 3.3 shows the angle of the imaginary line connecting the quarter-chord point of the root to the quarter-chord point of any section along the span. It is plotted along half of the same wing as used in Fig. 3.2 as a function of the spanwise location, normalized by the half-span $b/2$, so that the horizontal axis runs from 0.0 to 1.0. This figure shows that the tip sweep angle of this imaginary line increases linearly along the span. We will therefore refer to wings using this kind of sweep distribution as “linearly swept wings”, “wings with linear sweep” or sometimes simply “crescent wings” from now on to distinguish them from the aforementioned wings with constant sweep.

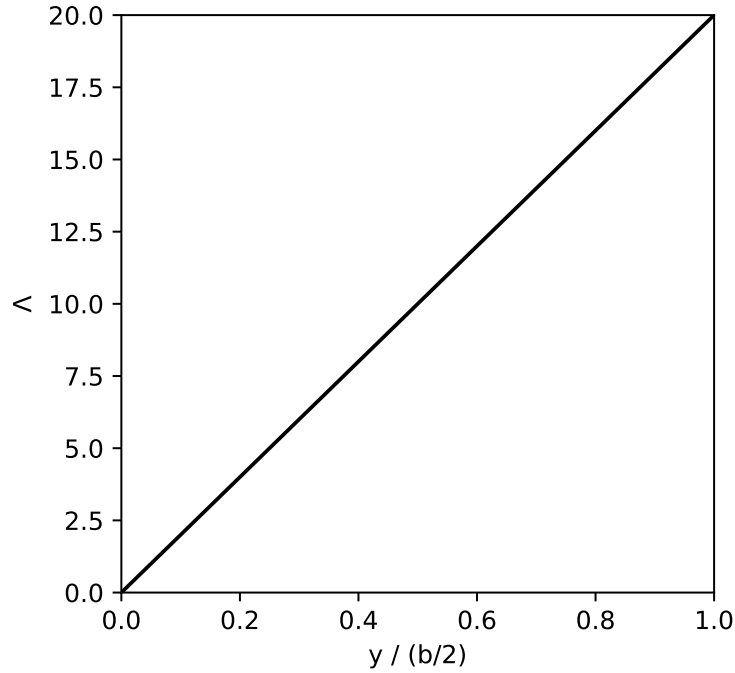


Fig. 3.3: Local sweep angle of the local quarter-chord line for a linearly swept wing with $R_A = 8$, $R_T = 0.25$ and $\Lambda_{tip} = 20^\circ$.

3.2 NUMERICAL AERODYNAMIC TOOLS

This section introduces the numerical tools used to analyze the aerodynamics of swept wings. All methods are all able to output lift, induced drag, and pitching moment coefficients. A numerical implementation of lifting-line theory and two high order panel method

are used throughout this research. A grid convergence study is presented for each method to establish them as suitable tools for use in the present research. While a well-converged method does not imply the method itself being accurate, it does ensure precision. Truncation error is the error that results from using an approximation to represent an exact formula [33]. For example, in the case of a second order polynomial being used to represent a physical phenomenon, the result takes on the shape of a parabola across a single panel. Increasing grid resolution and hence decreasing panel size allows to minimize the truncation error. Accuracy on the other hand implies closeness to reality. Since all numerical methods are approximations, none match physical reality perfectly and they all have a degree of inaccuracy. Generally speaking, methods with a higher level of fidelity will render more accurate results than methods with a lower level of fidelity. Where possible, references to other publications with validation cases are given.

For the grid convergence studies, different wings are analyzed at different sweep angles. All wing are untwisted and use a symmetric NACA 0012 airfoil with a lift-curve slope $\tilde{C}_{L,\alpha} = 6.9207$, feature a root chord of one, and are analyzed at an angle of attack $\alpha = 5^\circ$. For each method, grids of varying degrees of refinement are used to calculate and judge convergence on the resulting values for lift coefficient C_L . In the case of MachUpX and PANAIR, the finest of the grids is said to be converged if it is within a reasonable tolerance of a Richardson extrapolation for each of the sweep angles. The Richardson extrapolation is a method that can be used to estimate a numerical result as the limit of the number of nodes approaches infinity [34, 35]. Since FlightStream uses an unstructured mesh, a Richardson extrapolation can not be applied, therefore convergence is judged based on how much a fine result differs from the previous step in refinement.

Initially, this research started using PANAIR because of its open-source nature. However, because of its age, there are memory limitations hard-coded into PANAIR that prevented further grid refinement beyond what is specified in Section 3.2.2. Also, the increasing number of desired simulations, coupled with the difficulty integrating PANAIR into a modern, scripted workflow, spurred the search for a more modern tool, leading to the use of

FlightStream. Chapter 5 is wholly written using PANAIR results, whereas Chapters 4, 6, and 7 use results from FlightStream. MachUpX is only used in Chapter 4, as lifting-line as of today does not yet accurately handle wings with sweep.

3.2.1 MACHUPX

MachUpX is a tool based on the modern numerical lifting-line method by Goates [36], based on developments by Phillips and Snyder [6]. It is a numerical analog to Prandtl's classical lifting-line theory [25]. The lifting surfaces get represented by a system of discrete horseshoe vortices with their bound portion positioned along the locus of aerodynamic centers and the trailing vortices aligned with the trailing vortex sheet. The system of equations following from this representation can be solved for the unknown circulation strengths by equating the resulting force at each discrete local section along the span to the known aerodynamic properties of the airfoil used at its induced angle of attack. MachUpX utilizes recent developments by Reid and Hunsaker [20] that have increased the accuracy of the tool for finite wings with sweep. Some validation cases are given by Goates [36] and Harvey et al. [37]. Figure 3.4 shows the results for the lift coefficient and pitching moment coefficient respectively of the wing with aspect ratio $R_A = 8$ and taper ratio $R_T = 0.25$ at different sweep angles. The coarse grid features 50 nodes per semispan, the medium grid 100 nodes, and fine grid has 200 nodes.

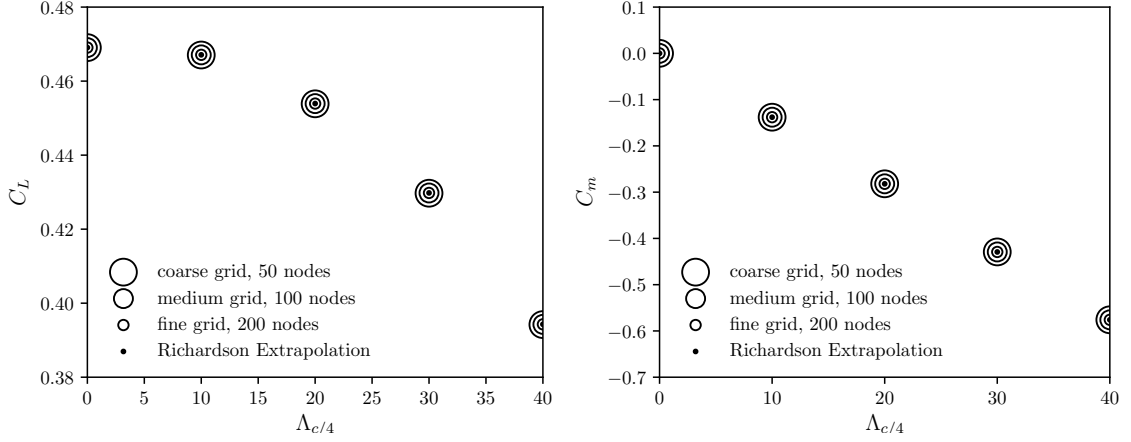


Fig. 3.4: Convergence plots for lift coefficient C_L and pitching moment coefficient C_m as calculated by MachUpX.

3.2.2 PANAIR

PANAIR is an open-source, high order panel method which uses linear potential flow theory and can be used for inviscid subsonic and supersonic flow simulations. It is high order in the sense that the singularity strengths are not constant on each panel but are allowed to vary linearly or quadratically across them. As a joint development effort from Boeing and NASA, PANAIR has enjoyed wide acceptance in the research community and has been validated multiple times in literature [38–40]. However, because of PANAIR’s strict memory limitations, a grid convergence study was done to make sure it is suited for the present research. Figure 3.5 shows the lift coefficient and pitching moment coefficient of a wing with aspect ratio $R_A = 8$ and taper ratio $R_T = 0.25$ as computed using PANAIR on a coarse (20x20 panels), medium (40x40 panels), and fine grid (80x80 panels).

While the case with a quarter-chord wing sweep of 20° shows some numerical discrepancy in its Richardson extrapolation, this is likely due to PANAIR’s rounding of calculations to four decimals. When comparing Figs 3.4 and 3.5, we see that the circles are a lot more concentric for the MachUpX results than they are for those of PANAIR. This is MachupX is already converged even on the smallest grid size, whereas PANAIR is still progressing towards full convergence. However, due to its age, PANAIR has built-in memory limitations and its grid can’t grow any more, which is part of the reason why a more modern

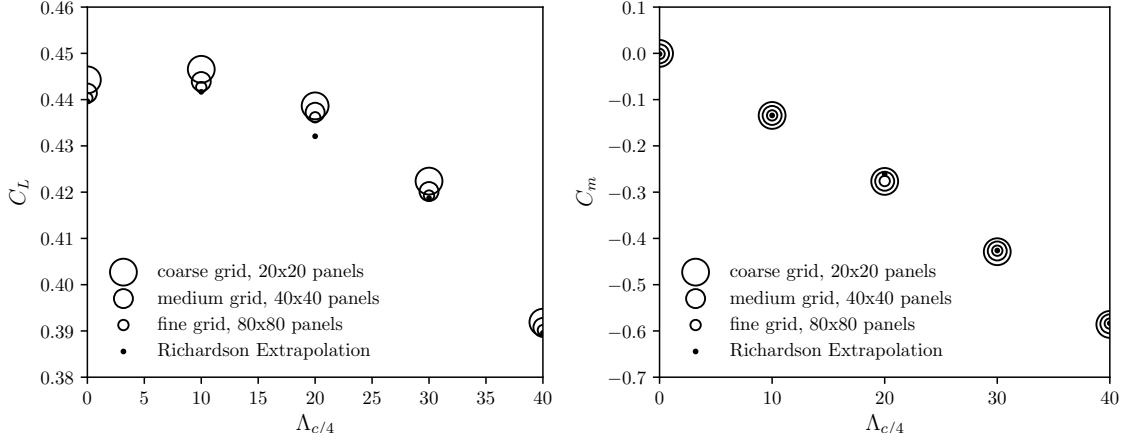


Fig. 3.5: Convergence plots for lift coefficient C_L and pitching moment coefficient C_m as calculated by PANAIR.

solution was found later in the research. Still, from Fig. 3.5, we see that the Richardson extrapolation and the fine grid results are within 1% of each other and therefore the fine grid is deemed suitable for the purpose of this research.

3.2.3 FLIGHTSTREAM

FlightStream is a commercially available panel code developed by Research in Flight (RIF) [41]. FlightStream makes use of vortex rings to model three-dimensional surface vorticity on an unstructured surface mesh. It has a correction for viscous effects of a laminar and turbulent boundary layer [24] based on a model by Standen [42] and can estimate transition based on the model by Dvorak [43]. The bulk of this study only uses the inviscid capabilities because it allows to draw powerful trends between geometry and induced drag, but a separate chapter on the effects of viscosity is included. It has been validated against experimental and high-fidelity computational fluid dynamics simulations in many recent publications [44–50]. It offers either a graphical user interface or the ability to perform simulations and output the data through scripting. The output of FlightStream is used to calculate the general relations introduced in Section 3.5 for a large design space of swept wing configurations. While RIF recommends using 80 panels around the perimeter of the airfoil, a grid convergence study is performed in spanwise direction to decide on suitable

grid dimensions. For these grid convergence studies, wings with taper ratio $R_T = 0.25$, aspect ratios $R_A = 4$ and $R_A = 20$ are analyzed at different tip sweep angles between $\Lambda_{tip} = 0$ and $\Lambda_{tip} = 40$. The wings are untwisted and use a symmetric NACA 0012 airfoil with a lift-curve slope $\tilde{C}_{L,\alpha}=6.9207$, feature a root chord of one, and are analyzed at an angle of attack $\alpha = 5^\circ$. The grid convergence studies are performed using grids with 20, 40, 80, 120, 160, and 200 panels per half-span respectively, while keeping the number of panels in chordwise direction constant at 80 panels. A grid is said to be converged if further refinement offers no significant change in result for each of the tip sweep angles.

Figure 3.6 shows the lift coefficient C_L and induced drag coefficient C_{D_i} for these wings using the grids of increasing refinement. The size of the circle denotes the fineness of the grid, with the largest circles being the most coarse, and the smallest circles being the finest grids with 200 panels in spanwise direction.

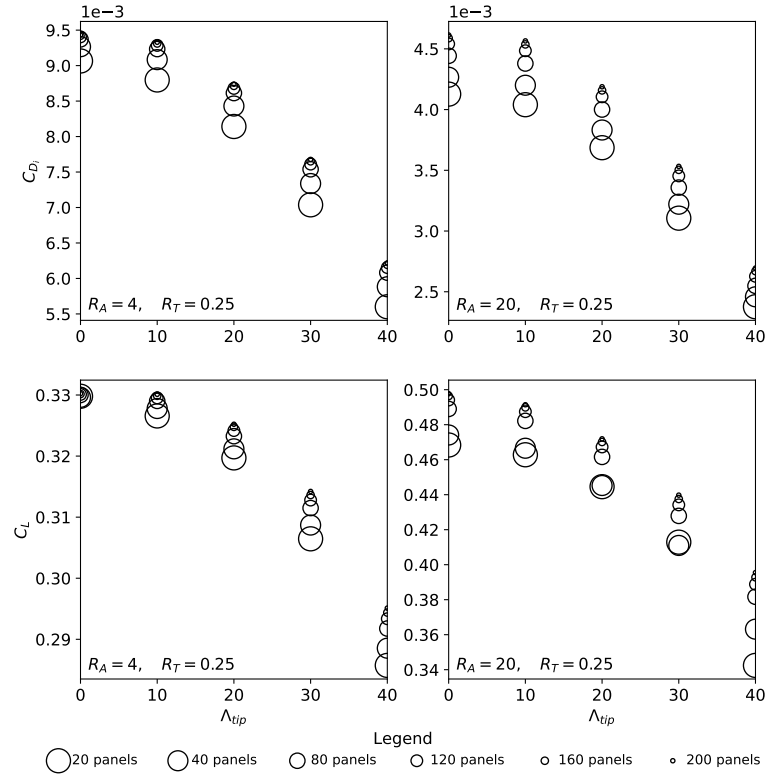


Fig. 3.6: Convergence plots for lift coefficient C_L and induced drag coefficient C_{D_i} as calculated by FlightStream for wings with $R_T = 0.25$, $R_A = 4$ and $R_A = 20$, and varying tip sweep angle Λ_{tip} .

Figure 3.7 shows the same grid convergence study but with the data represented as a percentage change from the most refined grid as $(C_{D_i} - C_{D_i, fine})/(C_{D_i, fine})$ and $(C_L - C_{L, fine})/(C_{L, fine})$.

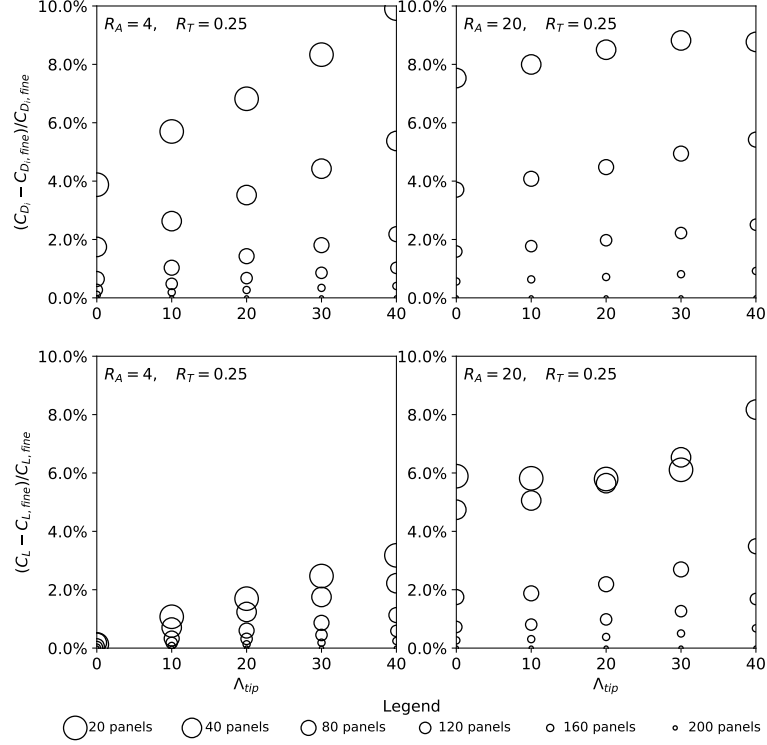


Fig. 3.7: Convergence plots for lift coefficient C_L and induced drag coefficient C_{D_i} as calculated by FlightStream for wings with $R_T = 0.25$, $R_A = 4$ and $R_A = 20$, and varying tip sweep angle Λ_{tip} , expressed as a percentage change from the most refined result.

From the distance between the circles of varying size in Fig. 3.6, we can tell that the results for lift and drag coefficients become less variable with increasing grid resolution, and hence converge to a certain value. Figure 3.7 show that the results for 160 panels in spanwise direction lie within 1% of the results using 200 panels in spanwise direction. In other words, the largest grid is only 1% more accurate than the second-largest grid. However, since computation time is proportional to N^2 , where N is the total number of panels, computations on the grid with 200 spanwise panels take 1.56 times as long as it takes for the computations with 160 panels to resolve. We therefore decide to run all simulations

in this research using a grid of 80 panels in chordwise direction by 160 panels in spanwise direction for a total of 12800 panels per half-span. The pitching-moment coefficient C_m was seen to converge in a similar fashion to the lift coefficient, but was left out of this discussion for brevity.

A crescent wing, first described in Section 3.1, is modeled using a number of spanwise airfoil definitions N_{span} . Using the minimum of two definitions, one for the root airfoil and one for the tip airfoil, a crescent wing essentially becomes a wing of constant sweep, as shown in the left hand side of Fig. 3.8. Increasing the number of spanwise airfoil definitions increases the smoothness of the crescent shape, as becomes apparent in the right hand side of Fig. 3.8, which shows a wing of the same aspect ratio, taper ratio and tip sweep as the left hand side of the figure, but with four spanwise definitions as opposed to only two.

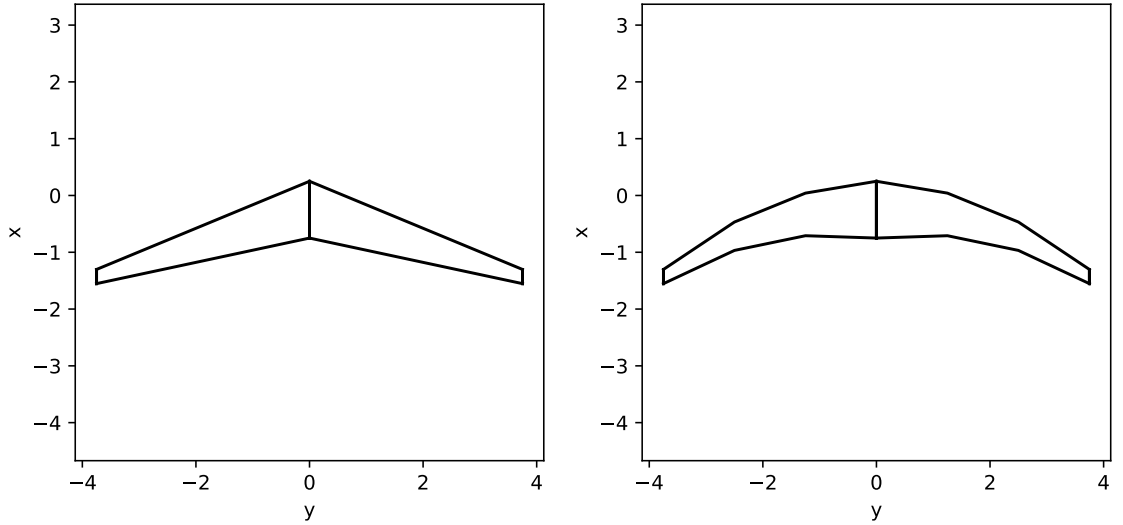


Fig. 3.8: Comparison of a crescent wing defined using two (left) and four (right) spanwise sections.

A convergence study is performed to see how many airfoil definitions are needed to represent a crescent wing with sufficient smoothness. Figure 3.9 shows the lift coefficient and induced drag coefficient for a linearly swept wing with aspect ratio $R_A = 12$, taper ratio $R_T = 0.25$, and tip sweep angle $\Lambda_{tip} = 20^\circ$ defined using $N_{span} = 2, 4, 8, 16$, or 32

spanwise sections.

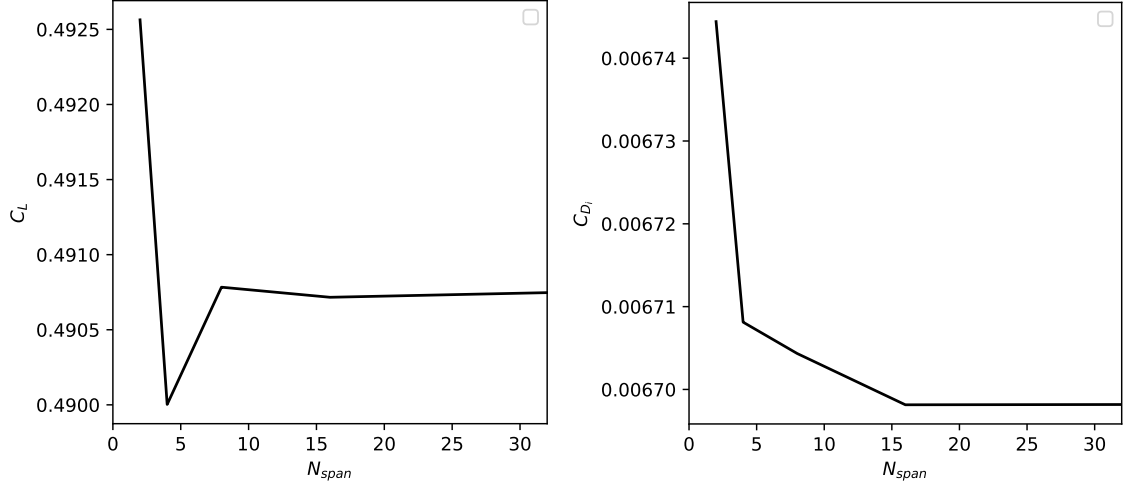


Fig. 3.9: Lift coefficient (left) and induced drag coefficient (right) for a linearly swept wing as a function of number of spanwise sections.

From Fig. 3.9 it is concluded that the results for the aerodynamic coefficients no longer vary with increasing of sections, with the results for $N_{span} = 16$ being equal to the results for $N_{span} = 32$. However, because the computation time between $N_{span} = 16$ and $N_{span} = 32$ does not differ noticeably, all crescent wings are modeled with 32 spanwise sections.

3.3 CALCULATION OF THE LOCUS OF SECTION AERODYNAMIC CENTERS

We have already seen that the locus of section aerodynamic centers can be calculated using Küchemann's analytical method presented in Section 2.2. The location of the aerodynamic center of each spanwise section using results from any numerical, or experimental method is found from

$$\frac{x_{ac}}{c} = -\frac{2\mu_m}{\omega\mu_L} \quad (3.6)$$

where ω , μ_L and μ_m are variables used in the definitions of lift and moment coefficients and defined in Section 2.3. Equation (3.6) is developed from relations for the aerodynamic center by Phillips [29] which include trigonometric and aerodynamic nonlinearities. The locus of section aerodynamic centers for a wing is then the collection of points found by applying Eq. (3.6) at each spanwise section. It is convenient to express it as a shift with respect to the two-dimensional aerodynamic center location, as given by Eq. (3.7).

$$\frac{\Delta x_{ac}}{c} = \frac{x_{ac}}{c} - \left(\frac{x_{ac}}{c}\right)_{2D} \quad (3.7)$$

where $\frac{x_{ac}}{c}$ is calculated from Eq. (3.6) using data from any numerical or experimental method and $\left(\frac{x_{ac}}{c}\right)_{2D}$ is the two-dimensional position of the aerodynamic center for a section using the same profile.

Figure 3.10 shows an example of the locus as calculated from PANAIR for two wings with an elliptic planform of aspect ratio 8, one without sweep and one with a quarter-chord sweep angle of twenty degrees. Figure 3.11 shows the deviation of the locus of aerodynamic centers of the same two wings from the location of the aerodynamic center for a two-dimensional section defined using the same profile by making use of Eq. (3.7).

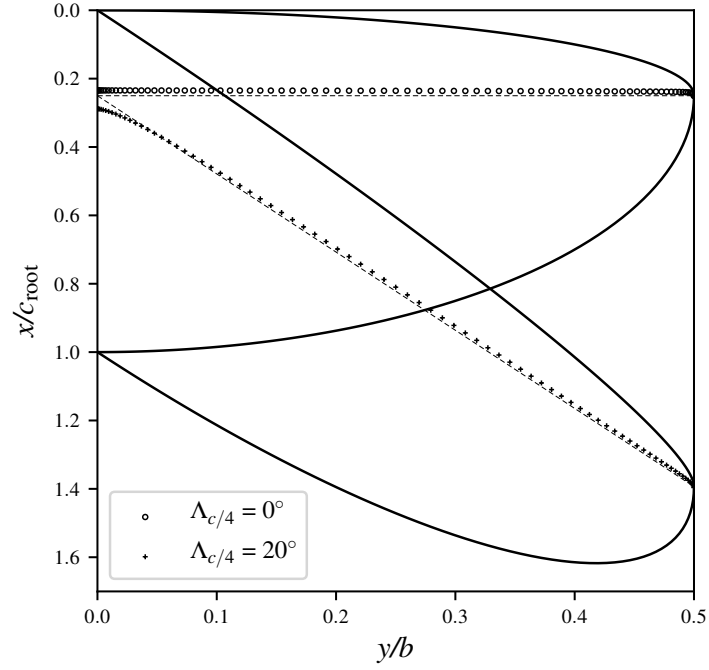


Fig. 3.10: Locus of section aerodynamic centers of two elliptic wings with varying quarter-chord sweep.

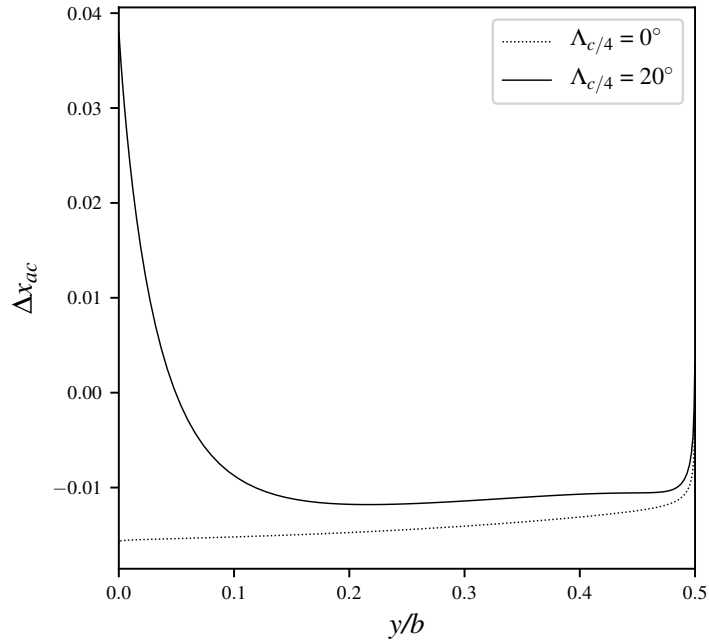


Fig. 3.11: Deviation of the locus of aerodynamic centers Δx_{ac} as computed using PANAIR for two elliptic wings with varying quarter-chord sweep.

3.4 CALCULATION OF THE GLOBAL AERODYNAMIC CENTER POSITION

All analytical and numerical computations in the present research are performed at an angle of attack of $\alpha = 5^\circ$, which is well within the range of linear aerodynamics for a symmetrical airfoil. The results for all methods include lift, induced drag, and pitching moment coefficients. Because all wings in the research use the symmetric NACA 0012 airfoil, we can calculate a lift slope $C_{L,\alpha}$ and pitching moment slope $C_{m,\alpha}$ from the results by recognizing that $C_L|_{-\alpha} = -C_L|_{\alpha}$ and $C_m|_{-\alpha} = -C_m|_{\alpha}$. From results at an angle of attack of $\alpha = 5^\circ$, the lift slope and pitching moment slope are therefore calculated using

$$C_{L,\alpha} = \frac{2 \cdot C_L|_{\alpha=5^\circ}}{10^\circ} \quad (3.8)$$

$$C_{m,\alpha} = \frac{2 \cdot C_m|_{\alpha=5^\circ}}{10^\circ} \quad (3.9)$$

The global axial position of the aerodynamic center of a wing can be calculated from

$$\frac{x_{ac}}{c_{ref}} = -\frac{C_{m,\alpha}}{C_{L,\alpha}} \quad (3.10)$$

where c_{ref} is a reference chord such as the mean aerodynamic chord.

3.5 GENERAL AERODYNAMIC RELATIONS FOR COMPARISON OF WINGS WITH AND WITHOUT SWEEP

From the lifting-line development in Section 2.1, we see that the lift slope of a finite wing without sweep can be expressed as a function of the lift-slope factor κ_L as shown in Eq. (2.8). Lifting-line theory provides an expression of κ_L directly as shown in Eq. (2.9). However, any analytical, numerical, or experimental method that can be used to predict the lift slope of a finite wing can be used to estimate κ_L by rearranging Eq. (2.8) in the form

$$\kappa_L = \frac{\tilde{C}_{L,\alpha}}{C_{L,\alpha} \left[1 + \tilde{C}_{L,\alpha}/(\pi R_A) \right]} - 1 \quad (3.11)$$

Likewise, the induced-drag factor from lifting-line theory can be directly computed from Eq. (2.11). However, it can be estimated from other aerodynamic solutions for lift and induced drag by rearranging Eq. (2.10) in the form

$$\kappa_D = C_{Di} \frac{\pi R_A}{C_L^2} - 1 \quad (3.12)$$

With these relations, we can now compare the predictions for κ_L and κ_D of the analytic solutions to computational results stemming from any numerical or experimental method.

Next we consider the aerodynamics of swept wings in terms of the deviation in the lift slope, induced-drag, and aerodynamic center relative to the straight-wing solution without sweep. In previous research [51], an induced drag factor was introduced to quantify the influence of sweep on the induced drag coefficient C_{Di} . However, this factor was dependent on lift coefficient C_L , making comparisons between different wings difficult. Therefore, this research expands the use of κ_D from Eq. (3.12) to wings with sweep as well. It can then be seen as a penalty in induced drag of a certain wing with respect to a wing with the same aspect ratio R_A and taper ratio R_T without sweep featuring the elliptic spanwise lift distribution.

The change in lift slope due to sweep is evaluated using a lift-slope sweep factor δ_L defined as

$$\delta_L = \frac{C_{L,\alpha}}{(C_{L,\alpha})_{\Lambda=0}} \quad (3.13)$$

The change in aerodynamic center due to sweep is evaluated using an aerodynamic-center sweep factor κ_{ac} defined as

$$\kappa_{ac} = \frac{x_{ac}}{c_{ref}} - \frac{(x_{ac})_{\Lambda=0}}{c_{ref}} \quad (3.14)$$

After calculating the aerodynamic center position using Eq. (3.10), all information is known to determine the lift slope correction factor due to taper and aspect ratio κ_L , the induced drag correction factor κ_D , the change in lift slope due to sweep δ_L , and the change in aerodynamic center κ_{ac} due to sweep. These can be computed using Eqs. (3.11),

(3.12), (3.13), and (3.14) respectively from numerical results. These are used in the following chapters to compare the different analytical and numerical methods and gain understanding of subsonic aerodynamics.

CHAPTER 4

AERODYNAMIC PROPERTIES OF WINGS WITHOUT SWEEP IN INVISCID FLOW

This chapter discusses the analyses of wings without sweep using Prandtl’s analytic lifting line solution, the numerical lifting line algorithm MachUpX, and the inviscid panel code FlightStream. The two numerical methods were discussed in Section 3.2. Results for κ_L and κ_D are shown for all methods for wings without sweep of varying aspect ratio and taper ratio.

4.1 RESULTS FOR LIFT

A set of 900 wings without sweep but with varying aspect ratios and taper ratios is analyzed using Prandtl’s analytic lifting line solution, the modern implementation of numerical lifting-line, MachUpX, and the inviscid panel code, FlightStream. The planform design variables are shown in Table 4.1.

Table 4.1: Planform variables for unswept wing analysis.

	Minimum	Maximum	Interval
R_A	4	20	2
R_T	0.01	1.00	0.01

Note that wings with $R_T = 0.0$ produced errors in some numerical methods, therefore the lower limit is $R_T = 0.01$. All wings are untwisted, feature symmetric NACA 0012 airfoils and a root chord of one, and all computations were done at an angle of attack of 5 degrees.

It is well known that the elliptic lift distribution produces minimum induced drag for a given lift coefficient. This can be produced by an elliptic planform without sweep. However, difficulties in manufacturing an elliptic planform and other considerations resulted in the tapered wing planform as a common compromise. Correction factors κ_L and κ_D can be

used to determine the lift slope and induced drag coefficient of tapered planforms. At a fixed angle of attack, κ_L and κ_D , as calculated using Eqs. (3.11) and (3.12), can be seen as penalties of aerodynamic performance of these tapered wings as compared to their elliptical counterparts.

The classic lifting-line result for κ_L is computed from the Fourier series using Eq. (2.9). With data from any numerical method, κ_L can be calculated from Eq. (3.11). Figure 4.1 shows κ_L as a function of taper ratio with lines for different aspect ratios. Lines show increasing opacity for increasing aspect ratio from $R_A = 4$ to $R_A = 20$, with the interval between two subsequent lines being a change in aspect ratio of two.

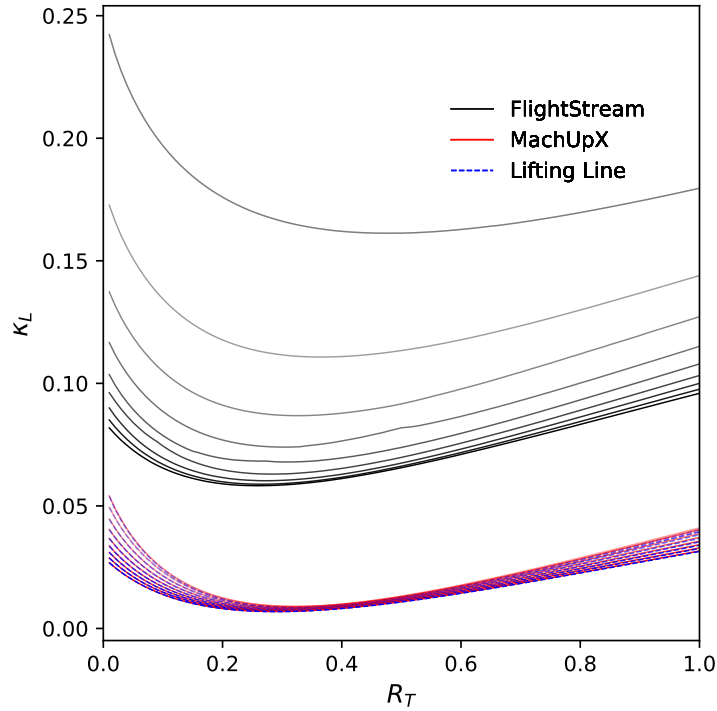


Fig. 4.1: Lift slope correction factor due to taper κ_L as a function of taper ratio R_T for wings with zero sweep.

While the results for classic lifting-line and MachUpX provide a nearly perfect match for κ_L , those computed using FlightStream are significantly higher. There are a couple of possible explanations for this. It has to be noted that Eq. (3.11) is very sensitive to $C_{L,\alpha}$.

For example, the lift curve slope of an unswept wing of aspect ratio $R_A = 4$ and taper ratio $R_T = 0.25$ is 4.417 as computed using MachUpX and 3.814 according to FlightStream. While this is a difference of only 16%, Fig. 4.1 shows that κ_L differs by an order of magnitude. The results are in slightly better agreement for high R_A when compared to low R_A , which is likely due to the increased accuracy of the lifting-line method at high aspect ratio.

4.2 RESULTS FOR INDUCED DRAG

The drag correction factor due to taper κ_D follows from classic lifting-line by Eq. (2.11). Using a numerical method, it can be calculated from Eq. (3.12). Figure 4.2 shows κ_D as calculated using classic lifting-line, MachUpX, and FlightStream. Lines with the lowest opacity indicate the lowest aspect ratio $R_A = 4$, and each subsequent increase in opacity represents an increase of aspect ratio with 2, until the highest aspect ratio $R_A = 20$.

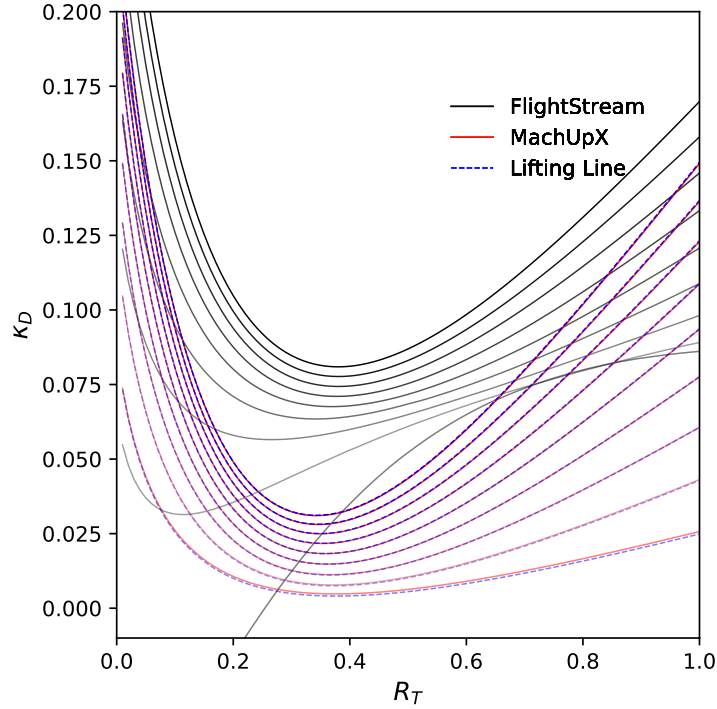


Fig. 4.2: Induced drag correction factor due to taper κ_D as a function of taper ratio R_T for wings with zero sweep.

It can be seen from Fig. 4.2 that results from analytic lifting-line and MachUpX are in near perfect agreement. For untwisted wings, the optimal taper ratio with the lowest induced drag lies around $R_T = 0.4$, which is in line with historic findings. It's interesting to note that FlightStream predicts negative values for κ_D at aspect ratio $R_A = 4$ and taper ratios below roughly $R_T = 0.2$. This suggests that these particular wings are more aerodynamically efficient than wings with an elliptic spanwise lift distribution. It is not certain whether this is physically true, or an artifact from numerical simulation. It has to be remembered that the elliptic lift distribution being the most efficient and leading to the lowest possible induced drag is only a finding from classical lifting-line theory, and it is possible that this does not hold for aspect ratios as low as $R_A = 4$. The wake and surface pressure solution from FlightStream of a wing with aspect ratio $R_A = 4$, taper ratio $R_T = 0.01$, and induced drag factor $\kappa_D = -0.066$, shown in Fig. 4.3, show no reason to believe the solution is invalid. One theory is that the combination of very low taper ratio with a low aspect ratio results in very high angles for the leading and trailing edges, potentially resulting in a high sweep effect.

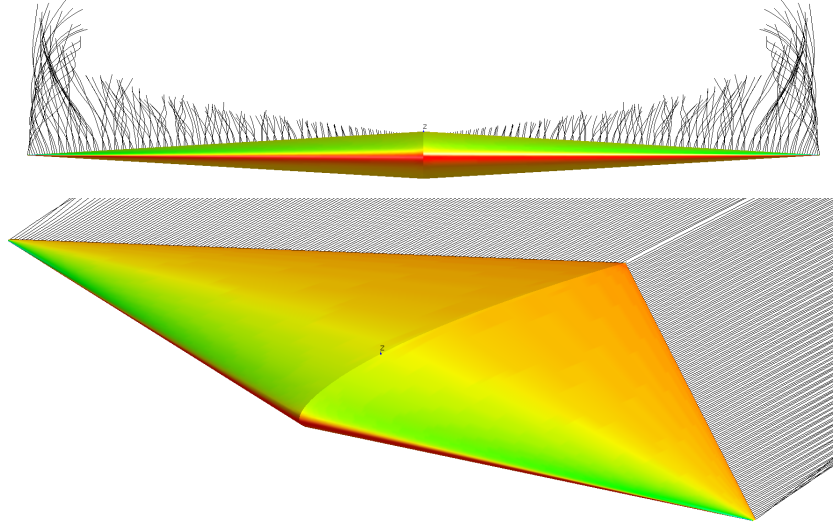


Fig. 4.3: Front view and isometric view of FlightStream results of wake and surface pressure field of a wing with aspect ratio $R_A = 4$, taper ratio $R_T = 0.01$, and induced drag factor $\kappa_D = -0.066$.

CHAPTER 5

EVALUATION OF KÜCHEMANN’S ANALYTIC SOLUTIONS FOR WINGS WITH CONSTANT SWEEP

This chapter evaluates the accuracy of Küchemann’s analytic solution for the locus of section aerodynamic centers as presented in Section 2.2 using wings with an elliptic planform. Section 5.1 analyzes wings with constant, rearward sweep, Section 5.2 studies the effects of thickness variation, and Section 5.3 studies wings with constant, forward sweep.

5.1 RESULTS FOR CONSTANT REARWARD SWEEP

The locus of section aerodynamic center locations as calculated using Küchemann’s analytical method given by Eq. (2.21) is here compared to results from PANAIR. For the purpose of the present research, all wings investigated feature a NACA 0012 profile. The lift curve slope of this profile is calculated with a two-dimensional vortex panel method to be $\tilde{C}_{L,\alpha} = 6.9207$. The aerodynamic center of a NACA 0012 airfoil is found to lie at $(x_{ac}/c)_{2D} = 0.2619$ using the same vortex panel method.

To evaluate the accuracy of Küchemann’s analytic solution to the locus of aerodynamic centers, multiple numerical simulations were run using swept, elliptic wings over a wide range of aspect ratios and quarter-chord sweep angles. Table 5.1 defines limits to a range of design parameters of the swept elliptic wings for which the locus of aerodynamic centers is calculated.

Table 5.1: Planform variables for evaluation of Küchemann’s analytic solution to the locus of aerodynamic centers.

	Minimum	Maximum	Interval
$\Lambda_{c/4} [^\circ]$	0	40	1
R_A	4	30	2

An evaluation of the accuracy of Küchemann's theory is made at each individual span-wise section by taking the difference of the shift in aerodynamic center location as calculated using the numerical method, using Eq. (3.7), and analytical method, using Eq. (2.21), as

$$E_{x_{ac}/c} = \left(\frac{\Delta x_{ac}}{c} \right)_{\text{PANAIR}} - \left(\frac{\Delta x_{ac}}{c} \right)_{\text{Küchemann}} \quad (5.1)$$

Figure 5.1 shows $E_{x_{ac}/c}$ along the complete wing semispan for varying quarter-chord sweep angles with constant aspect ratio $R_A = 8$. It can be seen that as the wing sweep increases and hence the locus moves away from the two-dimensional aerodynamic center, the difference between the numerical and analytical result increases over the whole span. It stays within 1% of the local chord for 90% of the semispan for all sweep angles, only increasing beyond that at the tip, where the small local chord amplifies the differences. Note that at high enough sweep angles, $E_{x_{ac}/c}$ is positive at the wing tip as opposed to negative for low sweep angles. This means that Küchemann predicts a farther shift aft than the numerical approach at low sweep angles whereas at higher sweep angles the numerical prediction will lie aft of the analytical result.

To see the effect of aspect ratio on the accuracy of Küchemann's theory according to Eq. (5.1), Fig. 5.2 shows $E_{x_{ac}/c}$ for wings with a quarter-chord sweep angle $\Lambda_{c/4} = 20^\circ$ and different aspect ratios. Note that the accuracy greatly decreases with decreasing aspect ratio, but the analytic result still lies within 2.5% of the local chord length from the numerical result for the lowest aspect ratio. It can be seen that Küchemann's theory becomes more accurate with increasing aspect ratio.

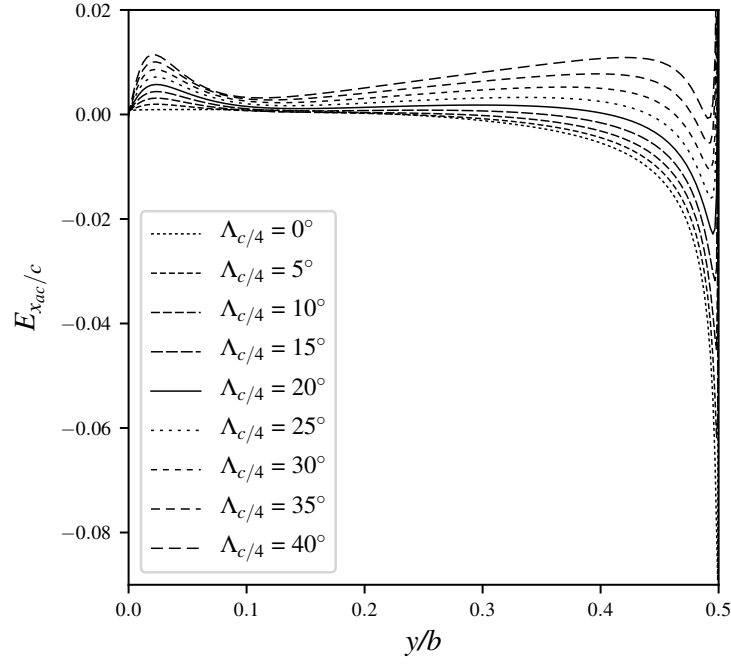


Fig. 5.1: $E_{x_{ac}/c}$ as a function of spanwise position for wings of $R_A = 8$ and different quarter-chord sweep angles.

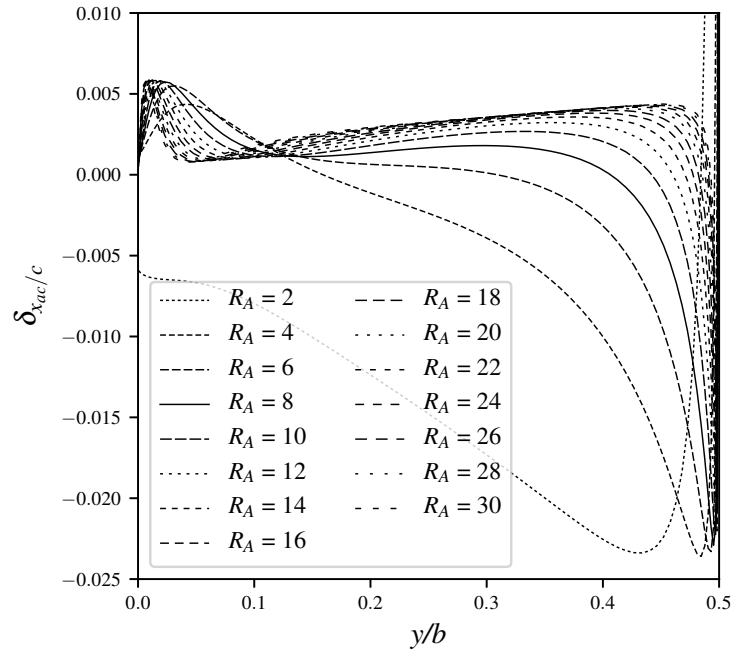


Fig. 5.2: $E_{x_{ac}/c}$ as a function of spanwise position for wings with $\Lambda_{c/4} = 20^\circ$ and different aspect ratios.

Figure 5.3 shows how far the local aerodynamic center at the root section shifts from the two-dimensional aerodynamic center location for wings of varying sweep and aspect ratio using a NACA 0012 profile. The curves show the prediction using Küchemann's approach as a function of aspect ratio with different lines for different sweep angles, while the dots indicate the numerical results using PANAIR. It shows that for increasing wing sweep the local section aerodynamic center moves aft. For increasing aspect ratio, the local section aerodynamic center moves aft until it reaches a nearly constant shift, with $(\Delta x_{ac}/c)_{root}$ not increasing with aspect ratio beyond roughly $R_A = 12$. This means that as aspect ratio approaches infinity, $(\Delta x_{ac}/c)_{root}$ approaches Küchemann's analytic approximation for aerodynamic center position at the root of an infinite wing with sweep given by Eq. (2.12). It can be seen that the analytical and numerical prediction of the shift at the root section line up very well for swept wings.

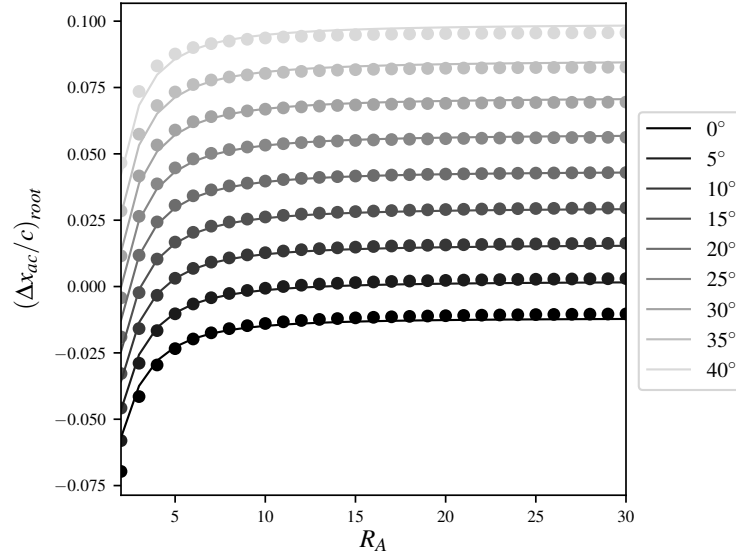


Fig. 5.3: $\Delta x_{ac}/c$ at center section for elliptic wings as a function of aspect ratio and sweep angles.

For an overview of how accurate Küchemann's approach is for the full set of wing designs as defined in Table 5.1, the root mean square error is defined as:

$$RMS = \sqrt{\frac{1}{n} \left((E_{x_{ac}/c})_1^2 + (E_{x_{ac}/c})_2^2 + \dots (E_{x_{ac}/c})_n^2 \right)} \quad (5.2)$$

Here, $(E_{x_{ac}/c})_n$ is the difference between the section aerodynamic center location as predicted by PANAIR and Küchemann as defined in Eq. (5.1). It is calculated at each spanwise location with a total of $n = 80$ sections along the semispan. Figure 5.4 shows the root mean square error as a function of aspect ratio for lines of constant sweep angle on a logarithmic vertical axis.

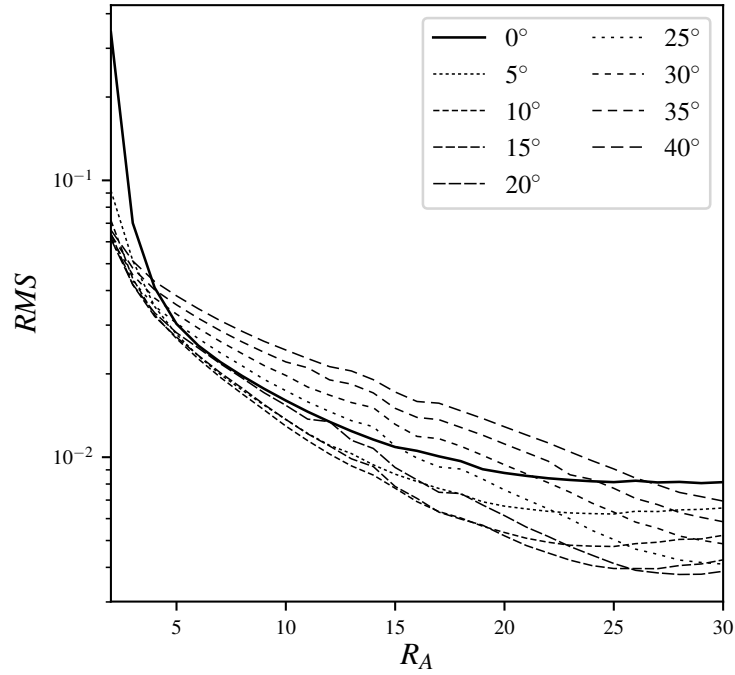


Fig. 5.4: Root mean square error of $E_{x_{ac}/c}$ as a function of aspect ratio and quarter-chord sweep angle for all wings defined in Table 5.1.

From Fig. 5.4 one can deduce that for wings with an aspect ratio higher than $R_A = 5$, the RMS is below 4% of the local chord. Because of the small chord of an elliptic wing near the wing tip, the difference $E_{x_{ac}/c}$ in this region is magnified and carries a significant

weight in the *RMS* calculation. From visual inspection of Figs. 5.1 and 5.2 we see that $E_{x_{ac}/c}$ is significantly smaller in magnitude across the majority of the span than it is at the outermost portion of the wing. Therefore, the *RMS* is skewed by this tip region and the overall error is smaller than suggested by Fig. 5.4. Küchemann’s analytic solution for the locus of section aerodynamic centers therefore is very close to the numerical result predicted using PANAIR.

5.2 RESULTS FOR THICKNESS VARIATION

Figure 5.4 shows that Küchemann’s analytic derivation offers a reasonable approach to calculating the locus of section aerodynamic centers for swept elliptic wings featuring a NACA 0012 profile with an aspect ratio between 2 and 30 and a quarter-chord sweep angle between 0 and 40 degrees. To see whether this theoretical approach is valid over a wider range of wing designs, wings with a thickness-to-chord ratio of between 12% and 21% are investigated. Table 5.2 describes the airfoils used in the investigation, their respective lift curve slopes $\tilde{C}_{L,\alpha}$ and the location of their aerodynamic center for a profile in two-dimensional flow $(x_{ac}/c)_{2D}$ as calculated using a vortex panel method.

Table 5.2: Airfoil Data.

Airfoil	$\tilde{C}_{L,\alpha}$	$(x_{ac}/c)_{2D}$
NACA 0012	6.9207	0.2619
NACA 0015	7.0885	0.2657
NACA 0018	7.2515	0.2696
NACA 0021	7.4152	0.2738

Figure 5.5 show the root and tip region of an elliptic wing with aspect ratio $R_A = 8$ and $\Lambda_{c/4} = 20^\circ$ using all airfoils from Table 5.2. It shows the locus of aerodynamic centers as calculated using Küchemann’s analytic solution as well as using PANAIR data.

As can be seen in Fig. 5.5, Küchemann’s analytic solution correctly captures the trend due to thickness, where the locus is seen to move forward for increasing wing thickness.

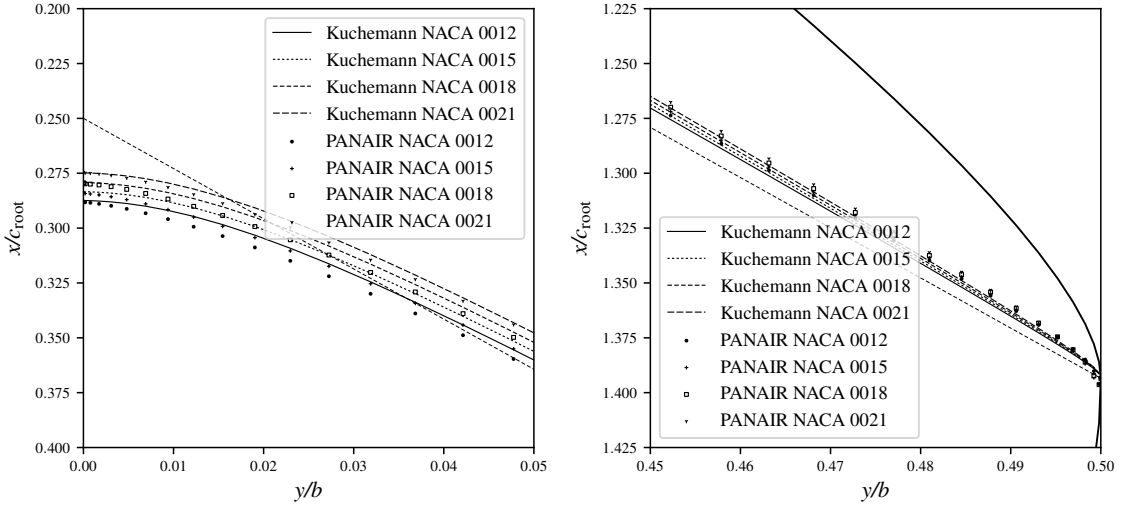


Fig. 5.5: Magnified view of the locus of section aerodynamic centers near the center and tip regions of a wing of $R_A = 8$ and $\Lambda_{c/4} = 20^\circ$ and varying profile thickness. Quarter-chord is indicated by the dashed line.

Figure 5.6 shows $E_{x_{ac}/c}$ as calculated using Eq. 5.1 for the same elliptic wing with aspect ratio $R_A = 8$ and $\Lambda_{c/4} = 20^\circ$ using all thicknesses mentioned in Table 5.2.

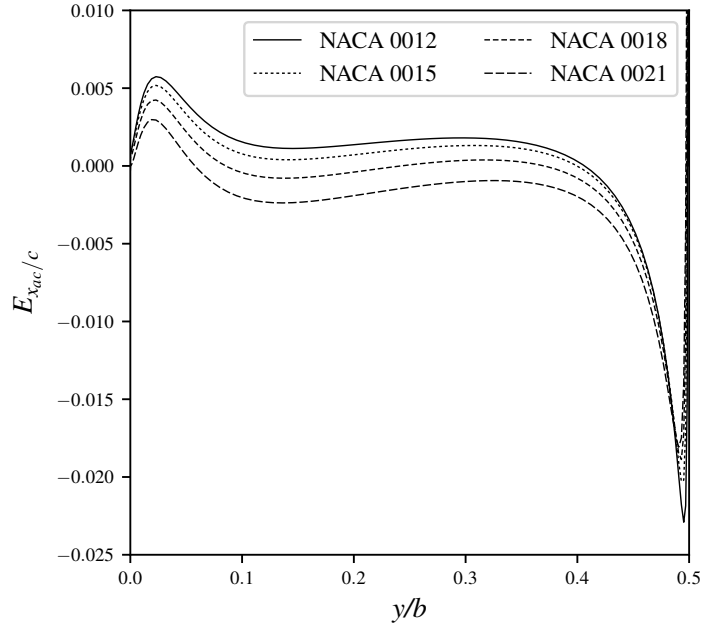


Fig. 5.6: $E_{x_{ac}/c}$ for an elliptic wing $R_A = 8$ and $\Lambda_{c/4} = 20^\circ$ and varying profile thickness as a function of spanwise position.

From Fig. 5.6, the magnitude of $E_{x_{ac}/c}$ seems to decrease for increasing airfoil thickness over the majority of the wing span. However, Fig. 5.7, showing the root mean square error over a wide range of wings with geometry defined by Table 5.1 and thicknesses defined by Table 5.2, does not necessarily reflect that. Isolating the lines for wings with quarter-chord sweep $\Lambda_{c/4} = 20^\circ$ into Fig. 5.8, the RMS is actually seen to increase for increasing airfoil thickness over all aspect ratios tested.

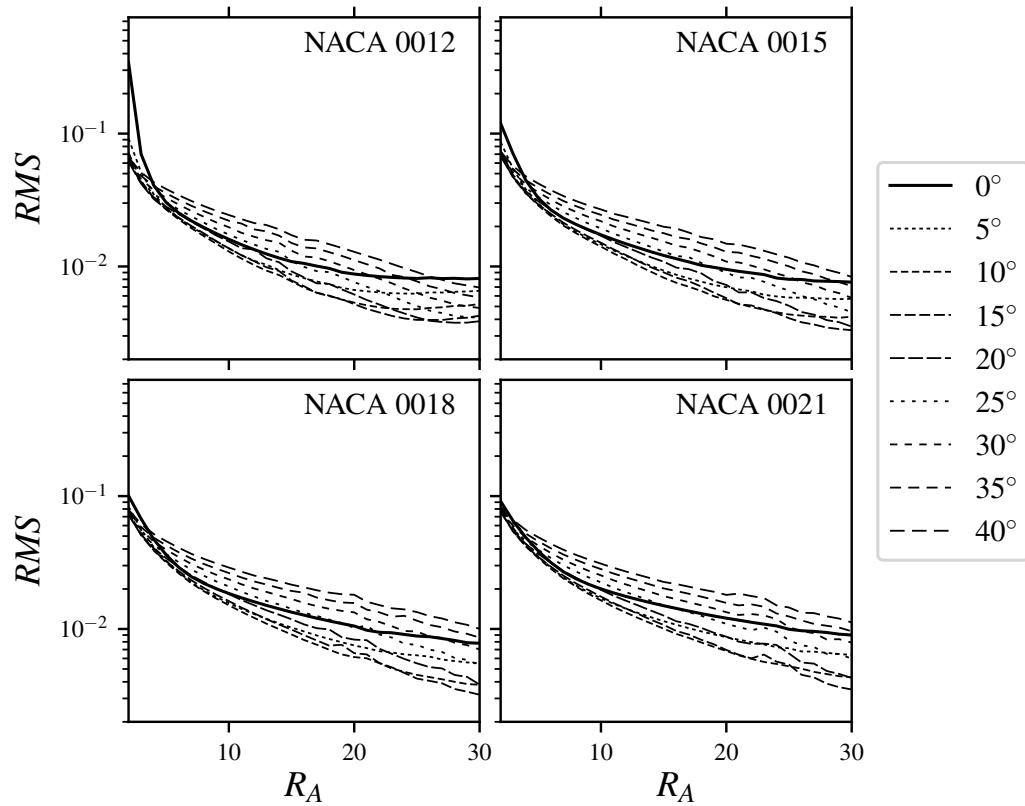


Fig. 5.7: Root mean square error of $E_{x_{ac}/c}$ for all wings defined in Table 5.1 for different profile thicknesses defined in Table 5.2.

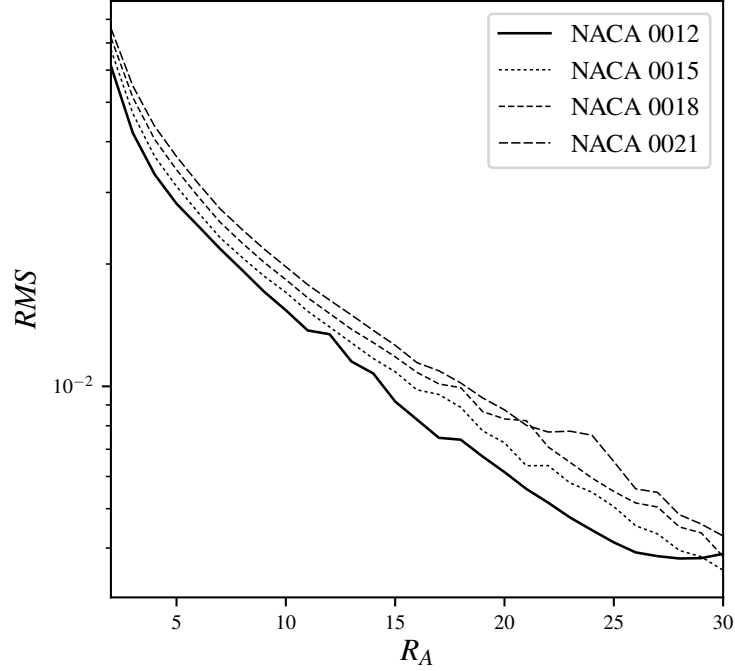


Fig. 5.8: Root mean square error of $E_{x_{ac}/c}$ for wings with a sweep angle of $\Lambda_{c/4} = 20^\circ$ as a function of aspect ratio for different profile thickness.

From Fig. 5.5 we get an idea of why this happens. The differences between Küchemann and PANAIR at the tip are larger for thicker airfoils. Since the chord is small and hence $E_{x_{ac}/c}$ is large at the tip, the RMS is greatly magnified. However, over the majority of the span, the numerical and analytical results match very closely. Despite the slight increase in RMS with increasing thickness, Fig. 5.7 shows that it is still below 4% for all wings of aspect ratios lower than $R_A = 5$ and therefore Küchemann's analytic approach gives a reasonable estimation for the locus of section aerodynamic centers.

5.3 RESULTS FOR CONSTANT FORWARD SWEEP

This section discusses the accuracy of Küchemann's analytic derivation for the locus of section aerodynamic centers for forward-swept wings. Wings with forward sweep can be of interest to aircraft designers because of their favorable properties at high angles of attack. Their inboard sections will stall first, allowing aileron control authority at high angles of attack. They are also suggested to be beneficial for use in wing designs with natural laminar

flow. With the advent of composite structures, forward-swept wings are more feasible to produce and hence might see an increased use in aircraft design. [52]

Figure 5.9 shows an elliptic wing of aspect ratio $R_A = 8$ and a quarter-chord sweep angle of $\Lambda_{c/4} = -20^\circ$ and its locus of section aerodynamic centers as calculated by Küchemann's theory as well as calculated using the numerical panel method. The locus moves forward near the wing root, opposite to the behavior present in a wing swept backwards.

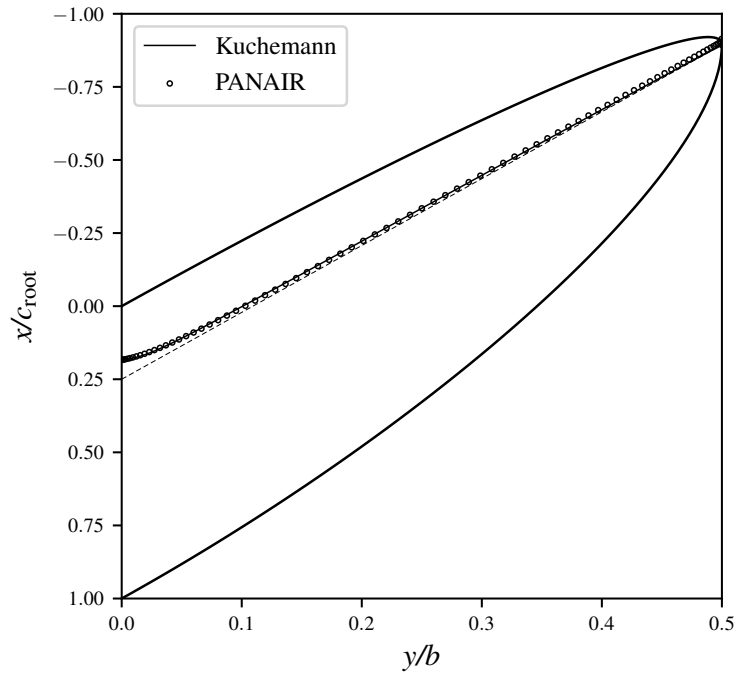


Fig. 5.9: Locus of section aerodynamic centers for a wing of $R_A = 8$ and $\Lambda_{c/4} = -20^\circ$. Quarter-chord is indicated by the dashed line.

Figure 5.10 shows a zoomed view of the root region and tip region, respectively, for all wing thicknesses in Table 5.2. It can be seen that the numerical and analytical approach match well in the root region, with the difference between numerical and analytical result increasing for increasing thickness. However, while Küchemann predicts the locus to follow the quarter chord closely out towards the tip, the numerical approach using PANAIR shows it to move forward in the outer regions of the wing.

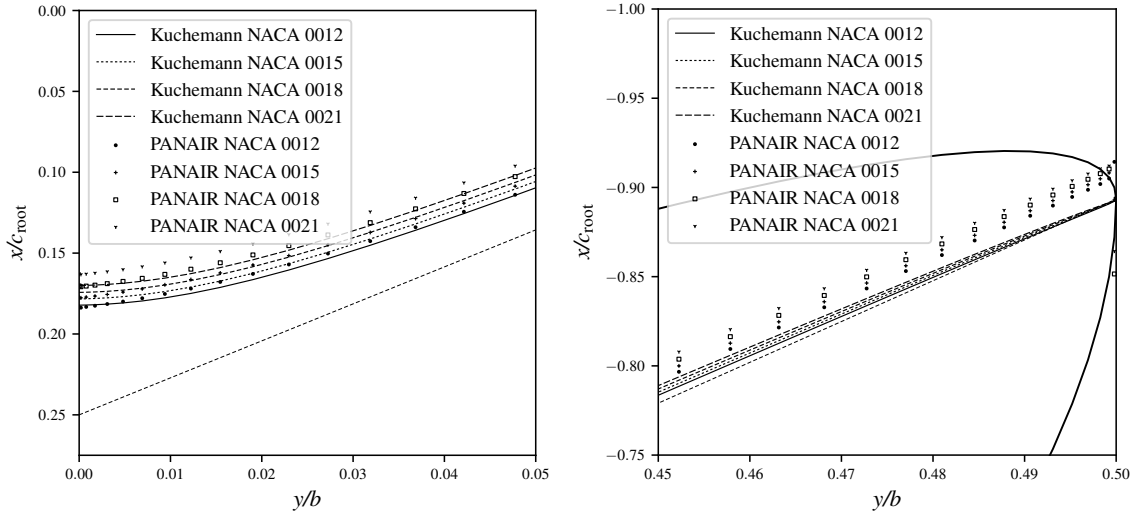


Fig. 5.10: Magnified view of the locus of section aerodynamic centers near the center and tip regions of a wing of $R_A = 8$ and $\Lambda_{c/4} = -20^\circ$ and varying profile thickness. Quarter-chord is indicated by the dashed line.

The behavior at the tip shown in Fig. 5.10 suggests a bad prediction of the locus by Kuchemann as compared to the numerical calculation and a high negative value for $E_{x_{ac}/c}$, as is confirmed in Fig. 5.11 for all profile thicknesses defined in Table 5.2. Note that the lower limit on the vertical axis was chosen for plotting purposes, but that the difference $E_{x_{ac}/c}$ does in fact exceed 25% of the local chord length.

On first inspection, with the exception of the very outboard portion of the wing, Fig. 5.11 suggests that Kuchemann's analytic derivation correctly predicts the locus of section aerodynamic centers over the majority of the span of this particular elliptic wing of aspect ratio $R_A = 8$ and a quarter-chord sweep angle of $\Lambda_{c/4} = -20^\circ$.

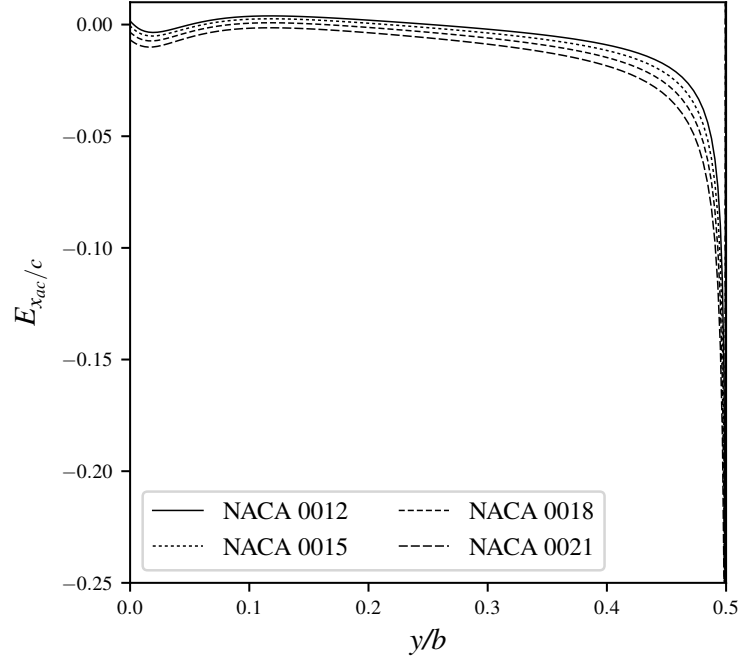


Fig. 5.11: $E_{x_{ac}}/c$ for a wing with $R_A = 8$ and $\Lambda_{c/4} = -20^\circ$ as a function of spanwise position for varying profile thickness.

To evaluate Küchemann's analytic derivation over a wide range of forward-swept wing designs, the root mean square error as defined by Eq. (5.2) is calculated for the wings defined in Table 5.3. The aerodynamic data from Table 5.2 was used. The results for the RMS across the whole design space of forward-swept wings are shown in Fig. 5.12.

Table 5.3: Planform variables for evaluation of Küchemann's analytic solution to the locus of aerodynamic centers of forward swept wings.

Design Parameter	Value	Step Size
$\Lambda_{c/4}$ [°]	0 – -40	-1
R_A	2 – 30	1
Airfoil	NACA 0012 – 0021	3%

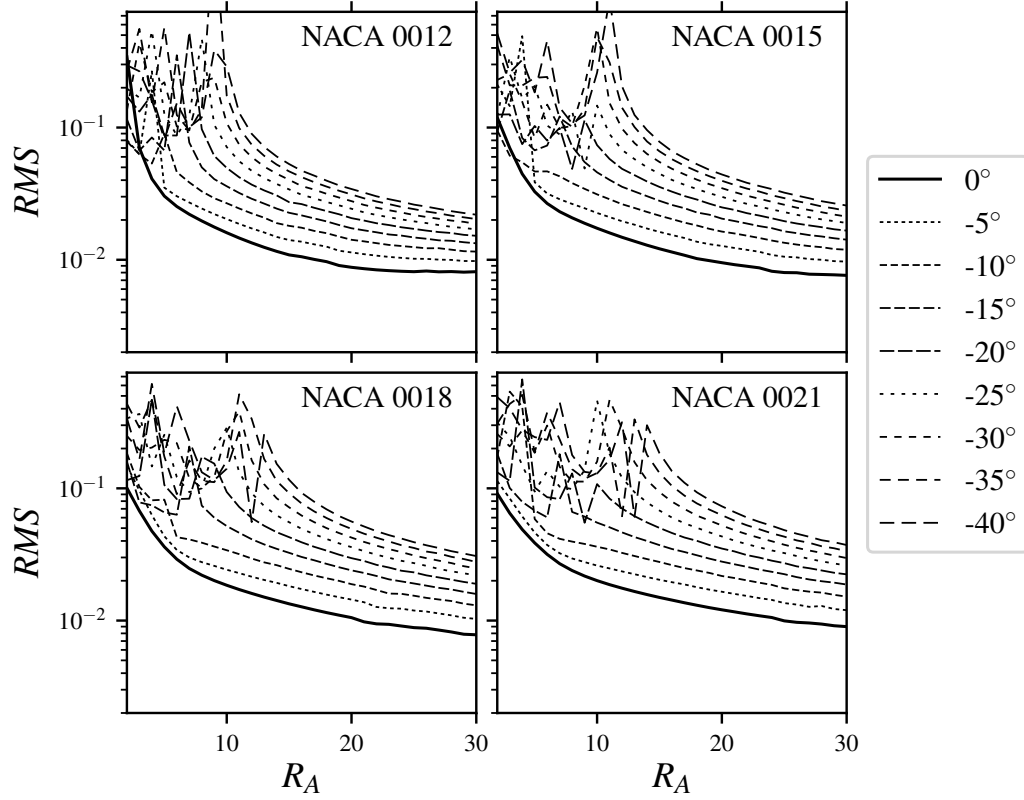


Fig. 5.12: Root mean square error of $E_{x_{ac}/c}$ for all wings defined in Table 5.3 as a function of aspect ratio and sweep angle.

Comparing Fig. 5.12 to Fig. 5.7 and using the zero-sweep curve as a reference shows that overall, the RMS is higher for the forward-swept wings than for the wings with a positive sweep angle. This is due to the incorrect prediction of the moving forward of the locus in the outboard portion of the wing as pointed out in the discussion of Fig. 5.10. The peaks present at low aspect ratios are due to some specific aspect ratio and sweep combinations that cause numerically erratic behavior within PANAIR.

Figure 5.13 shows the deviation of the aerodynamic center from its two-dimensional position as calculated by both the analytical and numerical approach at the root section of wings using a NACA 0012 profile as a function of aspect ratio for varying forward sweep angles. Figure 5.10 shows that for that particular wing with aspect ratio $R_A = 8$ and quarter-chord sweep angle of $\Lambda_{c/4} = -20^\circ$, Küchemann and PANAIR agree well. However,

Fig. 5.13 shows that at combinations of low aspect ratio and high sweep angle, Küchemann fails to correctly predict the forward shift of the locus by up to 2.5% of the local chord.

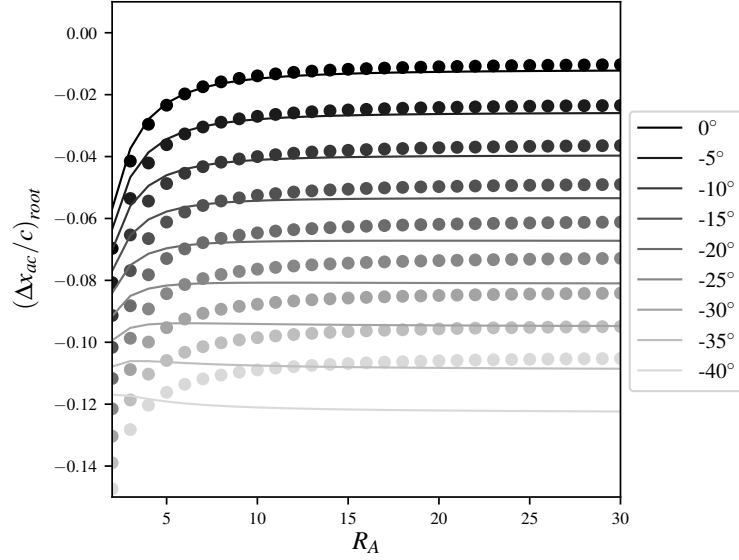


Fig. 5.13: $\Delta x_{ac}/c$ at center section for elliptic wings as a function of aspect ratio and sweep angle.

While the *RMS* from Fig. 5.12 is significantly higher than the results in Fig. 5.7, it is important to realize that the *RMS* is mainly driven by the behavior out towards the wing tips, where the small local chord magnifies $E_{x_{ac}/c}$ and hence drives the *RMS* up. Still, more care has to be taken when using Küchemann's analytic solution for the locus of section aerodynamic centers for forward swept wings.

CHAPTER 6

AERODYNAMIC PROPERTIES OF WINGS WITH CONSTANT SWEEP IN INVISCID FLOW

This chapter analyses a set of 1476 wings using a constant sweep profile, with varying sweep angles, aspect ratios, and taper ratios using the modern panel code FlightStream, according to the general relations for wings with sweep from Section 3.5. The planform design variables for the wings are shown in Table 6.1.

Table 6.1: Planform variables for wings with constant tip sweep.

	Minimum	Maximum	Interval
Λ_{tip} [°]	0	40	1
R_A	4	20	2
R_T	0.25	1.00	0.25

All wings in this analysis feature the symmetric NACA 0012 airfoil and feature no twist, and a root chord of one, fully defining the geometry. The inviscid simulations are all run in FlightStream using a grid featuring 160 panels in spanwise direction and 80 panels in chordwise direction, at an angle of attack of $\alpha = 5^\circ$. Tip sweep angle Λ_{tip} is defined as the angle of the imaginary line between the quarter-chord points of the root and tip airfoil section. In other words, for wings with constant sweep, Λ_{tip} is equivalent to the well-understood $\Lambda_{c/4}$, but the distinction is made to be consistent with the definition of geometry of wings with linear sweep, discussed in Section 3.1.

Section 3.5 defined general expressions to relate the aerodynamic properties of swept wings to wings of the same aspect ratio and taper ratio without sweep. These expressions can be seen as penalty factors with respect to the ideal, unswept planform with elliptical lift distribution. Sections 6.1, 6.2, and 6.3 use these relations to analyze the aerodynamic properties of the wings with constant sweep defined in Table 6.1 in terms of lift, induced

drag, and aerodynamic center position.

6.1 RESULTS FOR LIFT

Section 3.5 defined δ_L as the ratio of the lift curve slope at any tip sweep angle Λ_{tip} divided by the lift curve slope of a wing without sweep using the same aspect ratio and taper ratio. The correction in lift coefficient due to sweep δ_L for all the wings with constant sweep defined in Table 6.1 can be seen in Fig. 6.1. Each quadrant shows the results of a specific taper ratio. The interval between each line represents an aspect ratio change of two, with the most transparent line representing $R_A = 4$ and the most opaque line representing $R_A = 20$.

It is expected and shown that δ_L , and hence $C_{L,\alpha}$, decreases as the tip sweep Λ_{tip} increases. It can also be seen that for low aspect ratio wings, the penalty in lift curve slope due to sweep is less than that for high aspect ratio wings. Note that this does not mean that the absolute value of lift curve slope of a low aspect ratio swept wing is higher than that of one with a high aspect ratio. While reading specific values of Fig. 6.1 is hard, one could argue from the high concentration of lines, that above aspect ratio $R_A = 8$, the change in lift slope due to sweep δ_L is not very sensitive to aspect ratio. From the spread between aspect ratio $R_A = 4$ and $R_A = 20$, it also appears that as taper ratio increases, the results become less sensitive to aspect ratio.

6.2 RESULTS FOR INDUCED DRAG

Figure 6.2 shows the change in induced drag due to sweep κ_D as a function of the tip sweep angle with different plots for taper ratio and different lines for aspect ratio. The opacity of the lines increases with increasing aspect ratio, from the most transparent line with $R_A = 4$ to the most opaque line for $R_A = 20$. The step between each line represents an increase or decrease of $\Delta R_A = 2$ for the aspect ratio. Each quadrant mentions the taper ratio.

FlightStream correctly captures the downward trend in δ_D for increasing tip sweep, indicating a decrease in induced drag for an increase in sweep angle. We can see that as

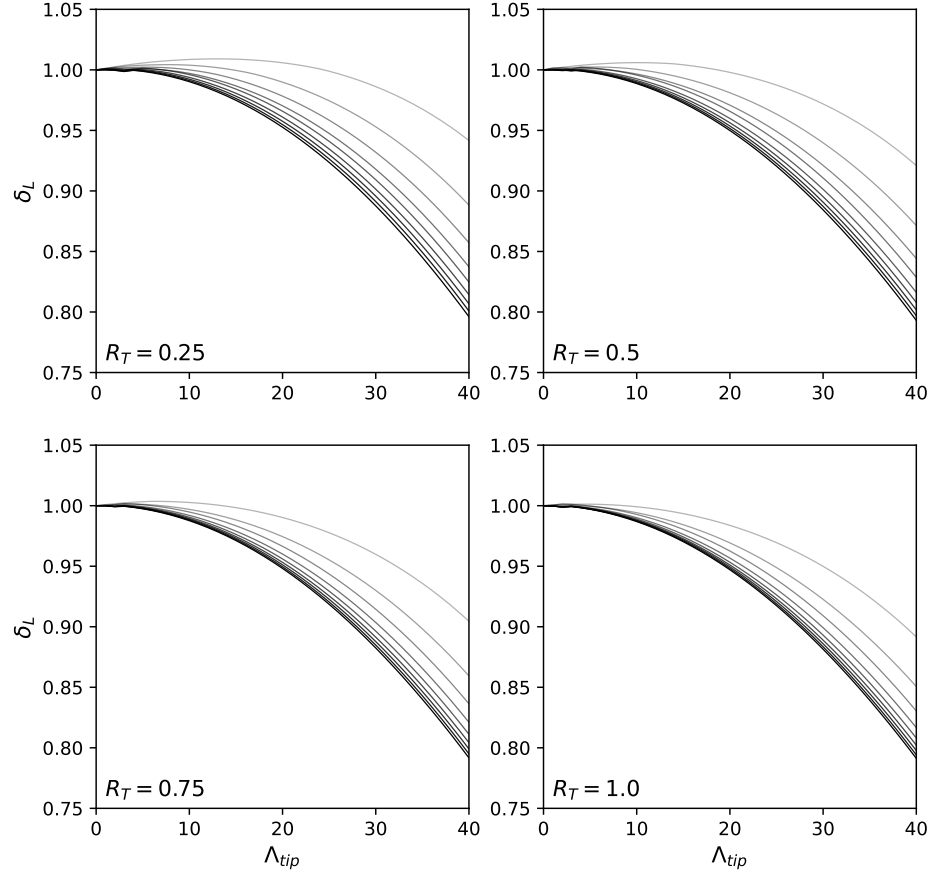


Fig. 6.1: Lift slope factor δ_L of wings with constant sweep as a function of tip sweep angle Λ_{tip} , aspect ratio, and taper ratio.

taper ratio R_T increases, κ_D trends towards higher values as well. The same is generally true for κ_D increasing with increasing aspect ratio R_A , although we can notice that this trend is reversed at higher tip sweep angles for the lowest taper ratio of $R_T = 0.25$. Note that this plot does not directly tell us anything about absolute values of induced drag, but that κ_D is in relation to a wing without sweep using the elliptic spanwise lift distribution. In other words, while we see that in general the drag penalty with respect to an unswept wing is larger for higher aspect ratios, we see that for low taper ratios with tip sweep angles higher than roughly 15° , low aspect ratios are actually penalized more than high aspect

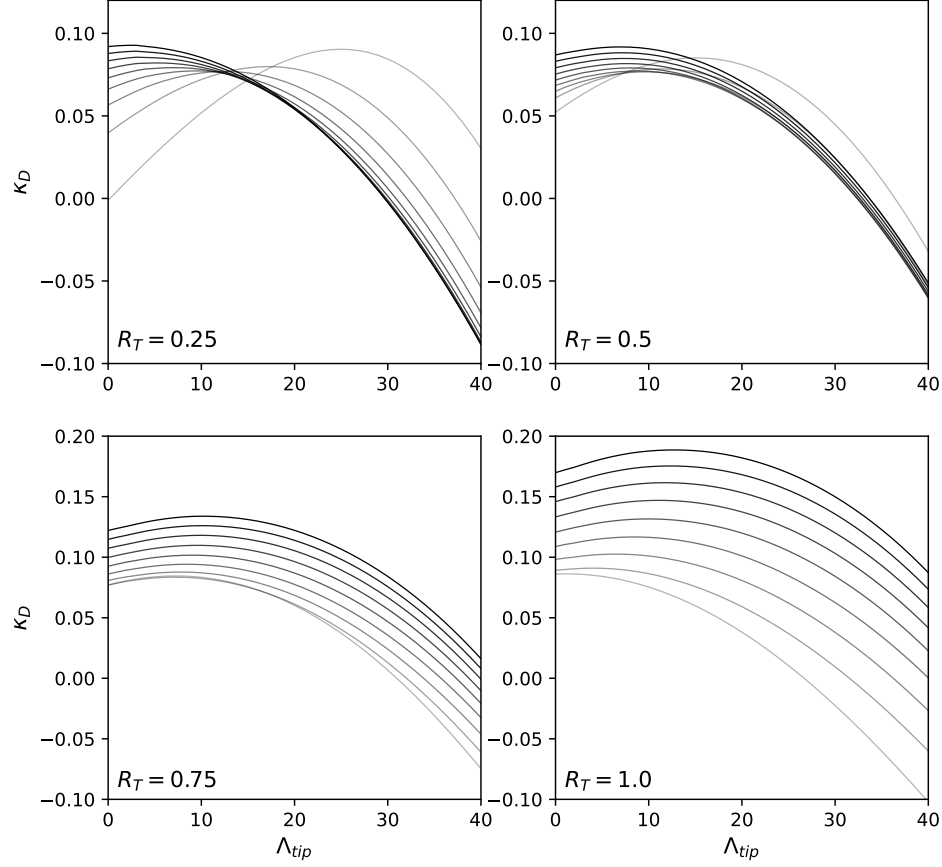


Fig. 6.2: Induced drag factor κ_D of wings with constant sweep as a function of tip sweep angle Λ_{tip} , aspect ratio, and taper ratio.

ratios. This could mean that in terms of aerodynamic efficiency, wings with low taper and aspect ratio are less suited for high sweep applications

It is interesting to note that while we traditionally have only used κ_D as an induced drag penalty for wings without sweep, we can see from Fig. 6.2 that expanding its definition to include swept wings means that κ_D can also be negative. This was also suggested by Van Dam [15]. Remember that κ_D is an induced drag penalty with respect to an unswept wing using the elliptic spanwise lift distribution. At first glance, a negative κ_D might suggest that the elliptic spanwise lift distribution is not the most aerodynamically efficient, but it

must be remembered that Fig. 6.2 analyses swept wings. As sweep increases, the induced drag coefficient C_{Di} decreases [53], so while a negative κ_D suggests lower drag of a swept wing when compared to an unswept wing using an elliptic lift distribution, it does not mean that the lift distribution of the wings in Fig 6.2 is in itself more efficient than an elliptic lift distribution.

6.3 RESULTS FOR AERODYNAMIC CENTER

Figure 6.3 shows change in aerodynamic center position due to sweep κ_{ac} as calculated using Eq. 3.14 for different taper ratios as a function of aspect ratio and tip sweep angle for all wings defined in Table 6.1. Again, the lowest aspect ratio $R_A = 4$ is represented by the most transparent line, the highest aspect ratio $R_A = 20$ is shown using the most opaque line, and the lines are $\Delta R_A = 2$ apart.

It can be seen in Fig. 6.3 that κ_{ac} increases for increasing sweep, meaning that for wings with rearward swept wings the aerodynamic center moves aft. This is in line with previous research on the locus of section aerodynamic centers [51]. As expected, κ_{ac} increases for increasing aspect ratio, since at constant root chord, an increased aspect ratio means longer span. The shift in aerodynamic center is seen to be fairly insensitive to taper ratio.

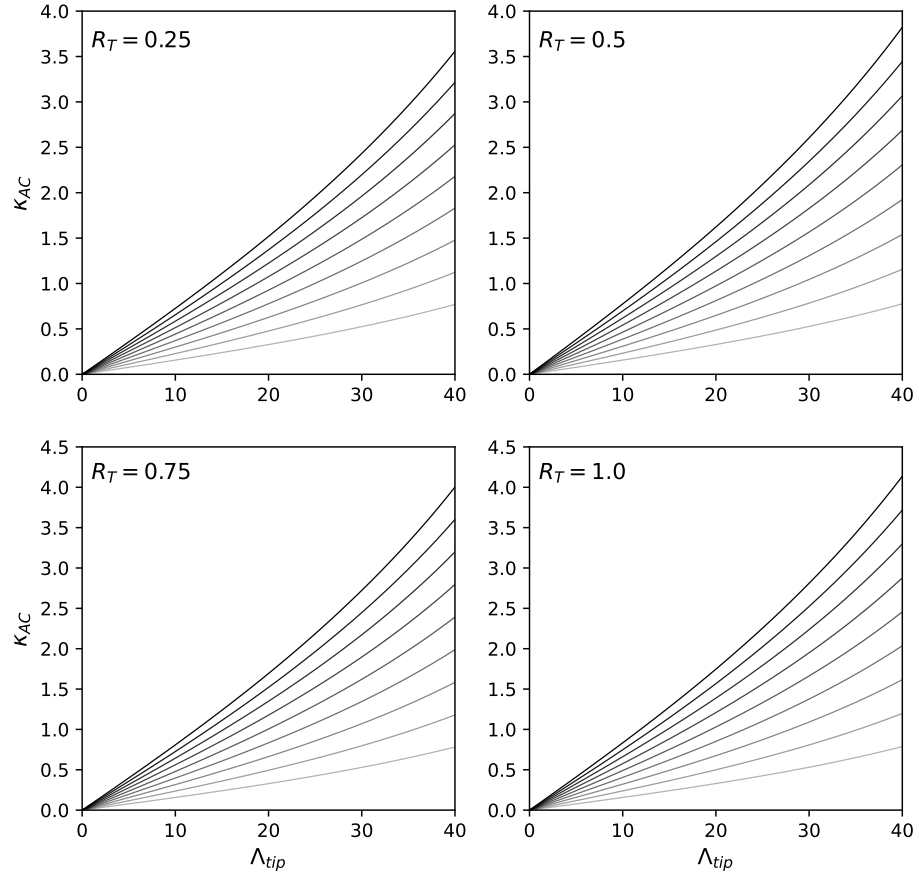


Fig. 6.3: Aerodynamic center shift factor κ_{ac} of wings with constant sweep as a function of tip sweep angle Λ_{tip} , aspect ratio, and taper ratio.

CHAPTER 7

AERODYNAMIC PROPERTIES OF WINGS WITH LINEAR SWEEP IN INVISCID FLOW

This chapter discusses a set of 1476 wings using a linear sweep profile, with varying tip sweep angles, aspect ratios, and taper ratios. All wings were analyzed using the inviscid panel code FlightStream, discussed in Section 3.2.3. The planform variables governing the set of wings with a linear sweep profile is described in Table 7.1. Section 3.1 discusses the geometry of a linearly swept wings.

Table 7.1: Planform variables for wings with linear sweep.

	Minimum	Maximum	Interval
Λ_{tip} [°]	0	40	1
R_A	4	20	2
R_T	0.25	1.00	0.25

Just like with the constant sweep analysis, all linearly swept wings feature the symmetric NACA 0012 airfoil, no twist, and a root chord of one. The inviscid simulations are all run in FlightStream using a grid with 160 spanwise panels and 80 chordwise panels, at an angle of attack of $\alpha = 5^\circ$.

Sections 7.1, 7.2, and 7.3 use the general relations from Section 3.5 to discuss the aerodynamic properties of wings with a linear sweep profile.

7.1 RESULTS FOR LIFT

For wings with linear sweep, the correction in lift coefficient due to sweep δ_L is defined as the ratio of the lift curve slope at any tip sweep angle Λ_{tip} divided by the lift curve slope of a wing without sweep using the same aspect ratio and taper ratio. Figure 7.1 shows δ_L for all crescent wings defined in Table 7.1. Each quadrant shows the results of a specific taper

ratio. The interval between each line represents an aspect ratio change of two, with the most transparent line representing $R_A = 4$ and the most opaque line representing $R_A = 20$.

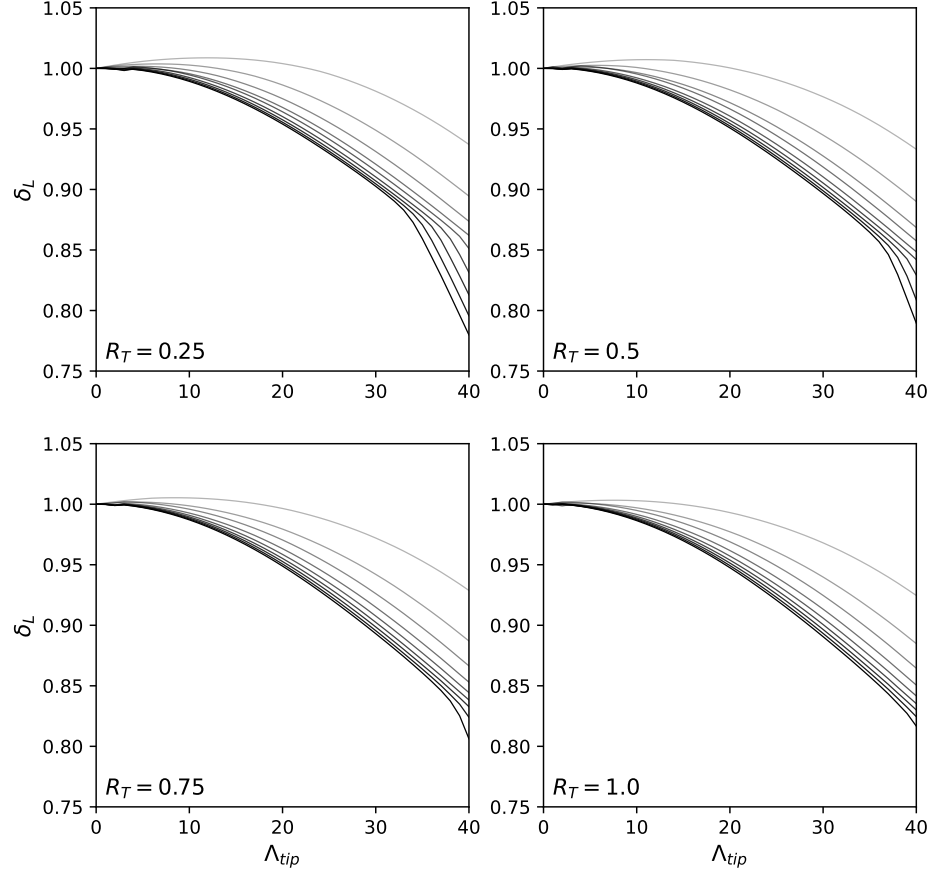


Fig. 7.1: Lift slope factor δ_L of wings with linear sweep as a function of tip sweep angle Λ_{tip} , aspect ratio, and taper ratio.

When comparing Fig. 7.1 to Fig. 6.1, it seems that, while they following the same downward trends, the values for δ_L are slightly higher for the crescent wings, suggesting a slightly lower penalty in lift-curve slope due to sweep. This is likely due to the fact that because of its shape, a crescent wing is effectively less swept across the span than a wing with constant sweep, with only the tip section being in the same location as that of a wing

with constant sweep. The same overall observations about dependency on taper and aspect ratio as those made for the wings with constant sweep apply.

A sharp increase in slope can be seen for some wings at high tip sweep angles. This effect is more noticeable for combinations of high aspect ratio R_A with low taper ratio R_T . The exact reason of this is unknown, but a couple of suggestions are proposed. It could be a physical phenomenon due to the fine outboard wing section having a more significant effect at high sweep angles. This would explain why the effect is more noticeable at combinations of high aspect ratio and low taper ratio, where the wing tip is more slender than at combinations of low aspect ratio and high taper ratio. It could also be a numerical phenomenon due to the skewness of the fine panels used for modelling the wing tips.

7.2 RESULTS FOR INDUCED DRAG

The results for the penalty in induced drag due to sweep for linearly swept wings can be seen in Fig. 7.2. Again, each quadrant shows a different taper ratio, and the different lines show different aspect ratios, with the most transparent line representing $R_A = 4$, the most opaque line representing $R_A = 20$, and each consecutive line denoting a step change of two.

When comparing Fig. 7.2 to Fig. 6.2, a couple of things are immediately apparent. At $R_T = 0.25$, the κ_D values for crescent wings are never negative, whereas this was achieved by high aspect ratios on wings with constant sweep and the same taper ratio. However, for all remaining taper ratios, linearly swept wings appear to achieve lower κ_D values across the board, suggesting that crescent wings might be more aerodynamically efficient than wings with constant sweep. A sharp increase can be seen at high tip sweep angles, especially for wings with combinations of low taper ratio and high aspect ratio. This is likely to be caused by the same mechanism that causes the increase in slope of the results for δ_L in Fig. 7.1.

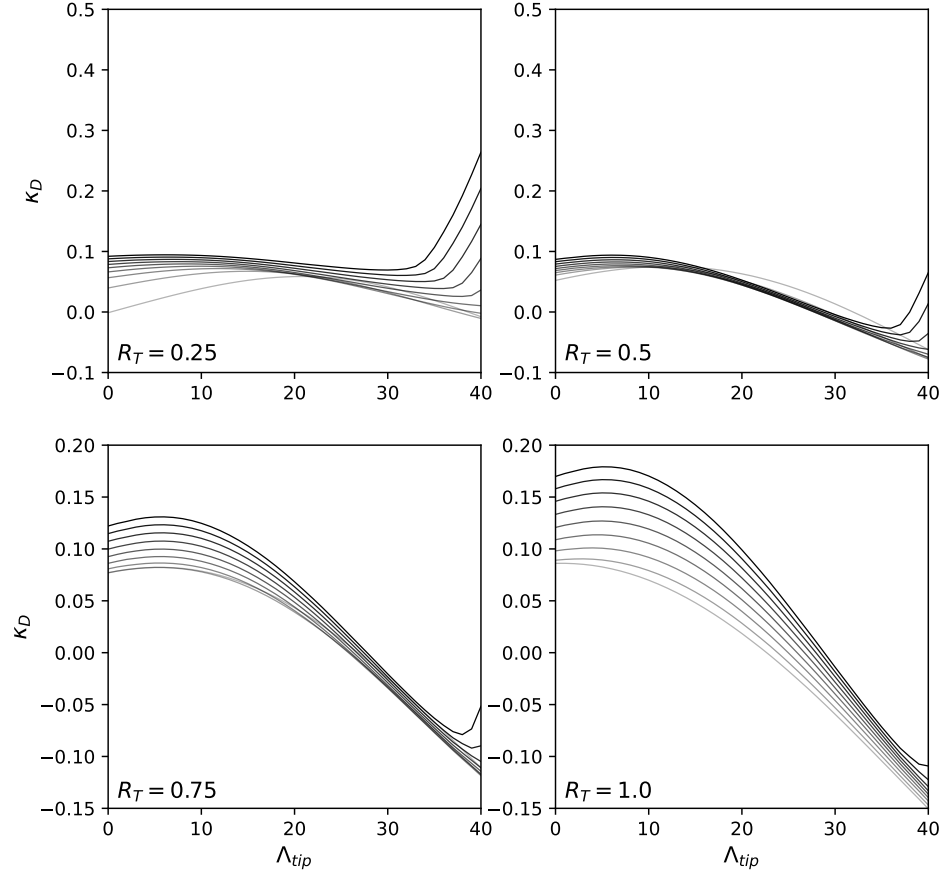


Fig. 7.2: Induced drag factor κ_D of wings with linear sweep as a function of tip sweep angle Λ_{tip} , aspect ratio, and taper ratio.

7.3 RESULTS FOR AERODYNAMIC CENTER

The results for shift in aerodynamic center κ_{ac} for linearly swept wings are shown in Fig. 7.3. They show no surprises when compared to the results for conventionally swept wings in Fig. 6.3. One thing to note is that the overall range of κ_{ac} values is lower for the crescent wings than the wings with constant sweep, which is due to the fact of the crescent wings being effectively less swept across the majority of the span. While for a wing with constant sweep, the quarter-chord line lies on top of the imaginary line connecting the quarter-chord points of wing root and wing tip, for a crescent wing, all the surface area

lies in front of it, decreasing the shift in aerodynamic center aft with sweep. Note that the curling of the lines at higher tip sweep angles is again likely linked to the mechanism causing the effects visible in Figs. 7.1 and 7.2.

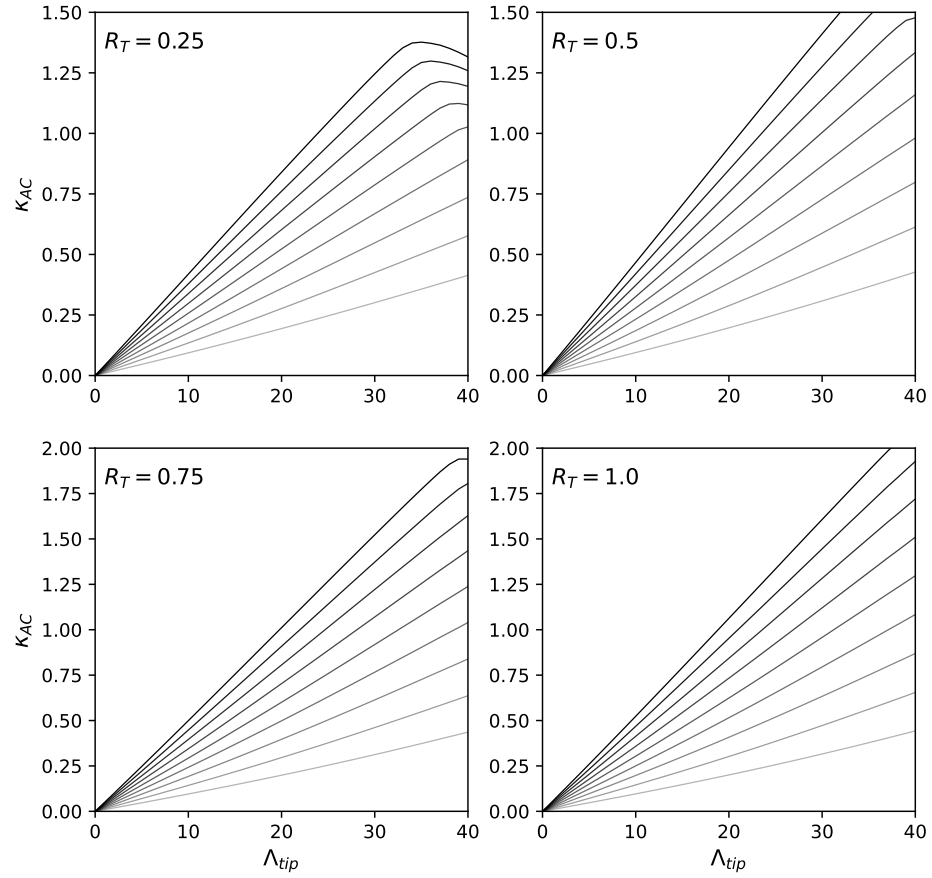


Fig. 7.3: Aerodynamic center shift factor κ_{ac} of wings with linear sweep as a function of tip sweep angle Λ_{tip} , aspect ratio, and taper ratio.

CHAPTER 8

COMPARISON OF INVISCID AERODYNAMICS OF WINGS WITH CONSTANT AND LINEAR SWEEP

This chapter makes a comparison between wings with constant sweep and those with a linear sweep profile, discussed in Chapters 6 and 7 respectively. Section 8.1 discusses why both wing types can't be compared to each other at constant Λ_{tip} , and offers a different way of comparing the two. Sections 8.2 and 8.3 combine the results from all wings described in Tables 6.1 and 7.1 to draw comparisons between the two sweep types, to hopefully offer some insight in whether one is more aerodynamically efficient than the other and why we don't see constant sweep in nature.

8.1 COMPARISON CRITERIA

In order to make a comparison, it has to be established what constitutes a fair or useful comparison and what the main performance metric to be measured is. It is good to remember that in subsonic applications, wing sweep is applied to provide stability to the wing or aircraft by shifting the aerodynamic center aft in relation to the center of gravity. When comparing wings with a constant and linear sweep profile, a crescent wing with 20 degrees of tip sweep is effectively less swept than a conventionally swept wing with 20 degrees of constant spanwise sweep, because the surface area of the crescent wing lies in front of that of a wing with constant sweep, as seen in Fig. 8.1, showing wings with $R_A = 8$, $R_T = 0.25$ and $\Lambda_{tip} = 20^\circ$ featuring a linear or a constant sweep profile. The aerodynamic center positions are shown using a circle.

The same conclusion can be drawn by looking at Fig. 8.2, where κ_{ac} is plotted versus the tip sweep angle Λ_{tip} for a linearly and conventionally swept wings with aspect ratio $R_A = 8$ and taper ratio $R_T = 0.25$. It can be seen that for equal tip sweep angle Λ_{tip} , κ_{ac} is higher for the wing with constant sweep, denoting a farther shift aft of the aerodynamic

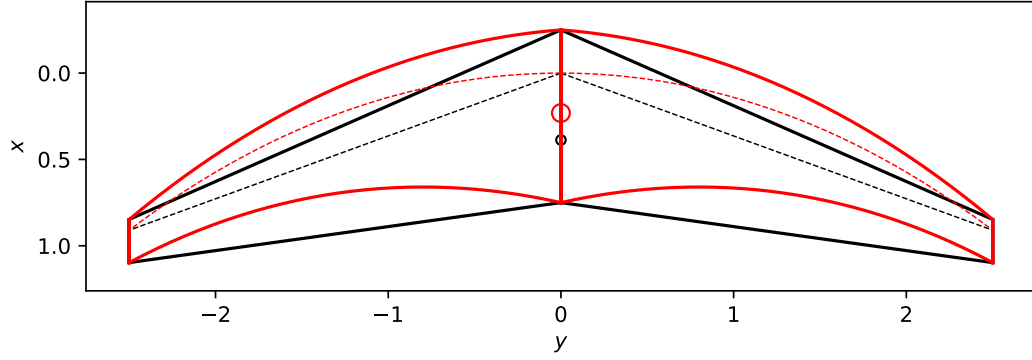


Fig. 8.1: Wings with $R_A = 8$, $R_T = 0.25$ and $\Lambda_{tip} = 20^\circ$ featuring constant and linear sweep profiles.

center position.

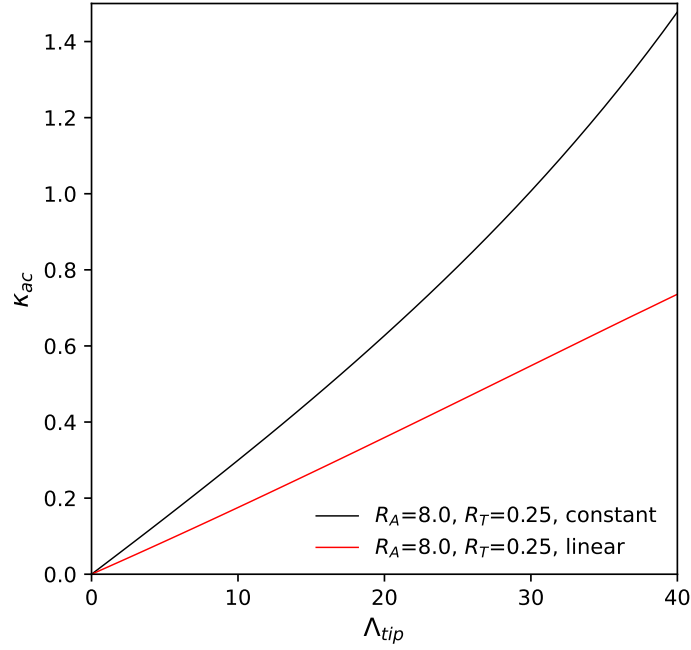


Fig. 8.2: Aerodynamic center shift κ_{ac} as a function of Λ_{tip} for wings with $R_A = 8$ and $R_T = 0.25$ featuring constant and linear sweep profiles.

Because of the significant difference in aerodynamic center position between the wing with constant sweep and the wing with linear sweep, they are not likely to be used in

the same application for the same flight condition and comparing two wings of equal tip sweep angle does not seem useful. A wing with constant sweep and a crescent wing with the same aspect ratio, taper ratio, and root chord have the same wing area regardless of their sweep profile. It is assumed that they make use of the same airfoil section and have no wing twist. Therefore, at a certain tip sweep angle, their lift coefficients C_L will be comparable. If a designer wants to consider these two designs at similar flight conditions in similar application, they should offer a similar level of longitudinal stability. An important parameter in flight performance is the static margin, which is a measure for how much longitudinal stability an aircraft or wing has. It is defined as

$$\sigma = \frac{x_{ac} - x_{cg}}{\bar{c}} \quad (8.1)$$

where x_{cg}/c is the position of the center of gravity, and x_{ac}/c is the aerodynamic center position, which can be calculated using Eq. (3.10). Since this research is specifically looking at the aerodynamics of swept wings and does not attempt to make an accurate tool for center of gravity position prediction, it is assumed that aerodynamic center position offers a suitable replacement for the static margin. Since one wing with constant sweep and one wing with crescent sweep in a comparison will be of equal aspect ratio, taper ratio, root chord, and hence wing area, it is assumed that structurally they will be similar. As the aerodynamic center moves aft, the center of gravity will move aft a certain amount without altering the relation between them. Therefore, it is assumed that a comparison between two wings is fair if they produce the same shift in aerodynamic center position. The aerodynamic efficiency of both wings is assessed by looking at the induced drag coefficient factor κ_D .

8.2 RESULTS FOR WINGS WITH ASPECT RATIO $R_A = 8$ AND TAPER RATIO $R_T = 0.25$

Before looking at the complete set of results, an in-depth look is taken at an example set of wings with a specific aspect and taper ratio combination. Figure 8.3 shows κ_D as a function of κ_{ac} for wings with $R_A = 8$ and $R_T = 0.25$ using a constant sweep profile

and a linear sweep profile. Because comparing the two different types of wings at the same tip sweep angle Λ_{tip} is not useful as per the discussion in Section 8.1, κ_D is plotted versus κ_{ac} , the shift in aerodynamic center. The dashed line depicts the wing with constant sweep, while the solid line depicts the crescent wing. Note that since both wing types were analyzed to the same maximum tip sweep angle $\Lambda_{tip} = 40^\circ$, the wing with constant sweep is capable of higher values for κ_{ac} than the crescent wing.

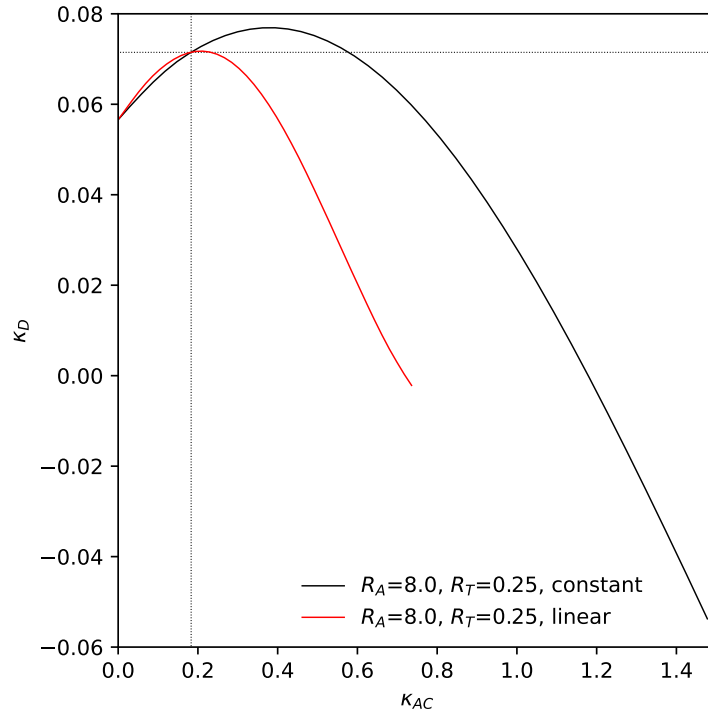


Fig. 8.3: Induced drag factor κ_D as a function of aerodynamic center shift κ_{ac} for wings with $R_A = 8$ and $R_T = 0.25$ featuring constant and linear sweep profiles.

It can be seen from Fig. 8.3 that the lines for constant and linear sweep cross at some point, marked by the horizontal and vertical dotted lines. To the left of this intersection, the dashed line lies below the solid line, suggesting that up until a certain required shift in aerodynamic center position, the wing with constant sweep could be more aerodynamically efficient than the wing with linear sweep, although after this point the crescent wing shows potential benefits. We can quantify this potential benefit by simply taking the difference

between the two as

$$\Delta\kappa_D = \kappa_{D,lin} - \kappa_{D,cst} \quad (8.2)$$

where the subscripts *lin* and *cst* denote linear and constant sweep respectively. Figure 8.4 plots $\Delta\kappa_D$ versus κ_{ac} over the range of κ_{ac} values of the crescent wing, since this has the more limited aerodynamic shift range.

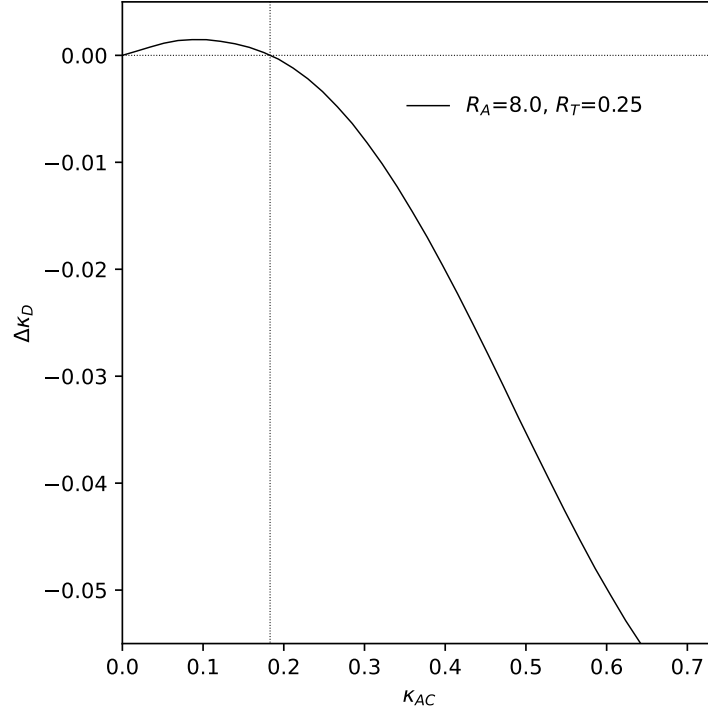


Fig. 8.4: Change in induced drag factor $\Delta\kappa_D$ between constant and linear sweep profiles as a function of aerodynamic center shift κ_{ac} for wings with $R_A = 8$ and $R_T = 0.25$.

We can find the intersection point where the lines for the wings with constant and linear sweep cross in Fig. 8.3 at $k_{ac} = 0.19$, $\kappa_D = 0.072$. We can also find this κ_{ac} value by marking where the curve crosses $\Delta\kappa_D = 0$, marked in Fig. 8.4. From Fig. 8.2 we can see what tip sweep angle Λ_{tip} this equates to for wings with a constant and linear sweep profile. For $k_{ac} = 0.19$, the tip sweep of a wing with constant sweep is $\Lambda_{tip,cst} = 6.19^\circ$ and that of a wing with linear sweep is $\Lambda_{tip,lin} = 10.42^\circ$. Figure 8.5 shows the two corresponding wings

plotted on top of each other. The circles indicate their global aerodynamic center position.

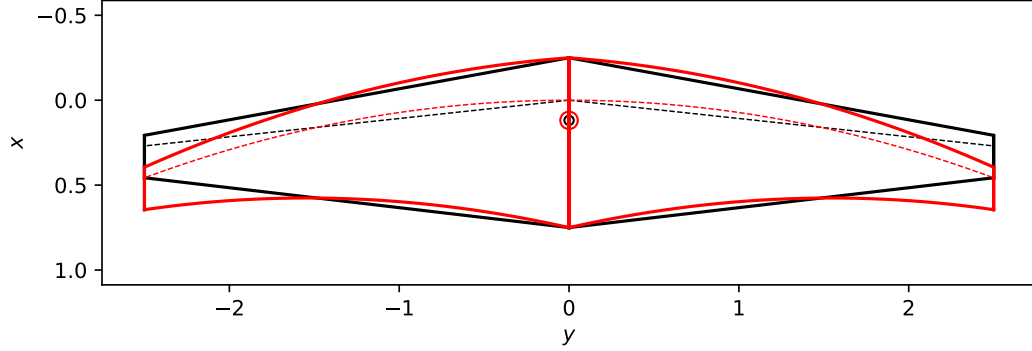


Fig. 8.5: Wings with $R_A = 8$, $R_T = 0.25$ featuring constant and linear sweep profiles with equal κ_{ac} and equal κ_D .

Since κ_D is nearly independent of lift coefficient C_L and it is equal between the constant and crescent wings at the intersection in Fig. 8.3, it is expected that their induced drag polars will be identical as well. These can easily be constructed by analyzing the wing geometries of Fig. 8.5 over a range of angle of attack values from $\alpha = -5^\circ$ to $\alpha = 5^\circ$. Figure 8.6 shows the drag polar as lift coefficient C_L versus induced drag coefficient C_{D_i} .

Note that because this is an inviscid study, the results in Fig. 8.6 only include induced drag. Also included in the figure are the results for $\kappa_D = 0$, which from Eq. (2.10) follows is the induced drag coefficient for an unswept wing using the elliptic lift distribution. Remember that κ_D is a penalty with respect to this drag value. The crosses, denoted as “analytic” in the legend, use Eq. (2.10) with $\kappa_D = 0.072$, found from the intersection Fig. 8.3. The fact that these lie on the computational result curves prove that κ_D is very nearly independent of C_L . This can also be seen in Fig. 8.7, where κ_D changes only slightly over the range of C_L values, apart from a slight asymmetry across the zero-lift point, which follows from the way matrices are solved in FlightStream. Note that at $C_L = 0$ there is no drag in an inviscid simulation, and hence no κ_D value is computed.

Since the induced drag polars and induced drag factor κ_D are identical between the wing with constant and the wing with linear sweep and their aerodynamic center shift factor

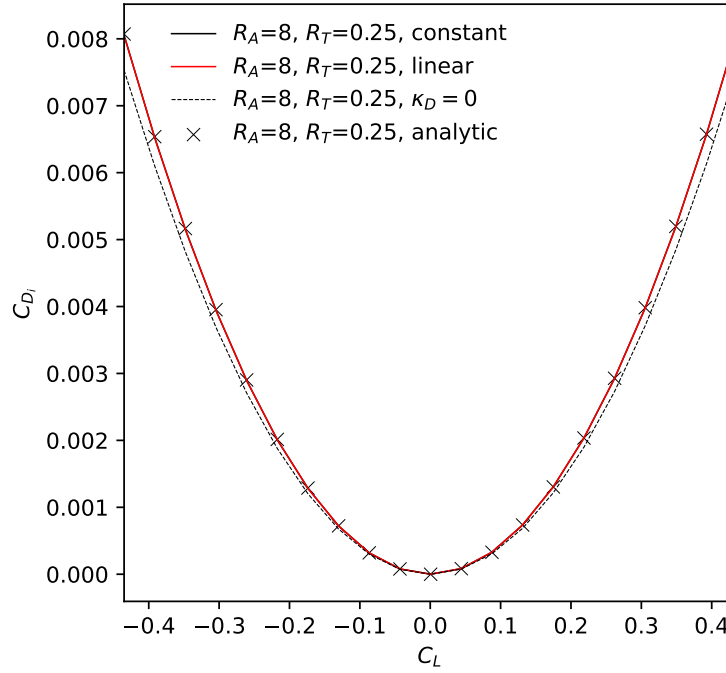


Fig. 8.6: Drag polars for wings with $R_A = 8$, $R_T = 0.25$ using constant and crescent sweep at the intersection in Fig. 8.3.

κ_{ac} is equal as well, it could be assumed that their lift properties are also the same. Figure 8.8 shows the spanwise distribution of lift coefficient multiplied by local chord, $\tilde{C}_L c$, for both wing types. It also includes the elliptic spanwise lift distribution from an elliptic planform with no sweep and $R_A = 8$. All wings are analyzed at a lift coefficient of $C_L = 0.3$.

Figure 8.8 shows that both distributions resemble an elliptical spanwise lift distribution. While both integrate to a global lift coefficient of $C_L = 0.3$, the spanwise lift distributions are not identical. The wing with linear sweep carries more lift outboard, which is interesting considering it experiences higher local sweep angles near the wing tip than the wing with constant sweep does.

Figure 8.6 is specifically for the point of intersection in Fig. 8.3 where the constant and crescent wings have the same κ_{ac} and κ_D . If instead we look at $\kappa_{ac} = 0.50$ in Fig. 8.3, we find that $\kappa_D = 0.075$ for the wing with constant sweep and $\kappa_D = 0.040$ for the crescent wing, resulting in a $\Delta\kappa_D = -0.035$ between both wing types. From Fig. 8.2 we see that $\kappa_{ac} = 0.50$ corresponds to $\Lambda_{tip, cst} = 16.26^\circ$ and $\Lambda_{tip, lin} = 27.48^\circ$. Figures 8.9 and

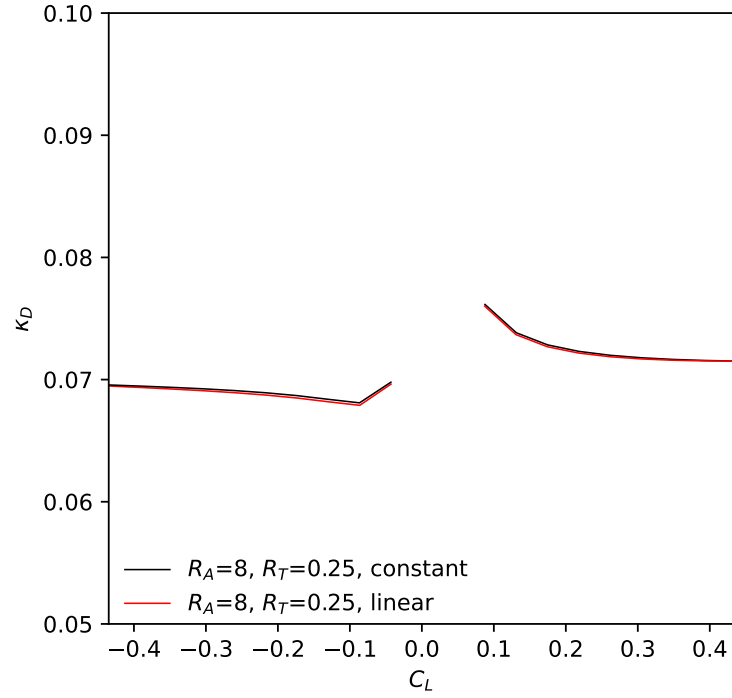


Fig. 8.7: Induced drag factor κ_D as a function of lift coefficient C_L for wings with constant and crescent sweep at the intersection in Fig. 8.3

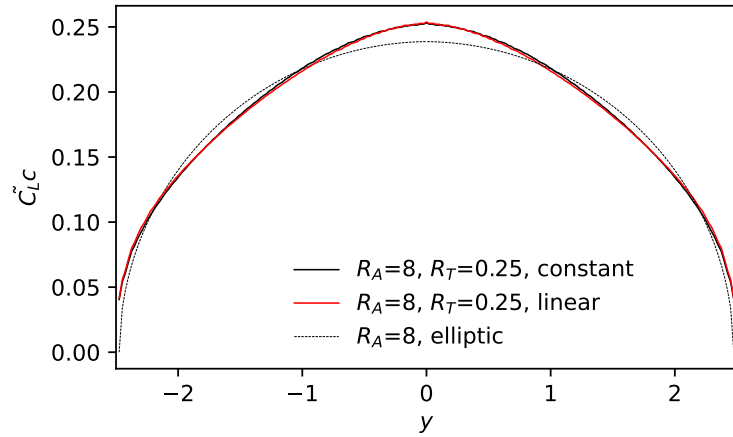


Fig. 8.8: Spanwise lift distribution for wings with constant and crescent sweep at the intersection in Fig. 8.3, evaluated at $C_L = 0.3$

8.10 show the corresponding wings and induced drag polars respectively. The circles in Fig. 8.9 indicate the wings' global aerodynamic center position.

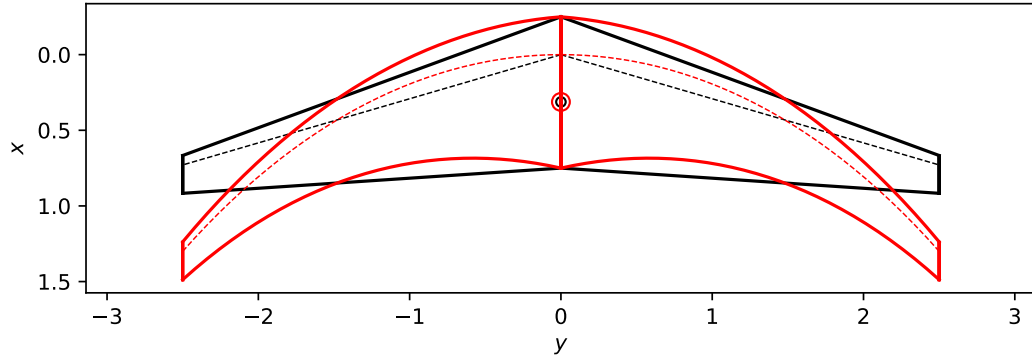


Fig. 8.9: Wings with $R_A = 8$, $R_T = 0.25$ featuring constant and linear sweep profiles with $\kappa_{ac} = 0.50$.

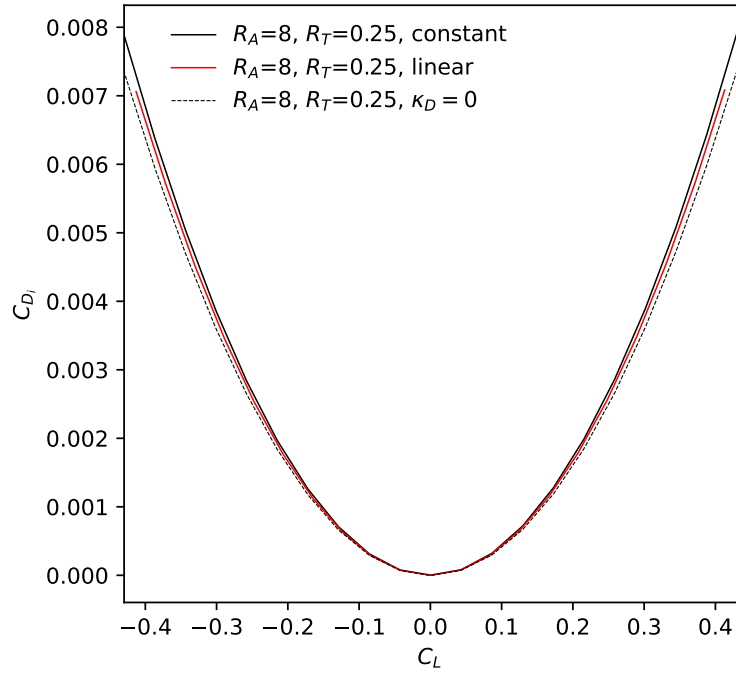


Fig. 8.10: Drag polars for wings with $R_A = 8$, $R_T = 0.25$ using constant and crescent sweep with $\kappa_{ac} = 0.50$.

There is a 89% difference between the $\kappa_D = 0.075$ for the wing with constant sweep and $\kappa_D = 0.040$ for the wing with linear sweep. However, the difference in Fig. 8.10 does not look as substantial. This is because κ_D is the penalty of drag with respect to a wing with the same aspect ratio using an elliptic lift distribution. In other words, the wing with constant sweep has a drag penalty that is 89% higher than the wing with linear sweep

compared to the unswept wing with the same aspect ratio and an elliptic lift distribution, which results in just a few percent more total induced drag.

Going back to Fig. 8.3 and looking at $\kappa_D = 0.040$, we find $\kappa_{ac} = 0.91$ for the conventionally swept wing and $\kappa_{ac} = 0.50$ for the wing with linear sweep. From Fig. 8.2 we see that this corresponds to $\Lambda_{tip,cst} = 27.67^\circ$ and $\Lambda_{tip,lin} = 27.36^\circ$. Figures 8.11 and 8.12 show the corresponding wings and induced drag polars respectively. The circles in Fig. 8.11 indicate the wings' global aerodynamic center position.

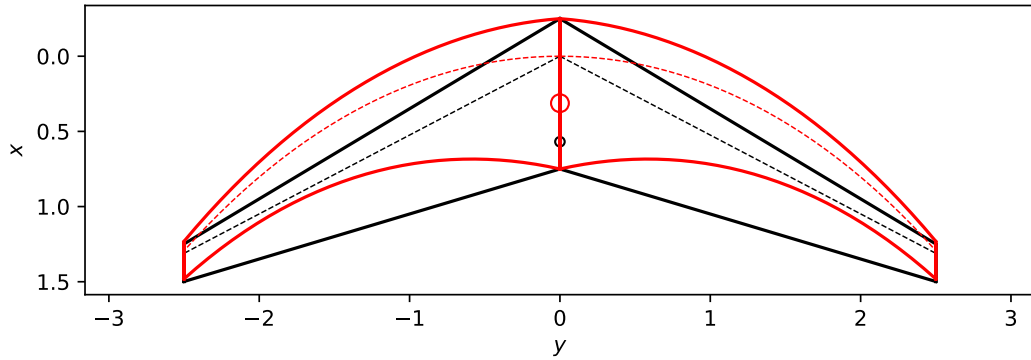


Fig. 8.11: Wings with $R_A = 8$, $R_T = 0.25$ featuring constant and linear sweep profiles with $\kappa_D = 0.040$

It is obvious that the induced drag polars in Fig. 8.12 lie on top of each other, as the κ_D value was specified to be $\kappa_D = 0.040$ for both. It is also clear that the induced drag values are lower in Fig. 8.12 than in Fig. 8.6, where $\kappa_D = 0.072$. Figure 8.12 shows two types of wings with the exact same induced drag, but where the one with constant sweep provides significantly more stability than the crescent wing, thanks to the higher κ_{ac} .

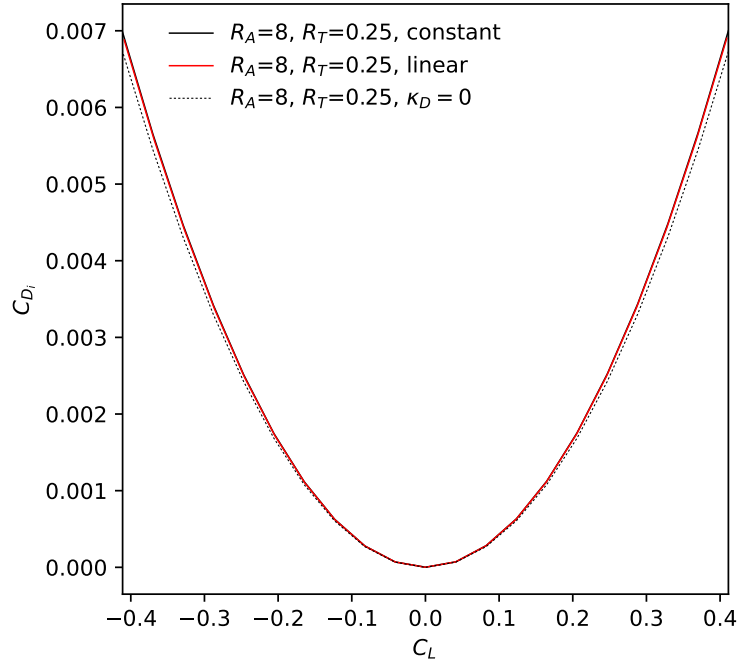


Fig. 8.12: Drag polars for wings with $R_A = 8$, $R_T = 0.25$ using constant and crescent sweep with $\kappa_D = 0.040$.

8.3 RESULTS FOR WINGS OF VARYING ASPECT AND TAPER RATIO

Having looked at the comparison of a wing with constant sweep and one with linear sweep for one particular aspect and taper ratio combination, $R_A = 8, R_T = 0.25$, we now look at the complete set of wings that were analyzed in Chapters 6 and 7.

Figure 8.13 shows κ_{ac} versus κ_D for constant and crescent wings with aspect ratio $R_A = 8$ and across all taper ratios analyzed, with each quadrant showing a different taper ratio. The dashed lines depict the wings with constant sweep, while the solid lines depict the wings with linear sweep.

The point where the lines for wings with constant and linear sweep cross appears to creep towards the left, or lower κ_{ac} , for increasing taper ratio, suggesting that crescent wings could show a benefit at lower required shifts in aerodynamic center, or equivalently lower tip sweep angles, for wings with high taper ratios than for wings with low aspect ratios..

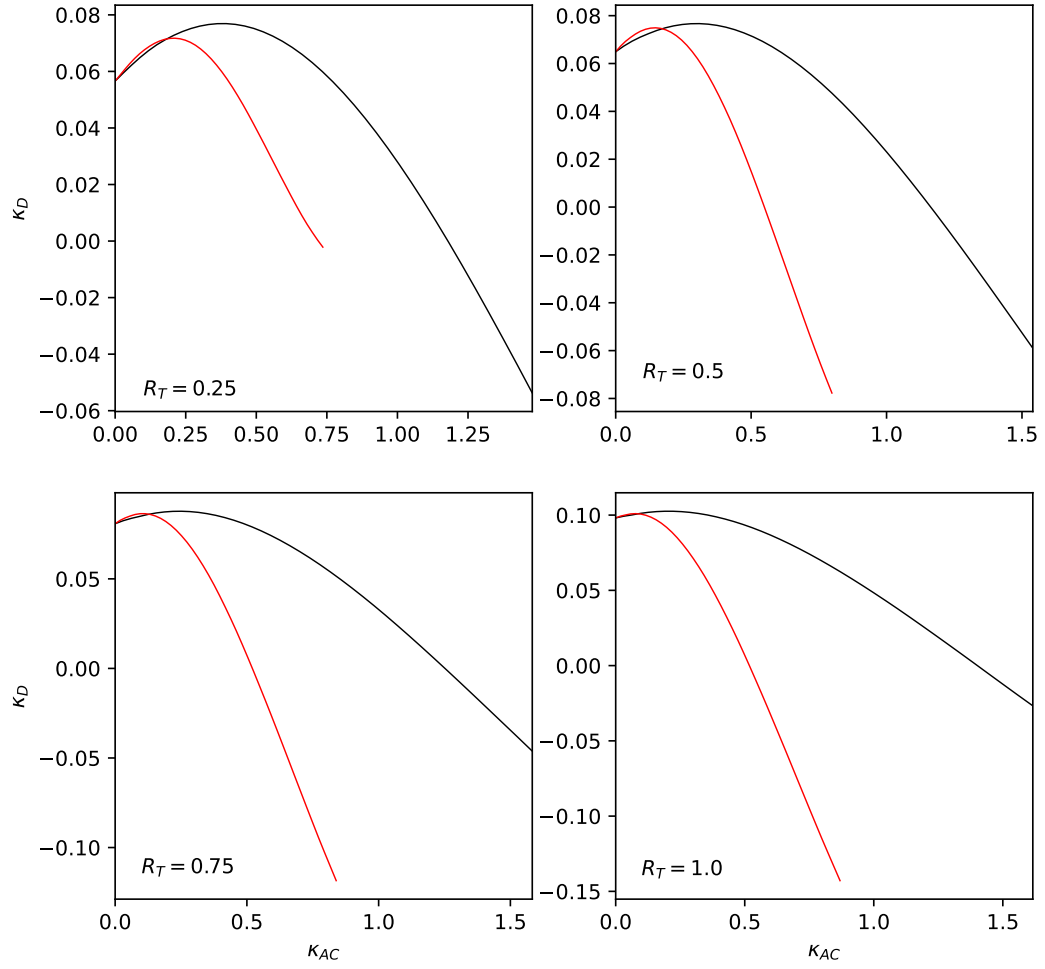


Fig. 8.13: Induced drag factor κ_D as a function of aerodynamic shift factor κ_{ac} and taper ratio R_T , for wings with aspect ratio $R_A = 8$ featuring constant linear sweep profiles.

Figure 8.14 shows κ_D for wings of taper ratio $R_T = 0.25$ using constant and linear sweep. The different quadrants show different aspect ratios. Again, the dashed lines depict the wings with constant sweep, while the solid lines depict the wings with constant sweep.

We see that as the aspect ratio increases, so does the range on the horizontal axis depicting κ_{ac} . This is because since the root chord is kept constant and equal to one for all wings, a higher aspect ratio results in a higher span. The higher span means a higher shift of the aerodynamic center or higher κ_{ac} for swept wings.

It appears from Fig. 8.14 that the results for κ_D for wings with constant and linear sweep lie closer to one another as the aspect ratio increases. This would suggest that with

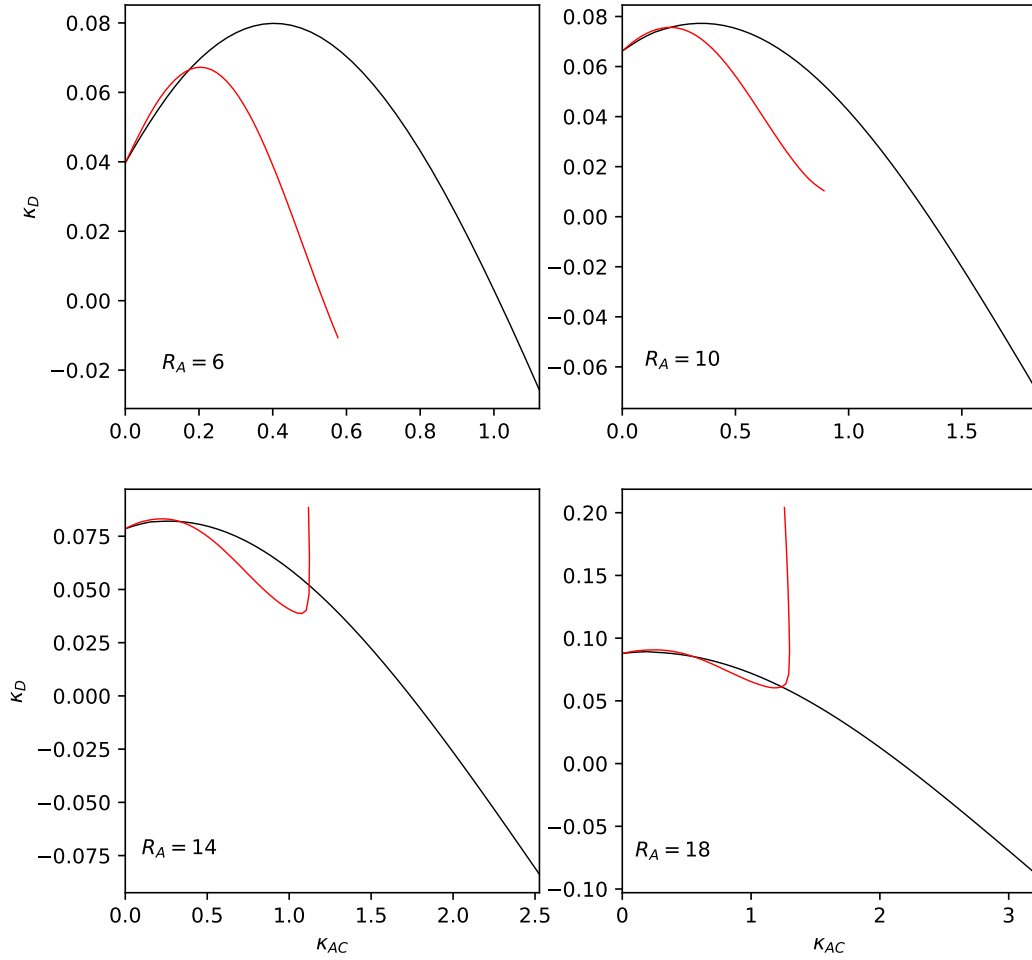


Fig. 8.14: Induced drag factor κ_D as a function of aerodynamic shift factor κ_{ac} and aspect ratio R_A , for wings with taper ratio $R_T = 0.25$ featuring constant linear sweep profiles.

taper ratio $R_T = 0.25$, at high aspect ratios, there is less of a difference in aerodynamic efficiency between both types of wing sweep profiles than at lower taper ratios. A possible explanation is that at higher aspect ratios, leading to higher spans, the effect of the physical curvature of the quarter-chord sweep line from a planform perspective is less noticeable.

Figure 8.15 shows $\Delta\kappa_D$ as calculated using Eq. (8.2) for all wings. Each quadrant depicts a different taper ratio, while the different lines indicate different aspect ratios. The most transparent lines is used for wings with aspect ratio $R_A = 4$, while the most opaque line shows aspect ratio $R_A = 20$. Each line in between depicts a step change of 2 in aspect ratio.

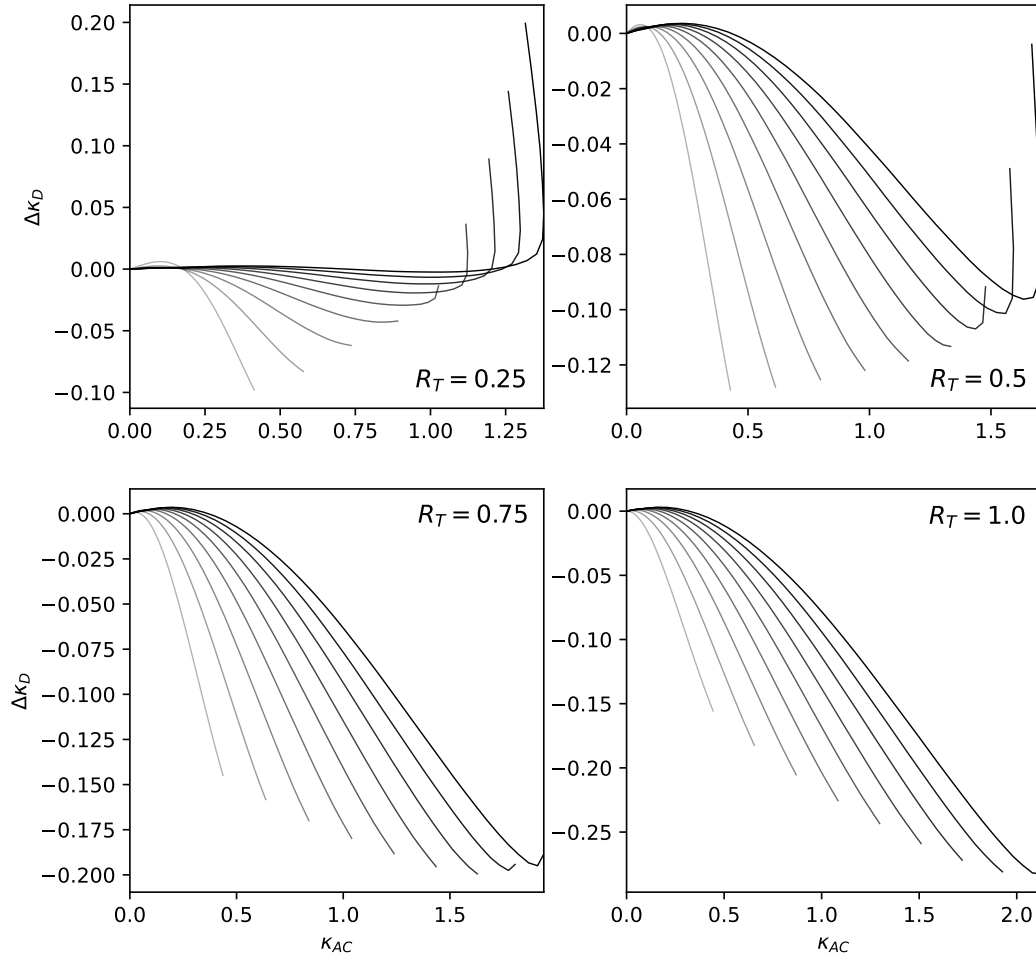


Fig. 8.15: Change in induced drag factor $\Delta\kappa_D$ between constant and linear sweep profiles as a function of aerodynamic center shift factor κ_{ac} , aspect ratio R_A , and taper ratio R_T .

We see that $\Delta\kappa_D$ is generally closer to zero for higher aspect ratios for all taper ratios, but it is nowhere as pronounced as with taper ratio $R_T = 0.25$, which we saw in Fig. 8.14 and now again in the top-left quadrant of Fig. 8.15. It can also be seen that $\Delta\kappa_D$ reaches lower, or more negative, values for increasing taper ratio, and that the effect of aspect ratio becomes less apparent at high taper ratio, which can be noticed due to the lines being more concentrated.

From Fig. 8.15 we can mark the κ_{ac} values where $\Delta\kappa_D = 0$, to mark at which point the linear sweep profile is potentially more aerodynamically efficient than the constant sweep profile. This is similar to what was done in in Fig. 8.4, but applied to all 1476 wings in our

data set. Figure 8.16 shows how this κ_{ac} value changes as a function of aspect ratio and taper ratio.

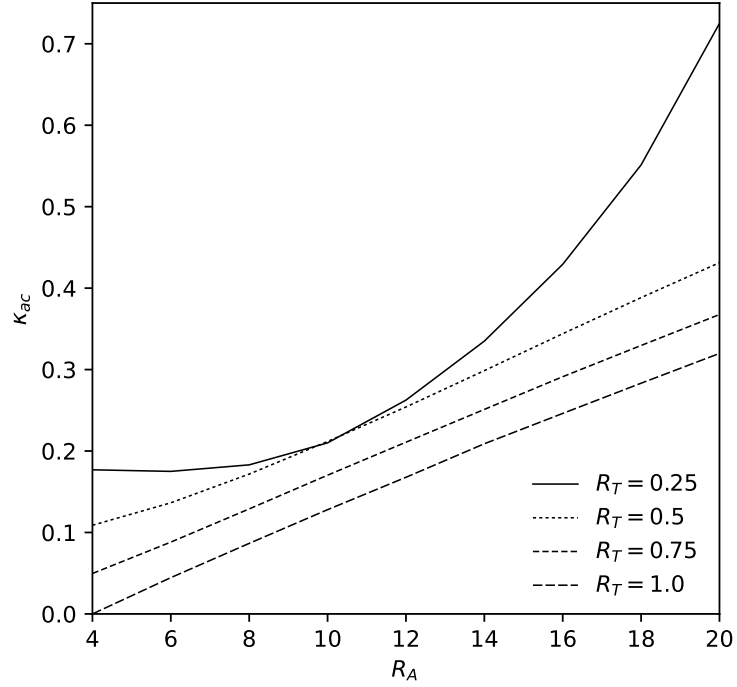


Fig. 8.16: Cross-over point between constant and linear sweep profiles in terms of aerodynamic center shift factor κ_{ac} as a function of aspect ratio R_A and taper ratio R_T .

From Fig. 8.16 we see that as taper ratio increases, a crescent wing becomes potentially more aerodynamically efficient than a wing with constant sweep at lower κ_{ac} values. Using Fig. 6.3, κ_{ac} can be turned in an equivalent constant sweep angle, above which a linear sweep profile becomes more efficient. Doing this to Fig. 8.16 gives us Fig. 8.17.

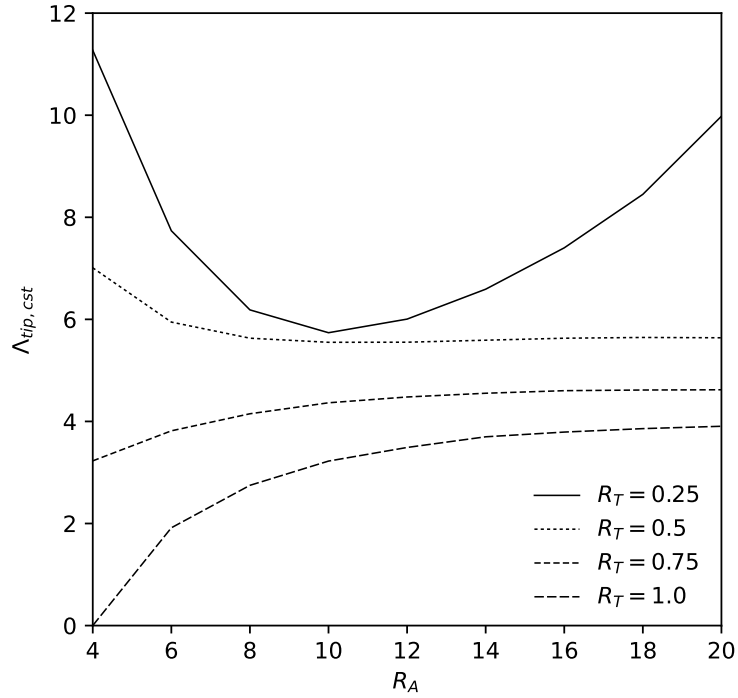


Fig. 8.17: Cross-over point between constant and linear sweep profiles in terms of equivalent constant tip sweep angle $\Lambda_{tip, cst}$ as a function of aspect ratio R_A and taper ratio R_T .

The strong curve in the line for taper ratio $R_T = 0.25$ can be explained by looking at Fig. 8.16. For aspect ratios below around 8-10, the cross-over point in terms of κ_{ac} where a crescent wing becomes more aerodynamically efficient than a wing with constant sweep does not vary much with aspect ratio. However, as aspect ratio increases, the tip sweep angle required to reach a certain κ_{ac} value decreases due to the increased span. We see that for wings with a taper ratio of $R_T = 0.25$ and aspect ratio of $R_A = 5$, a crescent wing is only potentially more efficient than a wing with constant sweep if the tip sweep angle of a constant-sweep wing is higher than around 10° , but this angle decreases to 6° for $R_A = 10$. $R_T = 0.25$ is considered a very low taper ratio. As taper ratio increases, crescent wings could the potential to decrease drag when compared to a wing with constant sweep at much lower equivalent sweep angles. For taper ratios upwards of $R_T = 0.5$, Fig. 8.17 shows that if a constant sweep angle of 4° or less is needed for the wing design, an equivalent crescent wing could show a higher aerodynamic efficiency, regardless of the aspect ratio.

8.4 COMPARISON TO ALBATROSS WING

This chapter dealt with comparing wings with a constant or linear sweep profile. Both of these two approaches are man-made and follow from either practicality in manufacturing or ease of mathematical formulation. In wings of birds or fins of fish we see neither constant sweep nor pure linear sweep. Assuming that nature always evolves to some optimum, we could expect these animals to have sweep profiles that are more efficient than the two studied in this chapter.

Albatrosses are known to be masters of gliding flight, spending only 1.2 to 14.5 percent of their flight time flapping their wings, and gliding the rest of the time [54]. In fact, thanks to their efficient wing design, they can stay aloft for days [55]. Figure 8.18 shows the wing of an albatross [56], and a simplified representation suitable for aerodynamic analysis.

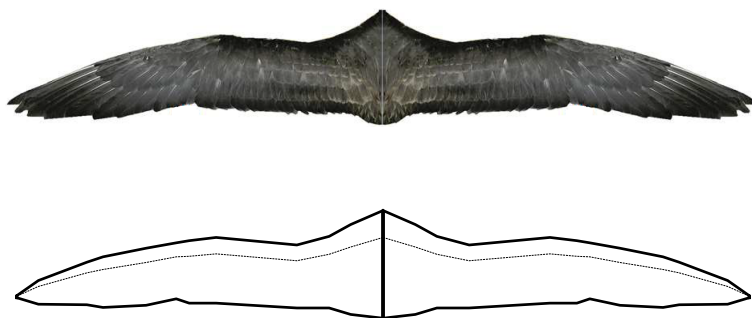


Fig. 8.18: Albatross wing geometry and model representation [7].¹

In order to calculate the κ_{ac} value for this albatross wing, we need to establish what unswept reference wing it will be compared to for the value of $(x_{ac})_{\Lambda=0}$ in Eq. 3.14. The wingspan of the albatross wing in Fig. 8.18 is 3.4m, the mean chord can be measured to be 0.27m, resulting in an aspect ratio of $R_A = 12.5$. We can't realistically measure the taper ratio of the albatross wing. Therefore, we keep the aspect ratio, wing area, and span of the reference wing equal to that of the albatross, and let that drive our taper ratio, resulting

¹Figure available via license: Creative Commons Attribution 4.0 International from Srigrarom [7]. Figure has been altered by removing the background and mirroring the wing.

in $R_T = 0.088$. Running the analysis using FlightStream with this information results in $\kappa_{ac} = 0.3674$ and $\kappa_D = 0.070$ for the albatross wing. Figure 8.19 shows a front view and isometric view of the FlightStream results for the wake and surface pressure field of the wing.

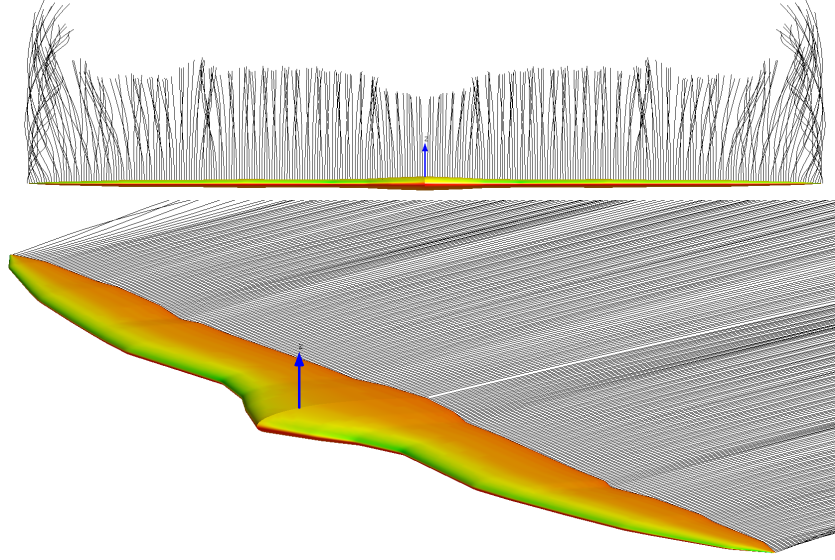


Fig. 8.19: Front view and isometric view of FlightStream results of wake and surface pressure field of the albatross wing with induced drag factor $\kappa_D = 0.070$.

As mentioned in Section 8.1, all our comparisons are done at equal aerodynamic center shift. The equivalent wings with constant sweep and linear sweep need a tip sweep angle of $\Lambda_{tip} = 8.48^\circ$ and $\Lambda_{tip} = 15.14^\circ$ to achieve the same $\kappa_{ac} = 0.3674$ value as that of the albatross wing. Figure 8.20 shows the albatross wing with the equivalent wings with constant and linear sweep superimposed. Note that in the analysis and in Fig. 8.20, the albatross wing has been scaled to match the root chord of one used in the rest of this dissertation research, but because of the aspect ratio remains the same and all reference lengths and areas are correctly adjusted, the results following from inviscid flow remain the same.

The equivalent wings with constant and linear sweep both have an induced drag factor $\kappa_D = 0.127$, higher than the result for the albatross wing, $\kappa_D = 0.070$. It therefore appears

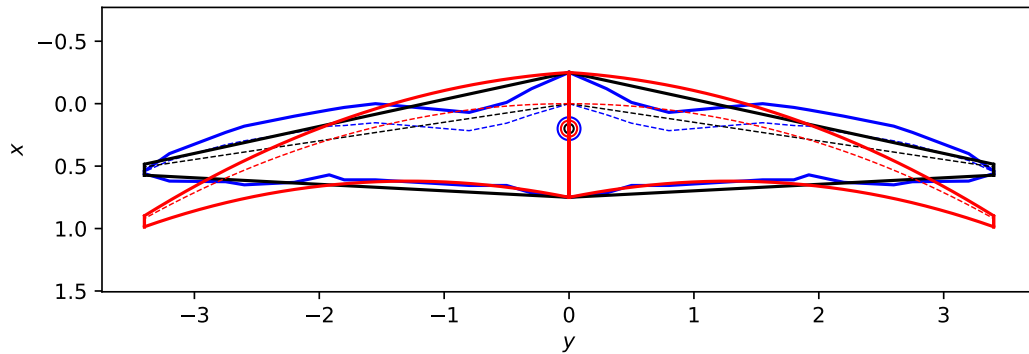


Fig. 8.20: Comparison between albatross wing and equivalent wings with constant and linear sweep profiles.

that the albatross wing is more aerodynamically efficient than both types of wing sweep. Looking at Fig. 8.20, this could be explained by the higher local angles of sweep along the span. It also has to be remembered that viscous effects are excluded from this analysis, and boundary flows in spanwise direction are likely to change the results and complicate any statements on aerodynamic efficiency.

8.5 DISCUSSION AND CONSIDERATIONS

Figures 8.16 and 8.17 are powerful figures that offer immediate use in wing design. They show the crossover point past which it makes more sense from an aerodynamic efficiency perspective to use a linear sweep profile over a constant sweep angle. They show that at least for taper ratios $R_T = 0.5$ and higher, there is a certain aspect ratio beyond which this crossover point is constant. Taper ratio $R_T = 0.25$ shows less predictable behavior. Once a designer knows where the aerodynamic center position should be to provide a suitable level of stability and control, they can decide from Fig. 8.16 whether a wing with constant or linear sweep will produce the lowest induced drag. They can use Fig. 8.17 to visualize what the equivalent level of constant sweep is, as they are likely more familiar with imagining constant sweep designs. It is shown that for a certain amount of drag, a designer can choose between either sweep profile to determine the level of stability desired.

An albatross wing is modeled and simulated to show how it is likely more aerodynamically efficient than both the wings with constant sweep as well as the crescent wings with a linear sweep profile.

One could jump to the foregone conclusion that deciding whether to go for a crescent wing or a conventional wing is a no-brainer, with the linear sweep profile posing lower κ_D values over a large space of wing designs. However, this isn't true. A large portion of current airplane designs, such as slow-flying general aviation aircraft with a conventional empennage, have no need for wing sweep. They don't face compressibility effects in their flight regime and have a horizontal stabilizer and elevator for longitudinal stability and control. The main application and possible benefit to be had is in flying wing designs, which are becoming increasingly interesting since the advent of unmanned aerial vehicles. Even there, however, there are drawbacks to a crescent wing design. While the induced drag polars show that for a certain lift coefficient C_L the induced drag coefficient C_{D_i} of a wing with linear sweep is lower than that of one with constant sweep, the generally lower κ_L value means it will have to fly at a higher angle of attack. This means that a crescent wing will likely experience separation and hence stall sooner than a wing with constant sweep, and likely not reach as high of a $C_{L,max}$ value. Due to the inviscid nature of this research, with angle of attack values well within the range of linear aerodynamics, separation or determination of $C_{L,max}$ values is outside the scope of this research.

Besides the discussion of aerodynamic efficiency not being self-evident, there are more qualitative and practical considerations to make. Wings with constant sweep have been manufactured for many decades, and crescent wings are conceivably harder to manufacture, similarly to elliptic wing planforms. This could require stiffer and heavier structures, potentially negating any benefits. Because of their wing tips being noticeable aft of those of wings with constant sweep and equal κ_{ac} values, the static elastic deformation resulting from the increased moment arm could be more significant [57]. This assumption is further justified when looking at the spanwise lift distributions in Fig. 8.8, where the wing with crescent sweep experiences more lift outboard of the wing. The added bending could make

flutter properties such as control reversal more likely and severe [58]. Crescent wings have higher local angles of sweep, especially near the wing tip, where control surfaces are often located. These high angles of sweep could potentially have effects on the effectiveness of these control surfaces [59].

The above considerations should only serve as food for thought and suggestions for future research. This dissertation is in no way trying to make quantified claims about them, as they are outside of the scope. In future research, it is also advised to investigate more types of sweep besides the constant and linear sweep profile.

CHAPTER 9

EFFECTS OF VISCOSITY ON WINGS WITH SWEEP

While the focus of this dissertation is on inviscid aerodynamics, this chapter will discuss how the results could change when including the effects of viscosity. FlightStream offers a viscous correction [24] to account for boundary layer effects based on a model by Standen [42]. While typically, simple boundary corrections consider the flow to be either laminar or turbulent, FlightStream takes transition into account when calculating the boundary layer thickness, using a transition model by Dvorak [43]. It uses a friction model from Olsen [60] to calculate the skin friction coefficient as a function of surface roughness height, boundary layer momentum thickness and boundary layer shape factor. The flow outside the boundary layer is assumed to be isentropic and subsonic, but compressible. This will be used to consider the first-order effects of viscosity on the results of this work.

While κ_D was defined as a parameter to represent induced drag without dependency on lift coefficient C_L , it can not be used verbatim when including viscous effects. Analogous to Eq. (2.10) for inviscid flow, we can write the total drag coefficient, including viscous effects, as the summation of parasitic and inviscid drag

$$C_{D_T} = C_{D_p} + C_{D_i} \quad (9.1)$$

Figure 9.1 shows the induced, parasitic drag, and total drag coefficient of a wing with a root chord of one, $R_A = 8$ and $R_T = 0.25$ and tip sweep angle $\Lambda_{tip} = 20^\circ$ featuring a constant sweep profile as a function of lift coefficient at a velocity of $V = 10m/s$ as predicted by FlightStream.

Note from Fig. 9.1 that the parasitic drag coefficient C_{D_p} shows a parabolic relationship with lift coefficient C_L due to viscous effects, increasing with increasing or decreasing lift coefficient due to the increased boundary layer thickness. Also note from Fig. 9.1 that the

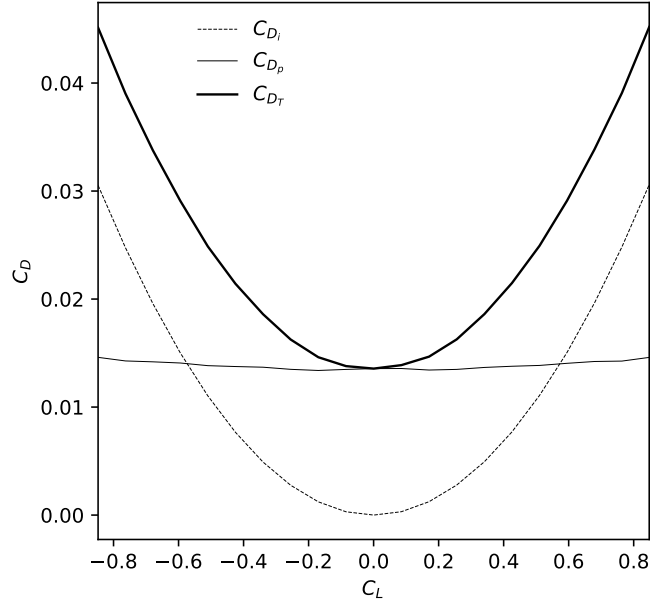


Fig. 9.1: Induced drag coefficient C_{D_i} , parasitic drag coefficient C_{D_p} and total drag coefficient C_{D_T} as a function of lift coefficient C_L for a wing with $R_A = 8$ and $R_T = 0.25$ and tip sweep angle $\Lambda_{tip} = 20^\circ$ featuring a constant sweep profile.

induced drag component is zero at zero-lift due to the use of a symmetric airfoil profile and no wing twist.

The dissertation research preceding this chapter only discussed inviscid studies because they allow for a great understanding of aerodynamic trends due to geometric design without the influence of atmospheric conditions and flight characteristics such as free stream velocity. Figure 9.2 shows induced, parasitic drag, and total drag coefficient as a function of airspeed. It shows how induced drag coefficient stays constant with increasing velocity, while the parasitic drag coefficient C_{D_p} decreases with increasing velocity because of the increasing Reynolds number.

Because the induced drag is a parabolic function of lift, and because the parasitic drag is nearly parabolic with lift, we will use the following relationship to parameterize the total drag as a function of lift:

$$C_{D_T} = C_{D_o} + \frac{C_L^2}{\pi R_A} (1 + \hat{\kappa}_D) \quad (9.2)$$

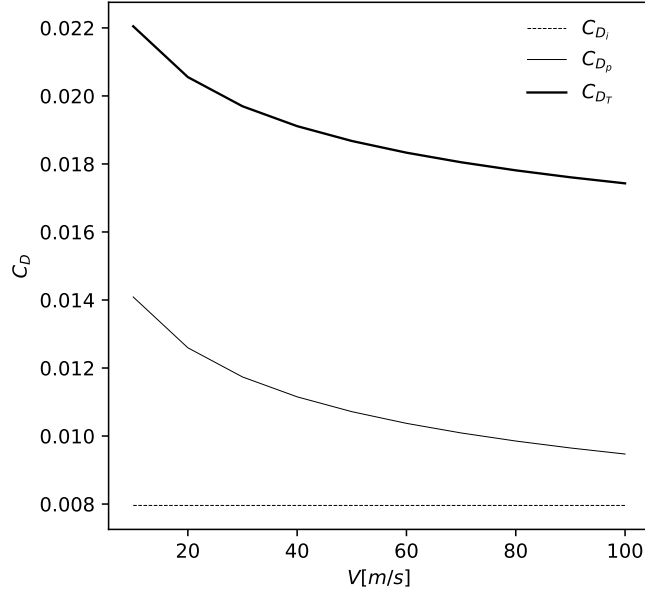


Fig. 9.2: Induced drag coefficient C_{D_i} , parasitic drag coefficient C_{D_p} and total drag coefficient C_{D_T} as a function of free stream velocity V for a wing with $R_A = 8$ and $R_T = 0.25$ without sweep, at angle of attack $\alpha = 5^\circ$.

where C_{D_o} is the drag coefficient at zero-lift. Since this research uses symmetric airfoils, this is also the drag coefficient at an angle of attack of $\alpha = 0^\circ$. For inviscid flow it results that $C_{D_o} = 0$, arriving at Eq. (2.10).

We can calculate all aerodynamic coefficients from Eq. (9.2) using FlightStream with viscous effects. All wings can be analyzed at an angle of attack of $\alpha = 0^\circ$ to find the zero-lift drag coefficient C_{D_o} . Solving Eq. (9.2) for $\hat{\kappa}_D$ results in

$$\hat{\kappa}_D = (C_{D_T} - C_{D_o}) \frac{R_A}{C_L^2} - 1 \quad (9.3)$$

Equation (9.3) can be used to calculate $\hat{\kappa}_D$ using results from two FlightStream runs with viscous effects per wing, one at zero degrees angle of attack and one at $\alpha = 5^\circ$. The results at an angle of attack of $\alpha = 5^\circ$ include the total drag coefficient and lift coefficient needed for Eq. (9.3). The resulting $\hat{\kappa}_D$ can then be used in Eq. (9.2) to calculate the total drag coefficient for that wing at an arbitrary lift coefficient C_L below stall.

In Chapter 8, the aerodynamic characteristics of wings with constant sweep and linear sweep were compared by plotting their induced drag factors κ_D versus their shift in aerodynamic center factor κ_{ac} . We can't simply plot $\hat{\kappa}_D$ versus κ_{ac} when including viscous effects because the total drag depends on both C_{D_o} and $\hat{\kappa}_D$. Instead, the total drag coefficient for each wing at the same lift coefficient, calculated using Eq. (9.2), will be used for comparison. For our study, we will use a lift coefficient of $C_L = 0.5$ for all comparisons unless specified otherwise.

In line with the preceding inviscid research, we would like to compare wings of constant sweep and linear sweep at equal aerodynamic center shift κ_{ac} as opposed to equal tip sweep angle. Therefore, total drag coefficient C_{D_T} at lift coefficient $C_L = 0.5$ will be considered as a function of κ_{ac} .

Figure 9.3 shows total drag coefficient C_{D_T} at $C_L = 0.5$ as a function of κ_{ac} for wings of aspect ratio $R_A = 8$ and taper ratio $R_T = 0.25$ using a constant and linear sweep profile with tip sweep angles ranging from $\Lambda_{tip} = 0^\circ$ to $\Lambda_{tip} = 40^\circ$.

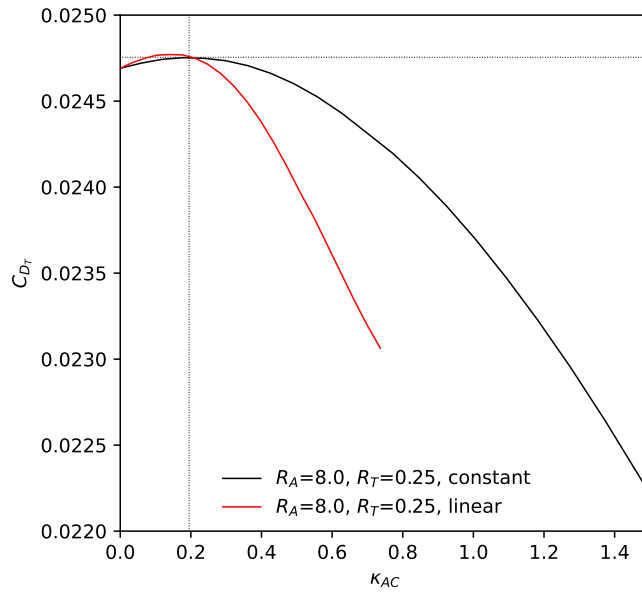


Fig. 9.3: Total drag coefficient C_{D_T} as a function of aerodynamic center shift κ_{ac} for wings with $R_A = 8$ and $R_T = 0.25$ featuring constant and linear sweep profiles at $C_L = 0.5$.

Figure 9.4 shows induced drag coefficient C_{D_i} at $C_L = 0.5$ as a function of κ_{ac} for the same set of wings as those used in Fig. 9.3. Notice that the cross-over point where wings with linear sweep produce less aerodynamic sweep than wings with constant sweep lies at roughly the same point with or without viscous effects.

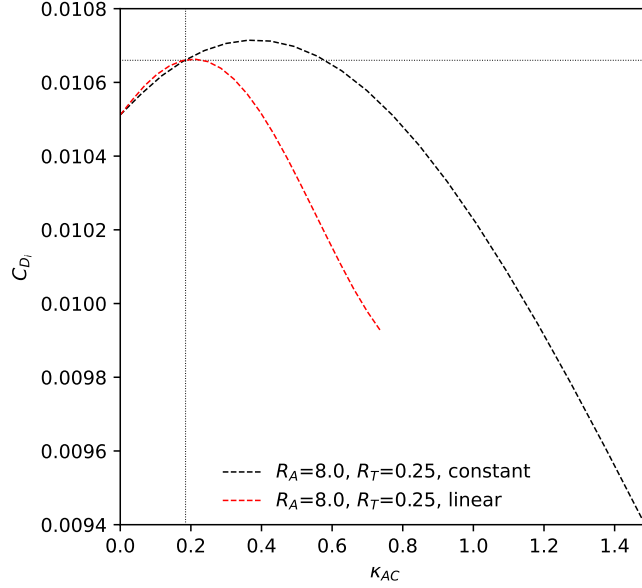


Fig. 9.4: Induced drag coefficient C_{D_i} as a function of aerodynamic center shift κ_{ac} for wings with $R_A = 8$ and $R_T = 0.25$ featuring constant and linear sweep profiles at $C_L = 0.5$.

Figures 9.5 and 9.6 show total drag coefficient C_{D_T} and induced drag coefficient C_{D_i} respectively for the same set of wings as above, evaluated at $C_L = 0.8$.

Note when comparing Figs. 9.4 and 9.6 that their curves are identical, only the absolute value of the induced drag coefficient has changed. In fact, their shapes are the same as that of κ_D in Fig. 8.3.

When comparing Figs. 9.3 and 9.5, the influence of lift coefficient C_L on viscous drag effects becomes apparent, as the cross-over point where wings with linear sweep pose a potential increase in aerodynamic efficiency over wings with constant sweep has shifted to the right, so that wings with constant sweep have a lower drag coefficient until higher equivalent sweep angles than at the lower lift coefficient of $C_L = 0.5$.

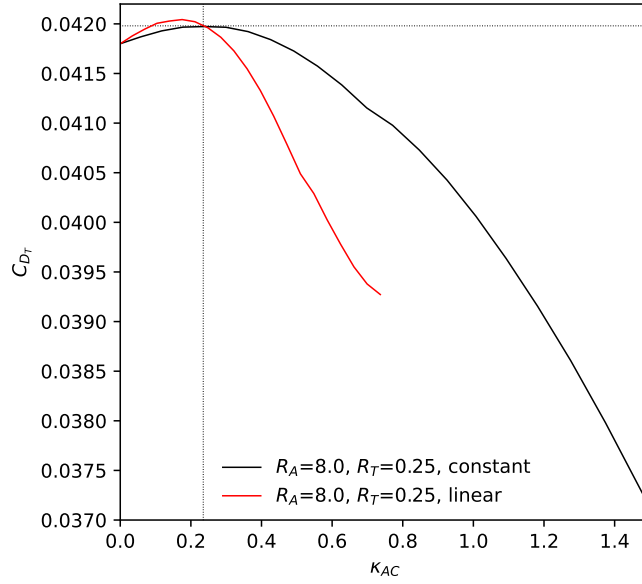


Fig. 9.5: Total drag coefficient C_{DT} as a function of aerodynamic center shift κ_{ac} for wings with $R_A = 8$ and $R_T = 0.25$ featuring constant and linear sweep profiles at $C_L = 0.8$.

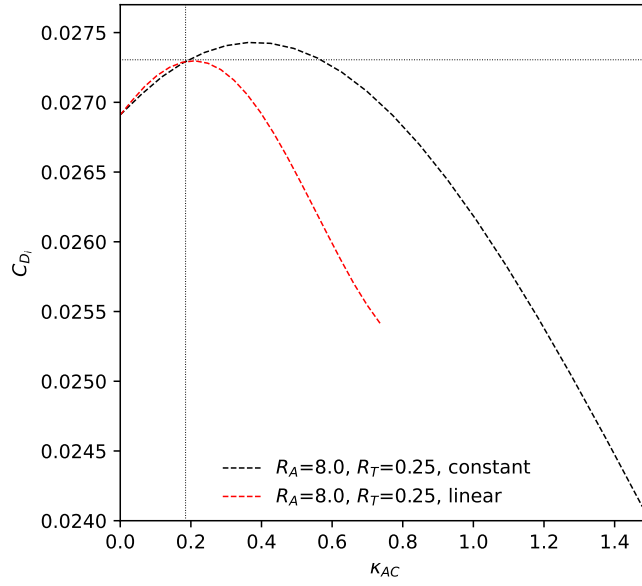


Fig. 9.6: Induced drag coefficient C_{Di} as a function of aerodynamic center shift κ_{ac} for wings with $R_A = 8$ and $R_T = 0.25$ featuring constant and linear sweep profiles at $C_L = 0.8$.

Viscous coupling for swept wings is an involved topic outside the scope of the present research. A comprehensive study on the effects of viscosity would require a significant amount of extra research, as viscous effects depend on Reynolds number, sweep angle and

lift coefficient. However, as can be seen from Figs. 9.3-9.6, the trends for total drag including viscosity are very similar to the trends found for induced drag alone in this work. Hence, the results of the present study neglecting viscosity offer great insight for understanding the effects of sweep type and angle on induced drag as a function of taper ratio and aspect ratio. The inviscid results for induced drag can be used by a designer to make a very quick comparison between a wing with constant sweep or linear sweep that will not change significantly when including viscous effects in a later, more resource intensive study.

CHAPTER 10

OPTIMIZATION OF WING SWEEP PROFILE FOR MINIMUM κ_D

Chapters 6, 7 and 8 took an in-depth look into the inviscid aerodynamics of conventional wings with constant sweep, and crescent-shaped wings with a linear sweep profile. These are not the only two types of wing planform designs. In fact, the set of crescent-shaped wings in itself contains an infinite amount of design possibilities, depending on the function governing the curvature of the quarter-chord line. It is therefore conceivable that neither of them are the most aerodynamically efficient planform shape available. This chapter uses an optimization algorithm to attempt to find solutions for the wing sweep profile that will minimize κ_D , calculated using Eq. 3.12 using data from FlightStream when ignoring viscous effects. While Chapter 9 shows that the effects of viscosity do not significantly alter the results and comparisons between wings with constant sweep and linear sweep, it is important to realize that the results from an optimization study might experience greater influence from viscosity due to the complexity of the resulting wing geometry. Still, a purely inviscid study will often be the stepping stone of any aerodynamic study involving optimization.

10.1 OPTIMIZATION SETUP

This section establishes the optimization setup and its limitations and constraints. Since this research is a study on the effects of sweep profiles on inviscid aerodynamics and to reduce the scope and number of variables in the optimization, aspect ratio R_A and taper ratio R_T are not part of the optimization process. Therefore, for a particular optimization exercise, R_A and R_T are defined as input parameters. The aspect and taper ratios fully define the spanwise chord distribution according to Eq. (3.1). With the root section fixed, the wing geometry is then completely determined by defining the longitudinal position x_{qc} of the quarter-chord sweep line. Wings are modeled using N_{span} spanwise sections, of which the innermost section, the wing root, is not allowed to vary. This means that the quarter-

chord sweep line is defined by the position of the $N_{span} - 1$ outermost sections, which the optimization algorithm is allowed to vary.

As discussed in Section 8.1, the induced drag factor κ_D is taken as performance metric, as it is nearly independent of lift coefficient C_L . Our objective function is therefore κ_D , calculated using Eq. 3.12 using data from FlightStream.

We have seen before in Section 8.1 that the factor for shift in aerodynamic center κ_{ac} of two wings should be equal in order for a fair comparison to be made. So that we can make this comparison at equal shift in aerodynamic center, κ_{ac} is taken as an inequality constraint as follows:

$$abs\left(\frac{b-a}{2}\right) - abs\left(\frac{\kappa_{ac} - (a+b)}{2}\right) \geq 0 \quad (10.1)$$

where a and b are the limits within which κ_{ac} must lie. This function is larger than zero and returns true only if κ_{ac} lies between a and b . Besides this one inequality constraint, bounds have been set on the input variable as $x_{qc} \in [-5, 5]$.

Before the optimization algorithm starts, a wing with the same aspect ratio and taper ratio as that of the wing to be optimized but with zero sweep has to be analyzed to find $\frac{(x_{ac})_{\Lambda=0}}{c_{ref}}$ in order to be able to calculate the κ_{ac} of each iteration using Eq. (3.14). The gradient-based SLSQP (Sequential Least Squares Quadratic Programming) algorithm [61] is used to optimize the objective function κ_D , which is calculated by calling FlightStream, described in Section 3.2.3. The tolerance for convergence with the SLSQP algorithm is set to $1e-3$.

During optimization, all simulations are run at a modified grid of 80 panels in spanwise direction, as opposed to the higher resolution of 160 spanwise panels used in the previous chapters, to decrease the computation time. From the grid convergence study done with FlightStream (Section 3.2.3), we see that the results for a grid with 80x80 panels is still within 6% of the finest grid of 200x80 nodes, so this is considered suitable. After the optimization is done, the resulting wings are analyzed using a grid with 160x80 panels for comparison to the rest of the results.

All optimization exercises feature wings with aspect ratio $R_A = 8$ and taper ratio $R_T = 0.25$, although with varying requirements on κ_{ac} . Throughout the discussion of the results, mention is made of reference wings. These are all wings with aspect ratio $R_A = 8$ and taper ratio $R_T = 0.25$ featuring a constant sweep angle such that they achieve the relevant κ_{ac} value that is being discussed in that particular optimization exercise.

10.2 INFLUENCE OF INITIAL GUESS

This section discusses how the solution of a gradient-based optimization effort depends on the initial guess. From Fig. 8.3 we see that the lines for a wing with constant sweep and a wing with linear sweep of aspect ratio $R_A = 8$ and taper ratio $R_T = 0.25$ cross at $\kappa_D = 0.072$ and $\kappa_{ac} = 0.19$. From Fig. 8.2, we can see that this correspond to a tip sweep angle $\Lambda_{tip} = 6.19^\circ$ for the wing with constant sweep and $\Lambda_{tip} = 10.42^\circ$ for the linearly swept wing. At this intersection, the wing with constant sweep effectively produces the same amount of drag as the wing with linear sweep. An SLSQP optimization algorithm is used to see if at this particular κ_{ac} we can find an optimal quarter-chord sweep line distribution x_{qc} that results in a lower κ_D than either of these two wing designs. For this we consider three different initial guesses for x_{qc} . The first one starts from a wing with zero sweep, the second one starts from a quarter-chord line with a constant sweep angle of $\Lambda_{tip} = 6.5^\circ$, as it is around the cross-over point at $\kappa_D = 0.072$ and $\kappa_{ac} = 0.19$, and the third guess is initialized from a wing with twice as much sweep, $\Lambda_{tip} = 13^\circ$. The goal for κ_{ac} is set with $a = 0.19$ and $b = 0.192$ in Eq. (10.1), to allow for a small margin. The optimization setups are summarized in Table 10.1.

Table 10.1: Setup of optimization cases to verify influence of initial guess.

	R_A	R_T	N_{span}	$\kappa_{ac,goal}$	$x_{qc,0}$
Wing A.I	8	0.25	5	0.19-0.192	[0, 0, 0, 0, 0]
Wing A.II	8	0.25	5	0.19-0.192	[0, 0.0712, 0.1424, 0.2136, 0.2848]
Wing A.III	8	0.25	5	0.19-0.192	[0, 0.1443, 0.2886, 0.4329, 0.5772]

The resulting wings are plotted in Fig. 10.1, with the results summarized in Table 10.2, where $\% \Delta_{ref}$ is the percentage change in κ_D with respect to the reference wing. The reference wing for all three wings in Table 10.2 is the wing with aspect ratio $R_A = 8$ and taper ratio $R_T = 0.25$ and a constant sweep profile with $\Lambda_{tip} = 6.19^\circ$. It is shown in Fig. 10.1 using a thin dashed line.

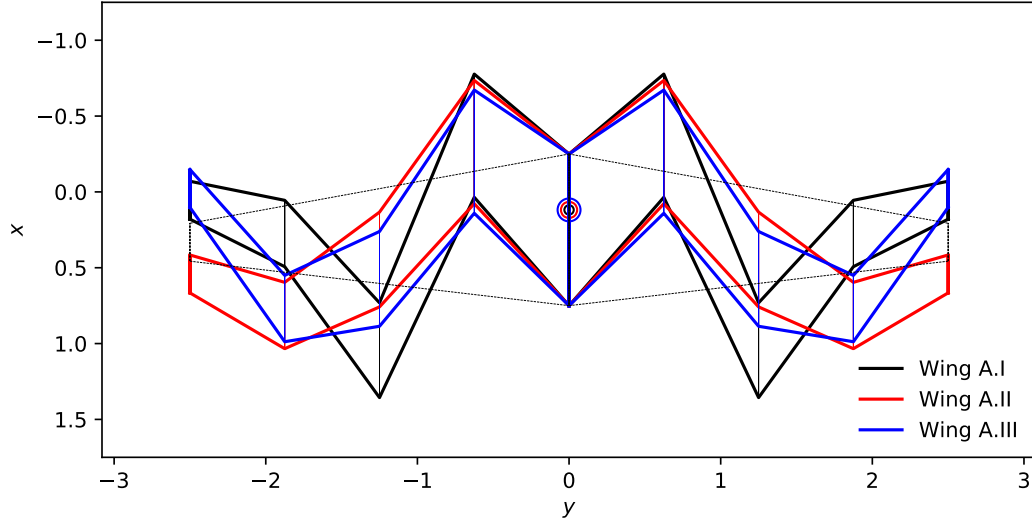


Fig. 10.1: Geometry of results of optimization cases from Table 10.2.

Table 10.2: Results of optimization cases to verify influence of initial guess.

	x_{final}	number of iterations		
Wing A.I	[0, -0.5737, 0.8875, 0.1649, -0.0077]	245		
Wing A.II	[0, -0.5317, 0.2896, 0.7056, 0.4784]	212		
Wing A.III	[0, -0.4684, 0.4173, 0.6598, -0.0854]	170		
	κ_{ac}	κ_D	$\% \Delta_{ref}$	
Wing A.I	0.19	-0.193	-367%	
Wing A.II	0.19	-0.092	-228%	
Wing A.III	0.19	-0.056	-178%	

It can be seen from Fig. 10.1 and Table 10.2 that the three different initial guesses result in significantly differing geometries that all meet the κ_{ac} constraint. We can also see that the induced drag factor κ_D for all three results are significantly reduced when

compared to the results for the reference wing, where from Fig. 8.3 we see that $\kappa_D = 0.072$. This shows that multiple quarter-chord sweep lines exist that result in lower induced drag than the constant or linear sweep distributions.

Figure 10.2 shows the spanwise lift distributions for all three wings from Table 10.2, as well as the elliptic spanwise lift distribution from an elliptic planform with no sweep and $R_A = 8$.

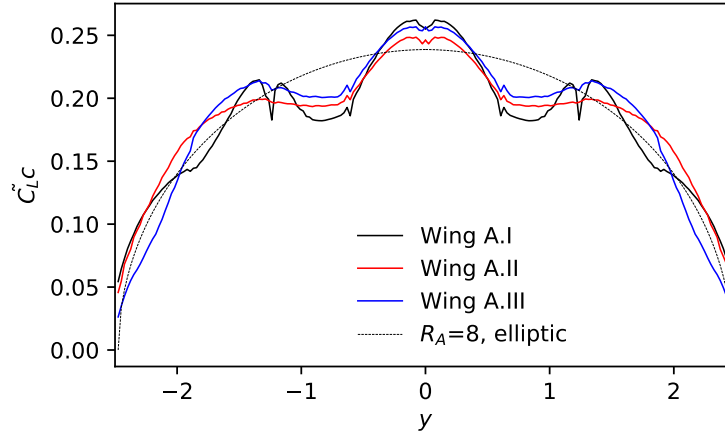


Fig. 10.2: Spanwise lift distributions of optimization cases from Table 10.2, evaluated at $C_L = 0.3$.

Despite all curves in Fig. 10.2 integrating to a global lift coefficient of $C_L = 0.3$, the curves for the optimal wings differ significantly from the elliptic spanwise lift distribution. Still, they offer a lower κ_D value according to the results in Table 10.2. This could be explained by looking at the geometry in Fig. 10.3, showing the isometric views of the surface pressure fields of all three wings from Table 10.2 respectively.

Behind the regions of high local sweep, the vorticity being shed in the wake is farther away from the lifting surface than behind regions with less sweep. Figure 10.4 shows the vortex structures in the wake behind the three wings from Table 10.2.

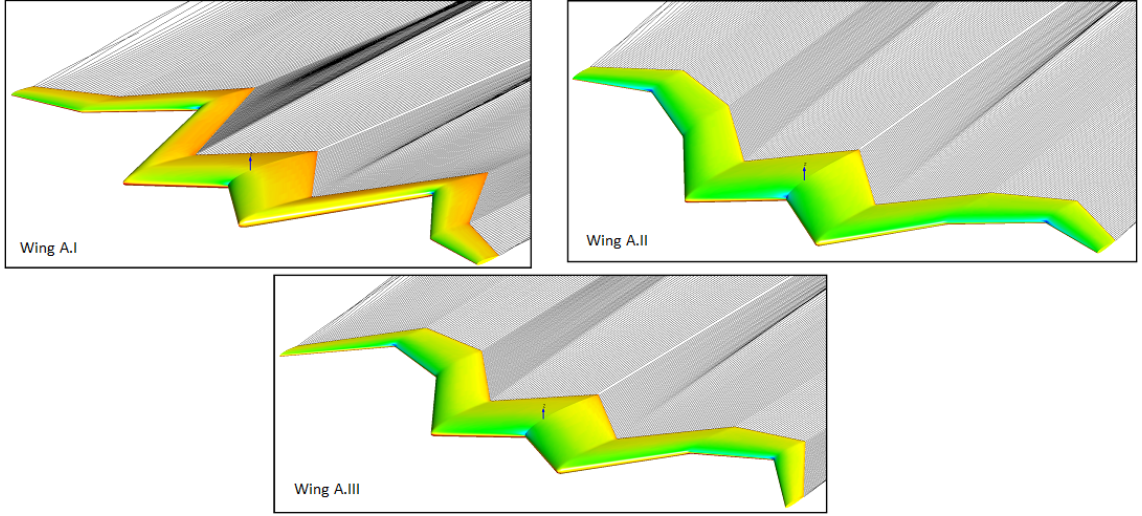


Fig. 10.3: Surface pressure fields of optimization cases from Table 10.2, evaluated at $C_L = 0.3$.

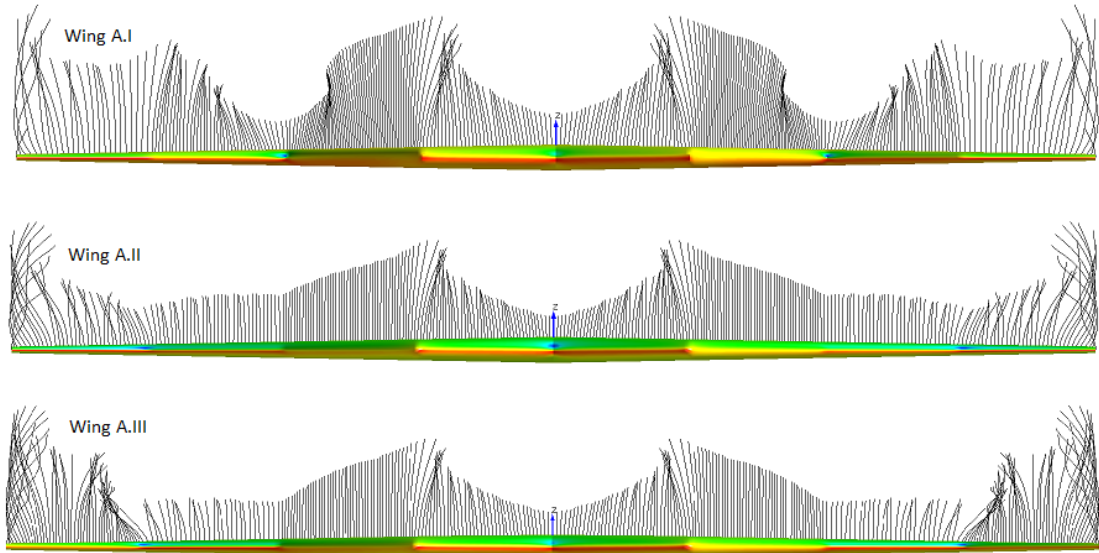


Fig. 10.4: Front views of wakes of optimization cases from Table 10.2, evaluated at $C_L = 0.3$.

The non-linear behavior of our multivariable problem means that SLSQP, a gradient based optimization solver, is not able to guarantee a global minimum. Basin-hopping is a technique in which random perturbations are made to the initial guess, followed by a local optimization with an algorithm such as SLSQP. Based on the resulting minimum function value, it will accept or reject iteration guesses. This could be useful in covering a

large space of potential solutions at the expense of significantly increased computing time. However, basin-hopping does not handle constraints in its selection of new guesses, so it could violate the inequality constraint on κ_{ac} in its selection of the initial guess. In the end, despite covering a large space, it still can't guarantee having found the global minimum, it just has more chances at finding a better solution than a gradient based optimization from just one initial guess, the result of which can vary significantly as shown in Table 10.2. This optimization chapter serves only to show the existence of solutions with less induced drag, and realizes it can't guarantee a global minimum. A global optimization study is recommended for future research.

10.3 INFLUENCE OF NUMBER OF SPANWISE SECTIONS

The wings in Section 10.2 were modeled using $N_{span} = 5$ sections and studied the effects of initial guess on the final solution. It is conceivable to think that solutions with lower induced drag can be found when increasing the number of sections. This increases the flexibility of the optimizer to modify the wing geometry by allowing it to vary the quarter chord position at more spanwise locations. We are still considering wings with aspect ratio $R_A = 8$ and taper ratio $R_T = 0.25$, and like in Section 10.2, the goal for κ_{ac} is set to $0.19 - 0.192$. Wing B.I is modeled using $N_{span} = 5$ sections, Wing B.II using $N_{span} = 7$ sections, and Wing B.III using $N_{span} = 9$ sections. To increase the convergence rate despite the increased number of sections, all three wings were initialized to a wing with constant sweep and a tip sweep angle $\Lambda_{tip} = 6.5^\circ$, so that the initial guess is closer to the desired κ_{ac} . Note that Wing B.I in this study is equal to Wing A.II in Section 10.2. The optimization setups are summarized in Table 10.3.

Table 10.3: Setup of optimization cases to verify influence of number of spanwise sections.

	R_A	R_T	N_{span}	$\kappa_{ac_{goal}}$	$x_{qc,0}$
Wing B.I	8	0.25	5	0.19-0.192	[0, 0.0712, 0.1424, 0.2136, 0.2848]
Wing B.II	8	0.25	7	0.19-0.192	[0, 0.0475, 0.0949, 0.1424, 0.1899, 0.2374, 0.2848]
Wing B.III	8	0.25	9	0.19-0.192	[0, 0.0356, 0.0712, 0.1068, 0.1424, 0.1780, 0.2136, 0.2492, 0.2848]

The resulting wings are plotted in Fig. 10.5, with the results summarized in Table 10.4. The reference wing for all three wings in Table 10.4 is the wing with aspect ratio $R_A = 8$ and taper ratio $R_T = 0.25$ and a constant sweep profile with $\Lambda_{tip} = 6.19^\circ$. It is shown in Fig. 10.4 using a thin dashed line.

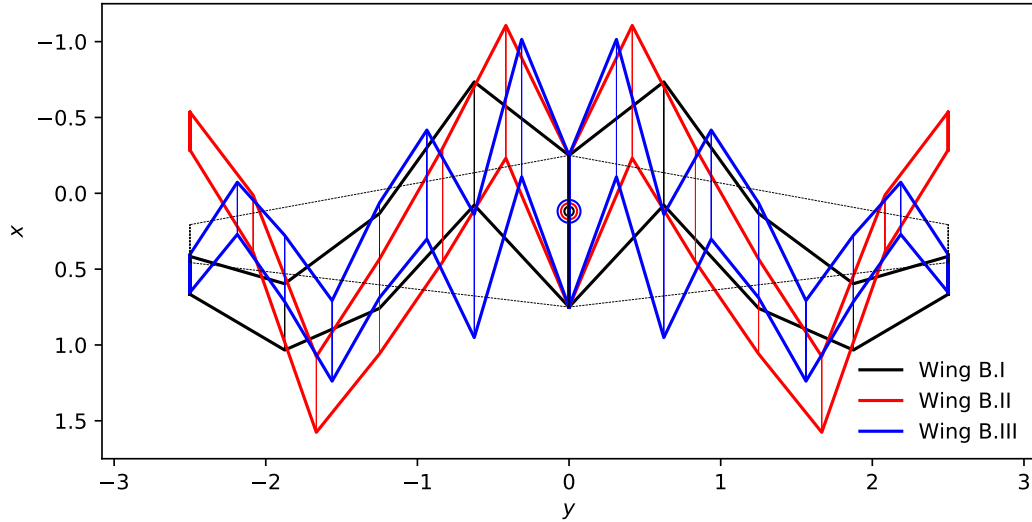


Fig. 10.5: Geometry of results of optimization cases from Table 10.3.

As we can see in Table 10.4, increasing the number of sections N_{span} allows for a decrease in the resulting κ_D , when initialized as a wing with 6.5° of constant sweep. Note that it is not guaranteed and in fact unlikely that either of these solutions is a global minimum, and that it is possible that a gradient-based optimization algorithm would have found a higher κ_D for a wing with more spanwise sections N_{span} than another wing. However, considering all three wings were initialized in the same way, it is telling that increased flexibility

Table 10.4: Results of optimization cases to verify influence of number of spanwise sections.

	x_{final}	number of iterations	
Wing B.I	[0, -0.5317, 0.2896, 0.7056, 0.4784]	212	
Wing B.II	[0, -0.8880, -0.1111, 0.5898, 1.2011, 0.1057, -0.4735]	368	
Wing B.III	[0, -0.7885, 0.3420, -0.2373, 0.2196, 0.8403, 0.3868, 0.0130, 0.4659]	877	
	κ_{ac}	κ_D	$\% \Delta_{ref}$
Wing B.I	0.19	-0.092	-228%
Wing B.II	0.19	-0.256	-455%
Wing B.III	0.19	-0.359	-597%

in geometry allows the optimizer to find a solution with lower induced drag.

10.4 RESULTS FOR OPTIMIZATIONS AT DIFFERENT κ_{ac}

The previous sections all dealt with optimizations of wings with $R_A = 8$ and $R_T = 0.25$ at $\kappa_{ac} = 0.19$. This was the cross-over point of the curves in Fig. 8.3, where the wings with constant and linear sweep of $R_A = 8$ and $R_T = 0.25$ produce the same amount of drag. This section looks at wings with $R_A = 8$ and $R_T = 0.25$ at different required shifts in aerodynamic center. This will effectively result in wings with different levels of equivalent sweep. All five wings investigated were modeled with $N_{span} = 5$ spanwise sections and initiated as a wing without sweep. Note that Wing C.III in Table 10.5 is the same as Wing A.I in Section 10.2.

Table 10.5: Setup of optimization cases at different κ_{ac} .

	R_A	R_T	N_{span}	$\kappa_{ac_{goal}}$	$x_{qc,0}$
Wing C.I	8	0.25	5	0.0-0.002	[0, 0, 0, 0, 0]
Wing C.II	8	0.25	5	0.1-0.102	[0, 0, 0, 0, 0]
Wing C.III	8	0.25	5	0.19-0.192	[0, 0, 0, 0, 0]
Wing C.IV	8	0.25	5	0.3-0.302	[0, 0, 0, 0, 0]
Wing C.V	8	0.25	5	0.4-0.402	[0, 0, 0, 0, 0]

The resulting wings are plotted in Fig. 10.6, with the results summarized in Table 10.6. Note that the reference wings in this study are not the same. They are all wings with

aspect ratio $R_A = 8$ and taper ratio $R_T = 0.25$ featuring a constant sweep profile, but their tip sweep angle Λ_{tip} is such that the κ_{ac} of the appropriate reference wing matches that of the optimized wing. Because there are multiple reference wings, they have been omitted from Fig. 10.6 to preserve legibility.

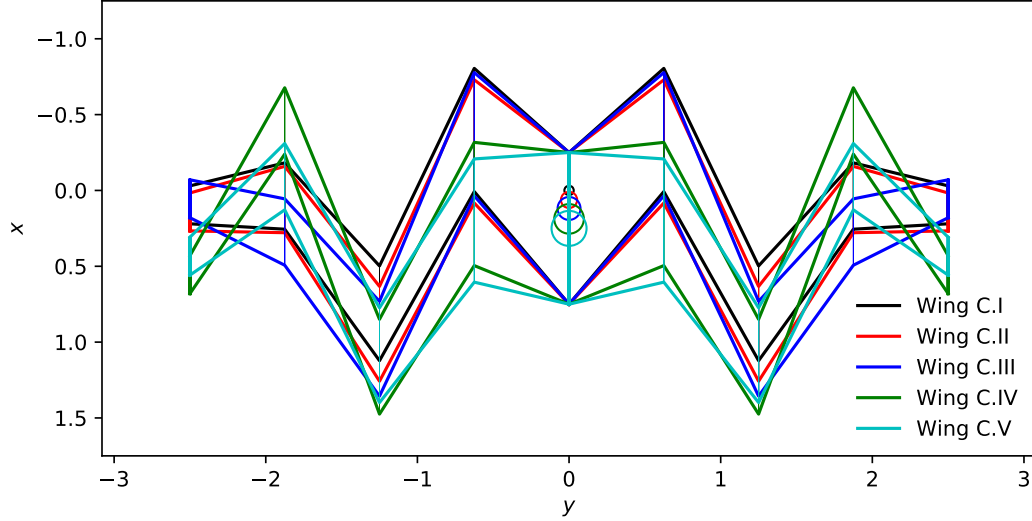


Fig. 10.6: Geometry of results of optimization cases from Table 10.6.

Table 10.6: Results of optimization cases at different κ_{ac} .

	x_{final}	number of iterations	
Wing C.I	[0, -0.6017, 0.6537, -0.0726, 0.0324]	364	
Wing C.II	[0, -0.5264, 0.7889, -0.0494, 0.0792]	266	
Wing C.III	[0, -0.5737, 0.8875, 0.1649, -0.0077]	245	
Wing C.IV	[0, -0.1139, 1.0059, -0.5676, 0.4928]	822	
Wing C.V	[0, -0.0047, 0.9299, -0.2002, 0.3708]	479	
	κ_{ac}	κ_D	$\% \Delta_{ref}$
Wing C.I	0.00	-0.197	-448%
Wing C.II	0.10	-0.177	-369%
Wing C.III	0.19	-0.193	-367%
Wing C.IV	0.30	0.104	+63%
Wing C.V	0.40	-0.011	-114%

The first thing to note from the results in Table 10.6 is that the optimization attempt for Wing C.IV resulted in a higher κ_D than the reference wing with constant sweep, which had a value of $\kappa_D = 0.076$. This is proof that a gradient based optimization algorithm can get stuck in a local minimum. From Fig. 10.6, it can be seen that the inboard wing section carries a lot of weight in the determination of κ_{ac} , since the wings with higher κ_{ac} constraints show less forward sweep in the inboard section than the wings with a lower required aerodynamic center shift. Another thing of interest is that, barring Wing C.IV, $\% \Delta_{ref}$ appears to become increasingly less negative with increasing κ_{ac} . While care should be taken not to jump to rash conclusions, there is a possible explanation for this. Throughout these optimization exercises it has become clear that the optimization algorithm wants to make use of high local forward and rearward sweep angles to minimize κ_D . This can likely be explained by looking at Fig. 6.2, where κ_D is seen to decrease with increasing sweep angle. Wings with constant sweep and a high κ_{ac} value already feature higher sweep angles than wings with a lower κ_{ac} value. There is therefore likely less possibility in decreasing κ_D by changing the local sweep angles.

10.5 DISCUSSION AND CONSIDERATIONS

This chapter made clear that there exist more aerodynamically efficient sweep profiles than both the constant and linear sweep profile when considering purely inviscid solutions. An optimization algorithm is a good way at finding optimal solutions, but it is hard, if not impossible, to guarantee a global minimum without a good functional description for the problem. The use of SLSQP, a gradient-based optimization algorithm, means it is easy to get stuck in a local minimum. In a real-life design scenario, it is advised to start multiple optimization exercises from different initial guesses, or use basin-hopping techniques, to increase the chance of finding a global optimum. This is definitely a worthwhile area for future research.

It is obvious from the resulting geometries that the optimization algorithm seeks wings with areas of high local forward and rearward sweep, making the manufacturability of the resulting geometries somewhat unlikely. Constraints for maximum changes in sweep should

be put in place to remedy this. While increasing the number of sections N_{span} for the optimizer to vary allows for more flexibility to find a solution with less induced drag, it has to be realized that the resulting wing becomes increasingly unfeasible to manufacture. It is also conceivable that the effects of viscosity will be more noticeable in these complex wing geometries. Chapter 9 showed that including viscosity does not significantly alter the main findings of this work, but that is possibly due to the continuous nature of the sweep profile of the wings with constant and linear sweep used in the comparison. In this inviscid optimization exercise, the gradient-based optimization algorithm seeks areas of high local sweep, because of the decreasing effect sweep has on κ_D . When including spanwise flow, it is possible that the boundary layer looks very complex in these areas of discontinuity in the sweep profile, greatly altering the results from optimization. A more detailed study focused on aerodynamic optimization is recommended.

In regards to the high local angles of sweep, note the remarks made in Section 8.5 about the maximum lift coefficient $C_{L,max}$. It is likely that these wings resulting from the optimization algorithm, while producing a lower κ_D , are limited by their capabilities in lift due to flow separation.

CHAPTER 11

CONCLUSIONS

Wing sweep in low-speed applications serves to provide longitudinal stability and control by shifting the aerodynamic center with respect to the center of gravity. Most current solutions in airplanes are limited to wings using a constant wing sweep angle throughout the span from wing root to wing tip. Nature, however, uses curved, crescent-shaped solutions in the design of birds' wings and fish' fins. Considering that nature uses evolution to find efficient solutions, it is conceivable that these crescent sweep profiles offer benefits over the constant sweep profiles, for example in terms of aerodynamic efficiency.

A theoretical background to finite wing aerodynamics was presented using existing literature. From Prandtl's classical lifting-line theory, factors can be defined to evaluate the penalty of taper ratio R_T and aspect ratio R_A on the lift-slope and induced drag coefficient. Plots for these factors κ_L and κ_D , have been published by, among others, Glauert [28] and Phillips [19], showing that a taper ratio of $R_T = 0.4$ will minimize induced drag. Küchemann [1] presented an analytic solution for the locus of section aerodynamic centers of swept wings. This is an important curve in aerodynamics and stability. Starting from developments by Hunsaker, Pope, and [30], a modern method to calculate the aerodynamic center position for any spanwise section on a finite wing was presented. This was used to compare the results from a numerical method for the locus of aerodynamic centers to the analytic derivation by Küchemann.

Throughout the present research, different numerical methods were used for predicting the aerodynamic properties of finite wings in inviscid flow. Wings were analyzed using the modern numerical lifting line algorithm MachUpX, an open source high order panel code PANAIR, and a modern, commercially available panel code FlightStream. All three numerical methods were discussed with appropriate grid convergence studies for each of the methods. Crescent wings were analyzed using FlightStream, so a separate convergence

study on the required smoothness of the sweep profile was presented. Results from these numerical methods were used to evaluate κ_L , κ_D , δ_L and κ_{ac} over a wide range of wing planforms with varying sweep angles and profiles.

Analytical and numerical results using MachUpX and FlightStream for κ_L and κ_D for wings without sweep were compared. The results are shown in Figs. 4.1 and 4.2. While there are differences between both numerical methods due to different levels of fidelity, the trends they follow with aspect and taper ratio are largely the same. The results for numerical and analytical lifting-line theory are near-identical as expected, and all three methods confirm the historical finding of minimal induced drag around taper ratio $R_T = 0.4$ for wings without twist. For low aspect ratios, FlightStream tends to show different trends, even resulting in negative κ_D values for $R_A = 4$. This is likely because MachUpX, a lifting-line development, is less suited for low aspect ratios than the inviscid panel code FlightStream, which is able to capture chordwise vorticity.

The analytical solutions for the locus of section aerodynamic centers by Küchemann are shown to be very accurate when evaluated against computed results from the inviscid panel code PANAIR. The analytical method was compared to the numerical method over a wide range of elliptic wing designs with varying aspect ratios and sweep angles. The numerical and analytical results for the locus are very close to each other, even capturing the effects of airfoil thickness. The RMS error between the two methods remains under 4% for all wings with aft sweep and aspect ratios higher than $R_A = 5$. The RMS error is actually skewed by the error at the wing tip, where the very small local chord magnifies the error between the two methods. Over the vast majority of the span, the error is much smaller than the RMS error. Since Küchemann's analytical solutions appear to deviate more from the numerical result for forward swept wings than for rearward swept wings, more care has to be taken when using the analytical approach to model the locus of section aerodynamic centers of forward-swept wings. Again, the RMS error is mostly skewed by the tip results. This finding could potentially be used in future efforts to improve the accuracy of numerical lifting-line algorithms for swept-wing analysis. They currently model the bound vorticity of

the wing along its quarter-chord line as an approximation for the aerodynamic center, but using the locus of section aerodynamic centers as predicted by Küchemann instead could offer a better result.

Numerical results using FlightStream for δ_L , κ_D , and κ_{ac} were computed for wings with constant sweep and linear sweep in inviscid flow as a function of taper ratio, aspect ratio, and tip sweep angle. Results are shown in Figs. 6.1, 6.2, 6.3, 7.1, 7.2, and 7.3. The lift slope factor δ_L behaves very similarly between the wings with constant sweep and linear sweep. The penalty on lift slope is seen to be higher for high aspect ratio wings than for low aspect ratio wings, although above aspect ratio $R_A = 8$, δ_L is not very sensitive to aspect ratio. As taper ratio increases, the sensitivity of δ_L with aspect ratio decreases. At low taper ratios, the results for κ_D for wings with linear sweep show flatter curves than for wings with constant sweep, although at high taper ratios the crescent wings can achieve lower κ_D values than for conventionally swept wings. It is shown that κ_D can in fact be negative for swept wings. This only means that the induced drag coefficient is lower than the induced drag coefficient of an elliptic wing with no sweep and the same aspect ratio. It does not mean that the spanwise lift distribution of the swept wing in question is in itself more efficient than if an elliptic spanwise lift distribution were to be used for the swept wing as well. The results for κ_{ac} show expected trends for both wing types, increasing as sweep increases, denoting an aft shift in aerodynamic center position. For a constant tip sweep angle Λ_{tip} , the wing with linear sweep achieves a lower κ_{ac} value than a wing with constant sweep, since its lifting surface lies in front of the imaginary line connecting the quarter-chord points of the wing root and wing tip.

In-depth comparisons are made between wings with constant and wings with linear sweep. Induced drag factor κ_D was used as the measure of aerodynamic efficiency and as a metric to compare between different wings. In Section 8.1 it is explained why wings should be compared at equal aerodynamic center shift κ_{ac} for fair comparison. A wing with constant sweep and linear sweep can be compared using their κ_{ac} - κ_D curves, as shown in Fig. 8.3. At the intersection of the curves in this figure, both sweep types produce the same

amount of aerodynamic center shift and induced drag. Using numerical data it is proven that κ_D is nearly independent of lift coefficient C_L . This intersection can be seen as the cross-over point below which wings with constant sweep are more aerodynamically efficient, and above which crescent wings can be more aerodynamically efficient. Figures 8.16 and 8.17 show this cross-over point in terms of aerodynamic center shift or equivalent constant tip sweep angle as a function of aspect ratio and taper ratio. It is shown that as taper ratio increases, this cross-over point moves left, making wings with linear sweep potentially more aerodynamically efficient over a wider range of applications. For example, for $R_T = 0.25$ and $R_A = 4$, a linear sweep profile is only more aerodynamically efficient as soon as the required equivalent constant sweep angle is over 10° . This required equivalent constant sweep angle decreases for increasing taper ratio, and for taper ratios above $R_T = 0.5$, it is nearly independent of aspect ratio above $R_A = 10$.

A study of the albatross wing showed that it is likely more aerodynamically efficient than both the constant and linear sweep profile. Figure 8.20 shows the wing of an albatross compared to equivalent wings using constant and linear sweep profiles producing the same shift in aerodynamic center. The albatross wing produces an induced drag factor of $\kappa_D = 0.070$, while the two other wings produce an induced drag factor of $\kappa_D = 0.127$. This is 81% higher than that of the albatross wing.

Chapter 9 takes into account effects of viscosity to show that these do not significantly alter the findings of the inviscid research. A change in lift coefficient C_L can slightly shift the cross-over point where wings with linear sweep produce less induced drag than wings with constant sweep as compared to the cross-over point in inviscid flow, but the overall downward trend and its slope stay largely unchanged. The cross-over point for total drag coefficient does not vary by much from the cross-over point when considering just induced drag coefficient. The conclusions from comparing the induced drag of the two types of wing sweep in inviscid flow remain useful to a wing designer even when excluding viscosity. As shown, they offer great insight for understanding the effects of sweep type and angle on induced drag as a function of taper ratio and aspect ratio.

Some considerations to be made when deciding between constant or linear sweep were presented. It is conceivable that wings with a linear sweep profile are harder to manufacture, making them potentially heavier and negating the positive effects of a lower κ_D . Stall characteristics are outside the scope of this research, and it is possible that crescent wings need to fly at higher angles of attack to achieve certain lift coefficients, potentially limiting their $C_{L,max}$ and hence their applications. It is also suggested that perhaps control surfaces are less effective along the highly swept outboard sections of a wing with linear sweep.

Several optimization studies were performed to see if wing sweep profiles resulting in less induced drag than the constant and linear sweep could be found. It was shown that this is in fact possible, and Fig. 10.1 showed that the optimization results are highly dependent on initial guess. Increasing the number of spanwise sections for the optimizer to vary increases its flexibility in finding a solution with less induced drag, as shown in Fig. 10.5. All optimal solutions made use of high local sections of sweep, lowering the induced drag factor κ_D . It is suggested that these optimized wing results could suffer from similar lift restrictions as crescent wings with linear sweep. The results from the optimization study will likely change significantly when including viscous effects. As shown, a purely inviscid aerodynamic study will lead to local areas of high local sweep with strong discontinuities in the sweep profile, because it leads to lower induced drag in inviscid flow. The spanwise flow of the boundary layer will likely be very complex at these areas of severe changes in sweep angle, leading to a different result. Still, an inviscid study is a logical first step in an aerodynamic optimization and offers some insight quickly.

This research analyzed a very broad range of wing planforms with varying aspect ratio, taper ratio, sweep angles and sweep profiles. By making use of a computationally efficient inviscid panel code, a lot of datapoints could be computed to create a map of results that is sensitive to its input parameters. The figures in this research provided an overview of how the lift, induced drag, and aerodynamic center characteristics of wings change with different sweep profiles. It compared wings with constant sweep and linear sweep using figures such that a reader could decide which sweep type is more efficient in a certain application. This

research could be further progressed by including the effects of viscosity. It is possible that the flow of the boundary layer in spanwise direction could affect the trends with increasing sweep. It is also suggested to look at different predetermined sweep profiles, such as a quadratic profile. This research used optimization algorithms to find optimal sweep profiles for particular scenarios, without making any claims to global optimality. Future research could use more complex optimization algorithms to guarantee finding a global optimum. Future research could include high-fidelity CFD results or experimental wind tunnel results for validation of the findings.

REFERENCES

- [1] D. Kuchemann, "A simple method for calculating the span and chordwise loading on straight and swept wings of any given aspect ratio at subsonic speed." Aeronautical Research Council London, Tech. Rep., 1956.
- [2] F. W. Boltz and C. D. Kolbe, "The forces and pressure distribution at subsonic speeds on a cambered and twisted wing having 45 of sweepback, an aspect ratio of 3, and a taper ratio of 0.5," *NACA RMA52D22*, 1952.
- [3] I. Hall and E. Rogers, "Experiments with a tapered sweptback wing of warren 12 planform at mach numbers between 0.6 and 1.6," *RM-3271, Aeronautical Research Council, London*, 1962.
- [4] R. R. Graham, "Low-speed characteristics of a 45 sweptback wing of aspect ratio 8 from pressure distributions and force tests at reynolds numbers from 1,500,000 to 4,800,000," *NACA RM-L51H13*, 1951.
- [5] J. Weber and G. Brebner, "Low speed tests on a 45-deg swept back wings, part-i: Pressure measurements on wings of aspect ratio 5," *RM-2882, Aeronautical Research Council, London*, 1958.
- [6] W. Phillips, D. F. Hunsaker, and R. Niewoehner, "Estimating the subsonic aerodynamic center and moment components for swept wings," *Journal of Aircraft*, vol. 45, no. 3, pp. 1033–1043, 2008.
- [7] S. Srigrarom and W.-L. Chan, "Ornithopter type flapping wings for autonomous micro air vehicles," *Aerospace*, vol. 2, no. 2, pp. 235–278, 2015.
- [8] A. Busemann, "Aerodynamischer auftrieb bei überschallgeschwindigkeit," *Luftfahrtforschung*, vol. 12, no. 6, pp. 210–220, 1935.
- [9] E. Obert, *Aerodynamic design of transport aircraft*. IOS press, 2009.
- [10] R. Storck, *Flying Wings: die historische Entwicklung der Schwanzlosen-und Nurflügelflugzeuge der Welt*. Bernard & Graefe, 2003.
- [11] A. Summers and J. Mahannah, "On swift wings: What airplane designers could learn from the shape-changing wings of birds." *Natural history*, vol. 117, no. 2, pp. 42–43, 2008.
- [12] G. Poulton, "Wing of the future," Apr 2019. [Online]. Available: <https://www.airbus.com/newsroom/news/en/2017/01/Wings-of-the-future.html>
- [13] D. Walker, D. Liu, and A. L. Jennings, "Wing design utilizing topology optimization and additive manufacturing," in *57th AIAA/ASCE/AHS/ASC Structures, Structural Dynamics, and Materials Conference*, 2016, p. 1246.

- [14] C. Van Dam, “Induced-drag characteristics of crescent-moon-shaped wings,” *Journal of Aircraft*, vol. 24, no. 2, pp. 115–119, 1987.
- [15] C. P. van Dam, “Efficiency characteristics of crescent-shaped wings and caudal fins,” *Nature*, vol. 325, no. 6103, pp. 435–437, 1987.
- [16] S. C. Smith and I. M. Kroo, “Computation of induced drag for elliptical and crescent-shaped wings,” *Journal of aircraft*, vol. 30, no. 4, pp. 446–452, 1993.
- [17] S. Smith and I. Kroo, “A closer look at the induced drag of crescent-shaped wings,” in *Flight Simulation Technologies Conference and Exhibit*, 1990, p. 3063.
- [18] J. Weissinger, “The lift distribution of swept-back wings,” *Zentrale fuer Wissenschaftliches Berichtswesen der Luftfahrtforschung des Generalflugzeugmeisters*, no. 1553, 1947.
- [19] W. Phillips and D. Snyder, “Modern adaptation of prandtl’s classic lifting-line theory,” *Journal of Aircraft*, vol. 37, no. 4, pp. 662–670, 2000.
- [20] J. T. Reid and D. F. Hunsaker, “A general approach to lifting-line theory, applied to wings with sweep,” in *AIAA Scitech 2020 Forum*, 2020, p. 1287.
- [21] C. E. Lan, “A quasi-vortex-lattice method in thin wing theory,” *Journal of Aircraft*, vol. 11, no. 9, pp. 518–527, 1974.
- [22] B. Litherland, “Using vsp aero,” 2015, last accessed 8 December 2020. [Online]. Available: <http://openvsp.org/wiki/doku.php?id=vspaerotutorial>
- [23] A. Magnus and M. Epton, “A computer program for predicting subsonic or supersonic linear potential flows about arbitrary configurations using a higher order panel method, vol. i. theory document (version 1.0),” *NASA Contractor Report*, vol. 3251, p. 18, 1980.
- [24] V. Ahuja, R. J. Hartfield, and D. Ciliberti, “Three-dimensional viscous coupling and flow separation enhancements to an inviscid surface vorticity flow solver,” in *2022 AIAA AVIATION Forum*, 2022.
- [25] L. Prandtl, “Tragflügel theorie,” *Nachrichten von der Gesellschaft der Wissenschaften zu Göttingen*, pp. 451–477, 1918.
- [26] W. Phillips, D. F. Hunsaker, and R. Niewoehner, “Estimating the subsonic aerodynamic center and moment components for swept wings,” *Journal of aircraft*, vol. 45, no. 3, pp. 1033–1043, 2008.
- [27] W. F. Phillips, *Mechanics of Flight*, 2nd ed. John Wiley & Sons, 2010.
- [28] H. Glauert, *A method of calculating the characteristics of a tapered wing*. HM Stationery Office, 1922.
- [29] W. Phillips, N. Alley, and R. Niewoehner, “Effects of nonlinearities on subsonic aerodynamic center,” *Journal of Aircraft*, vol. 45, no. 4, pp. 1244–1255, 2008.

- [30] D. F. Hunsaker, O. D. Pope, J. D. Hodson, and J. Rosqvist, "Aerodynamic centers of arbitrary airfoils," in *2018 AIAA Aerospace Sciences Meeting*, 2018, p. 1276.
- [31] O. Pope, "The aerodynamic center of inviscid airfoils," 2017.
- [32] B. Moorthamers and D. F. Hunsaker, "Aerodynamic center at the root of swept, elliptic wings in inviscid flow," in *AIAA Scitech 2019 Forum*, San Diego, California, Jan. 2019.
- [33] S. C. Chapra and R. P. Canale, *Numerical methods for engineers*. Mcgraw-hill New York, 2011, vol. 1221.
- [34] I. B. Celik, "Journal of fluids engineering editorial policy statement on the control of numerical accuracy," 2000.
- [35] W. F. Phillips, S. R. Fugal, and R. E. Spall, "Minimizing induced drag with wing twist, computational-fluid-dynamics validation," *Journal of Aircraft*, vol. 43, no. 2, pp. 437–444, March-April 2006.
- [36] C. D. Goates and D. F. Hunsaker, "Practical implementation of a general numerical lifting-line method," in *AIAA Scitech 2021 Forum*, 2021, p. 0118.
- [37] C. Harvey, V. Baliga, C. Goates, D. Hunsaker, and D. Inman, "Gull-inspired joint-driven wing morphing allows adaptive longitudinal flight control," *Journal of the Royal Society Interface*, vol. 18, no. 179, p. 20210132, 2021.
- [38] J. Thomas and D. Miller, "Numerical comparisons of panel methods at subsonic and supersonic speeds," in *17th Aerospace Sciences Meeting*, 1979, p. 404.
- [39] H. Sytsma, B. L. Hewitt, and P. Rubbert, "A comparison of panel methods for subsonic flow computation," Advisory Group for Aerospace Research and Development Neilly-sur-Seine, Tech. Rep. AGARD-AG-241, 1979.
- [40] J. Thomas, J. Luckring, and W. Sellers, III, "Evaluation of factors determining the accuracy of linearized subsonic panel methods," in *Applied Aerodynamics Conference*, 1983, p. 1826.
- [41] V. Ahuja and R. Hartfield, "Aerodynamic loads over arbitrary bodies by method of integrated circulation," *Journal of Aircraft*, vol. 53, no. 6, pp. 1719–1730, 2016.
- [42] N. Standen, "Calculation of integral parameters of a compressible turbulent boundary layer using a concept of mass entrainment." 1964.
- [43] F. A. Dvorak, B. Maskew, and F. A. Woodward, "Investigation of three-dimensional flow separation on fuselage configurations." ANALYTICAL METHODS INC BELLEVUE WASH, Tech. Rep., 1977.
- [44] B. Sandoz, V. Ahuja, and R. J. Hartfield, "Longitudinal aerodynamic characteristics of a v/stol tilt-wing four-propeller transport model using a surface vorticity flow solver," in *2018 AIAA Aerospace Sciences Meeting*, 2018, p. 2070.

- [45] S. Johnson, R. J. Hartfield, D. van Dommelen, and V. Ahuja, "Investigation of the static longitudinal characteristics of a full-scale light single-engine airplane using a surface vorticity solver," in *2018 AIAA Aerospace Sciences Meeting*, 2018, p. 1259.
- [46] E. D. Olson and C. W. Albertson, "Aircraft high-lift aerodynamic analysis using a surface-vorticity solver," in *54th AIAA Aerospace Sciences Meeting*, 2016, p. 0779.
- [47] S. Geuther and X. Fei, "La-8 computational analysis and validation studies using flightstream," in *AIAA SciTech 2021 Forum*, 2021, p. 1191.
- [48] T. Owens, "Close-proximity flight validation analysis with flightstream," 2019.
- [49] X. Fei, "Evaluation of a commercial surface vorticity flow solver for the modeling of propeller-wing interaction," in *AIAA Scitech 2019 Forum*, 2019, p. 1046.
- [50] "Flightstream case studies via wayback machine," <http://web.archive.org/web/20210227115130/https://researchinflight.com/casestudies.html>, accessed: 2021-08-01.
- [51] B. Moorthamers and D. F. Hunsaker, "Accuracy of Küchemann's prediction for the locus of aerodynamic centers on swept wings," in *AIAA Scitech 2020 Forum*, Orlando, Florida, Jan. 2020.
- [52] E. Torenbeek, *Advanced aircraft design: conceptual design, analysis and optimization of subsonic civil airplanes*. John Wiley & Sons, 2013.
- [53] C. W. Burkett, "Reductions in induced drag by the use of aft swept wing tips," *The Aeronautical Journal*, vol. 93, no. 930, pp. 400–405, 1989.
- [54] K. Sato, K. Q. Sakamoto, Y. Watanuki, A. Takahashi, N. Katsumata, C.-A. Bost, and H. Weimerskirch, "Scaling of soaring seabirds and implications for flight abilities of giant pterosaurs," *PloS one*, vol. 4, no. 4, p. e5400, 2009.
- [55] G. Sachs, J. Traugott, A. P. Nesterova, G. Dell'Omo, F. Kümmeth, W. Heidrich, A. L. Vyssotski, and F. Bonadonna, "Flying at no mechanical energy cost: disclosing the secret of wandering albatrosses," 2012.
- [56] A. Stempeck, M. Hassanalian, and A. Abdelkefi, "Aerodynamic performance of albatross-inspired wing shape for marine unmanned air vehicles," in *2018 Aviation Technology, Integration, and Operations Conference*, 2018, p. 3899.
- [57] R. L. Bisplinghoff, H. Ashley, and R. L. Halfman, "Static aeroelastic phenomena - swept wings," in *Aeroelasticity*, 2nd ed. Addison-Wesley Publishing Company, Inc, 1957, ch. 8, pp. 474–516.
- [58] W. F. Phillips, "Aileron reversal," in *Mechanics of Flight*, 2nd ed. John Wiley Sons, Inc., 2010, ch. 6, pp. 679–682.
- [59] C. of Engineering Purdue University, "AAE 556 Aeroelasticity, Lecture Notes 13: Control Effectiveness," uRL: https://engineering.purdue.edu/AAECourses/aae556/2011/AAE556-Lecture_13.Swept-wing.control.reversal. Last visited on 2021/07/28.

- [60] A. S. Olsen, N. Ramos-García, and C. Bak, “Improved roughness model for turbulent flow in 2d viscous-inviscid panel methods,” *Wind Energy*, vol. 23, no. 3, pp. 608–616, 2020.
- [61] D. Kraft *et al.*, “A software package for sequential quadratic programming,” *Deutsche Forschungsanstalt fuer Luft- und Raumfahrt e.V. (DLR)*, 1988.

Bruno Moorthamers, PhD

bmoorthamers@gmail.com | 435-764-4239 | <https://www.linkedin.com/in/bmoorthamers>

Aerodynamics – Aircraft Design – Flight Performance – Method Development

Work Experience

Aerospace Engineer Sept 21 - now
DARcorporation - Lawrence, Kansas, USA

Aerodynamic Design Engineer 2016-2017
Microdrones - Siegen, Germany

- Use of OpenFOAM 4.0 for external aerodynamic and thermodynamic studies
- Payload integration design and development from CAD to rapid prototyping and flight testing
- Rapid prototyping using 3D printing and CNC milling
- Communication with airframe manufacturer about changes to molds or production

Engineering Consultant 2014-2016
Alten - Brussels, Belgium

- Mechanical design, CAD, prototype production for automotive industry partners

Graduate Student 2013-2014
Airbus Future Projects Office - Hamburg, Germany

- Researched the impact of ultra-high bypass ratio engines mounted over the wing
- Developed methods to assess penalties on aerodynamics, stability, and weight
- Automated a sizing platform to converge to optimal aircraft design for a specific mission

Aerodynamic Engineering Intern 2013-2013
DARcorporation - Lawrence, Kansas, USA

- Developed methods to calculate stability and control derivatives of V-tail aircraft and validated these using existing wind tunnel and generated CFD data
- Wrote technical documentation to be read by consumers

Aerodynamic Engineer 2010-2012
Nuon Solar Team - Delft, The Netherlands

- Performed qualitative trade-off studies between new vehicle concepts
- Airfoil design for laminar flow using XFOIL and three-dimensional simulations using CFD
- Responsible for executing three scaled and one full scale wind tunnel test
- Responsible for full car assembly model, OML definition and mold design

Education

PhD Aerospace Engineering

2017-2021

Utah State University - Logan, Utah, USA

- Member of the AeroLab under supervision by Dr. Douglas Hunsaker
- Dissertation: 'A Study of Wings with Constant and Variable Sweep for Aerodynamic Efficiency in Inviscid Flow'
 - Lift, drag, and aerodynamic center position were studied over a large range of wing designs with varying aspect ratio, taper ratio, and sweep angles
 - Theoretical background for finite wing aerodynamics was revisited and comparisons between analytical and numerical results were presented
 - Shown that for certain combinations of aspect and taper ratios, inviscid flow studies indicate that crescent wings can produce less induced drag than wings with constant sweep, while maintaining a similar level of longitudinal static stability
 - Using optimization techniques, it can be shown that more optimal sweep profiles exist
- Academic activities
 - Taught 'Dynamics of Atmospheric Flight' full-time
 - Teaching Assistant for 'Aerodynamics' and 'Engineering Numerical Methods'
 - Authored five AIAA conference publications, one journal publication. One conference and one journal manuscript in review
- Other research subjects
 - Variable camber compliant wings: Shown that flexible, parabolic flaps can produce less drag than traditionally hinged flaps and require less deflection for the same change in lift coefficient

MSc Aerospace Engineering

2012-2014

Delft University of Technology - Delft, The Netherlands

- Graduation Project: Design of medium range passenger aircraft with ultra-high bypass ratio engines mounted over the wing at Airbus in Hamburg, Germany
- Specialization Track: Flight Performance & Propulsion, focused on aircraft design
- Attended 'History of Aircraft Design' class by Dr. Jan Roskam at University of Kansas

BSc Aerospace Engineering

2007-2010

Delft University of Technology - Delft, The Netherlands

- Graduation Project: Design of a Wave Energy Harvesting Device
- Six month exchange project to Politecnico di Milano in Milan, Italy

Skills & Qualifications

Professional Organizations: American Institute for Aeronautics and Astronautics, Vertical Flight Society

Programming: Python, MATLAB, C++, Isight, SIMULINK, OpenMDAO

Aero: XFOIL, OpenVSP, Advanced Aircraft Analysis, MachUpX

CAD: SolidWorks, CATIA, Pro/ENGINEER, Siemens NX

CFD: FlightStream, Star-CCM+, OpenFOAM, PANAIR, VSPAERO, ParaView

Productivity: MS Office, LaTeX

Rapid Prototyping: RC aircraft production, 3D-printing, CNC

Optimization

- PhD dissertation research:
 - Use of SciPy's optimize.minimize library to optimize sweep profile for minimum induced drag
 - Single-objective, multivariable problem using inequality constraints
 - BFGS and SLSQP algorithms with basin hopping
 - Coupling FlightStream to in-house code
- Course: MAE 5930 Optimization
 - Mathematical theory and computational techniques
 - Unconstrained optimization
 - Linear programming
 - Integer programming
 - Convex programming
 - Nonlinear programming
- MSc thesis research:
 - Use of Dassault Systemes' Isight to build an automated sizing platform coupling aerodynamic and structural methods to size a passenger aircraft according to specific constraints